nature metabolism

Article

https://doi.org/10.1038/s42255-024-01078-9

PAQR4 regulates adipocyte function and systemic metabolic health by mediating ceramide levels

Received: 20 December 2023

Accepted: 6 June 2024

Published online: 03 July 2024

Check for updates

Qingzhang Zhu[1], Shiuhwei Chen[1], Jan-Bernd Funcke[1], Leon G. Straub[1], Qian Lin[1], Shangang Zhao[1,2], Chanmin Joung[1], Zhuzhen Zhang[1], Dae-Seok Kim[1], Na Li[1], Christy M. Gliniak[1], Charlotte Lee[3], Alberto Cebrian-Serrano[4,5], Line Pedersen[1,6], Nils Halberg[6], Ruth Gordillo[1], Christine M. Kusminski[1] & Philipp E. Scherer[1]

PAQR4 is an orphan receptor in the PAQR family with an unknown function in metabolism. Here, we identify a critical role of PAQR4 in maintaining adipose tissue function and whole-body metabolic health. We demonstrate that expression of *Paqr4* specifically in adipocytes, in an inducible and reversible fashion, leads to partial lipodystrophy, hyperglycaemia and hyperinsulinaemia, which is ameliorated by wild-type adipose tissue transplants or leptin treatment. By contrast, deletion of *Paqr4* in adipocytes improves healthy adipose remodelling and glucose homoeostasis in diet-induced obesity. Mechanistically, PAQR4 regulates ceramide levels by mediating the stability of ceramide synthases (CERS2 and CERS5) and, thus, their activities. Overactivation of the PQAR4–CERS axis causes ceramide accumulation and impairs adipose tissue function through suppressing adipogenesis and triggering adipocyte de-differentiation. Blocking de novo ceramide biosynthesis rescues PAQR4-induced metabolic defects. Collectively, our findings suggest a critical function of PAQR4 in regulating cellular ceramide homoeostasis and targeting PAQR4 offers an approach for the treatment of metabolic disorders.

The ability of adipose tissue to dynamically adapt to various nutritional conditions is centre stage to the preservation of metabolic homoeostasis[1,2]. An unhealthy expansion of adipose tissue during obesity, mainly via a process referred to as hypertrophy (an increase in adipocyte size) rather than hyperplasia (involving de novo adipogenesis), is closely tied to chronic inflammation in adipose tissue, dyslipidaemia and systemic insulin resistance. However, adipose tissue atrophy or lipodystrophy (pathological conditions featuring a loss of fat tissue) are also associated with whole-body metabolic dysfunction due to aberrant lipid accumulation in non-adipose tissues and lower levels of critical adipokines, such as leptin and adiponectin. Moreover, adipocyte de-differentiation has recently been observed in several (patho) physiological settings, including lactation[3], skin repair and fibrosis[4,5], as well as several types of cancer, such as liposarcomas[6], nasopharyngeal carcinoma[7] and breast cancer[8]. Thus, further insights into the mechanisms underlying adipose tissue remodelling are critical for

[1]Touchstone Diabetes Center, Department of Internal Medicine, University of Texas Southwestern Medical Center, Dallas, TX, USA. [2]Sam and Ann Barshop Institute for Longevity and Aging Studies, Division of Endocrinology, Department of Medicine, University of Texas Health Science Center at San Antonio, San Antonio, TX, USA. [3]Center for Hypothalamic Research, University of Texas Southwestern Medical Center, Dallas, TX, USA. [4]Institute for Diabetes and Obesity, Helmholtz Diabetes Center, Helmholtz Zentrum München, Neuherberg, Germany. [5]German Center for Diabetes Research (DZD), Neuherberg, Germany. [6]Department of Biomedicine, University of Bergen, Bergen, Norway. e-mail: philipp.scherer@utsouthwestern.edu

a basic understanding of adipose tissue function and the associated metabolic dysregulation.

Sphingolipids are initially generated by the condensation of palmitoyl-CoA and serine through the enzyme serine palmitoyltransferase (SPT). Ceramides are key players in sphingolipid metabolism, as they are the foundation for the synthesis of more complex sphingolipids such as sphingomyelins and lactosylceramides. Increased ceramide levels are tightly linked to cellular dysfunction in different tissues. Inhibiting ceramide biosynthesis in adipocytes enhances adipose tissue beiging and improves adipose tissue metabolism in a cell-autonomous way[9]. Accordingly, numerous studies suggest that sphingolipids are closely associated with multiple pathophysiological conditions, including insulin resistance, type 2 diabetes, cardiovascular complications and cancer[10,11]. Moreover, genetic or pharmacological inhibition of de novo ceramide synthesis ameliorates glucose intolerance and insulin resistance in obese and diabetic models with dyslipidaemia[12] suggesting that such lipotoxic consequences are, at least in part, associated with these sphingolipid species. However, we have a limited understanding of the detailed mechanistic basis as to how a cell maintains ceramide levels.

The progestin and adipoQ receptor (PAQR) family features proteins with seven transmembrane helices and contains 11 sequence paralogues in three classes, with apparently distinct agonist specificities[13,14]. Class I includes PAQR1 through PAQR4. Among the members of this group, PAQR1 and PAQR2 are well-known as adiponectin receptors (AdipoR1 and AdipoR2). They have an important role in obesity-associated metabolic diseases and cancer[15]. Adiponectin, an insulin-sensitizing adipokine, effectively lowers ceramide levels by stimulating a ceramidase activity within AdipoR1/AdipoR2 (ref. 16). In contrast to AdipoR1/AdipoR2 and PAQR3, PAQR4 is not responsive to adiponectin[17]. Moreover, PAQR4 does not seem to be a plasma membrane receptor, as it mainly localizes to the Golgi apparatus[18]. This suggests it may not act as a 'classical receptor' involved in signal transduction from the extracellular milieu, such as AdipoR1/AdipoR2. Likewise, PAQR3 acts as an anchor protein for Scap/SREBP in the Golgi and regulates cholesterol homoeostasis[19]. PAQR3 also serves as a tumour suppressor in different cancer types[20,21], whereas PAQR4 seems to promote tumour progression, probably by regulating cell cycle and/or local ceramide toxicity[18,22]. Thus, PAQRs may play powerful roles in distinct biological processes. These proteins are potential therapeutic targets, as exemplified by AdipoR1/AdipoR2 modulators developed to address metabolic diseases and cancer[23]. However, the closest homologue to AdipoR1/AdipoR2, PAQR4, remains an understudied member beyond its tumour-associated effects. Here, by using an array of mouse models with both gain and loss of function, we demonstrate that PAQR4 acts as an essential regulator of adipocyte function, critically involved in ceramide metabolism, thereby impacting global metabolic homoeostasis. Based on our findings, PAQR4 may serve as a powerful therapeutic target for metabolic diseases.

Results

PAQR4 is an important player in regulating adipose function

Adipose tissue dysfunction is an important component and frequently a driving force for metabolic disorders. *PAQR4* expression is upregulated in abdominal subcutaneous white adipose tissue (sWAT) in obese individuals, associated with fibrogenesis[24], regardless of the degree of impaired glucose metabolism, compared with healthy lean sWAT (Fig. 1a). The upregulation of *PAQR4* is inversely correlated with the decrease of *ADIPOQ* and *PPARG* expression, suggesting an important role in adipose tissue remodelling (Fig. 1a,b). Likewise, in an unbiased gene expression analysis by RNA sequencing[25,26], *Paqr4* was identified as a top hit with remarkable upregulation in widely expanded adipose tissues, including gonadal (gWAT), inguinal (sWAT), mesenteric white adipose tissue (mWAT) and brown fat (BAT) from massively obese mice, compared with less expanded adipose tissues from obese mice, in both males and females (Extended Data Fig. 1a,b). *Paqr4* was most abundant in white adipose tissue (WAT) and heart tissue when examining multiple tissues (Extended Data Fig. 1c). However, *Paqr4* upregulation in response to high-fat diet (HFD)-exposure was observed in adipose tissues but not in the heart (Extended Data Fig. 1d), indicating a special role in adipose tissue function. Little is known about the metabolic function of PAQR4. We therefore generated transgenic mice that allowed us to express *Paqr4* specifically in adipocytes in a doxycycline (dox)-dependent manner (hereafter referred to as *Paqr4*^{ad} mice) (Fig. 1c). Upon dox treatment, *Paqr4* was only induced in adipose tissues, but not in other tissues (Extended Data Fig. 1e), highlighting the tissue specificity of our system. Upon induction of dox chow, *Paqr4*^{ad} mice displayed a remarkable decrease in body weight (Fig. 1d,e), mainly due to a reduction in fat mass (Fig. 1f,g). By contrast, lean mass was increased (Extended Data Fig. 1f,g), consistent with a lipodystrophic phenotype. Indeed, weight, volume and size of the various fat pads were markedly reduced, whereas the liver was massively steatotic (Fig. 1h,i, Extended Data Fig. 1h,i and Supplementary Videos 1 and 2). Moreover, histological analyses reflected enhanced macrophage infiltration and fibrosis in adipose tissues and more lipid accumulation in the liver (Fig. 1j). The impact of *Paqr4* overexpression in the adipocytes occurred rapidly. Expression of genes related to adipogenesis and mature adipocytes were significantly downregulated (Fig. 1k), together with decreases in circulating adiponectin and leptin levels (Fig. 1l,m), all within 1 week of gene induction. Thus, PAQR4 overexpression caused severe fat degeneration. As a result of fat loss, *Paqr4*^{ad} mice displayed hypothermia upon acute and adapted cold exposure (Fig. 1n and Extended Data Fig. 1j). Moreover, *Paqr4*^{ad} mice exhibited glucose intolerance and impaired insulin-mediated glucose disposal within 2–3 weeks of dox chow induction (Extended Data Fig. 1k,m), both of which were further aggravated thereafter (Fig. 1o–q). Therefore, adipocyte PAQR4 plays an important role in adipose tissue function.

PAQR4 induces insulin resistance despite weight loss

We more specifically addressed the role of PAQR4 in diet-induced obesity. Consistent with the results observed under chow-fed conditions,

Fig. 1 | PAQR4 is an important player in regulating adipose tissue function. **a**, Gene expression of *PAQR4*, *ADIPOQ* and *PPARG* from human abdominal sWAT. Data are extracted from GSE159924. Lean-NL, healthy lean normal, $n = 12$; Ob-NL, obese with normal intrahepatic triglyceride content and normal glucose tolerance, $n = 21$; Ob-NAFLD, obese with non-alcoholic fatty liver disease (NAFLD) and abnormal glucose metabolism, $n = 24$. **b**, Inverse correlation of gene expression of *PAQR4* with adipocyte markers *ADIPOQ* and *PPARG*. Individual data represent Lean-NL (white circles), Ob-NL (grey circles) and Ob-NAFLD (dark circles). **c**, Scheme of *Paqr4*^{ad} mouse model (top); *Paqr4*^{ad} mice are leaner (bottom) fed a dox chow diet for 15 weeks. **d**–**h**, Reduced body weight (**d**) and weight gain (**e**) (WT, $n = 7$; *Paqr4*^{ad}, $n = 6$), reduced fat mass (**f**) and fat percentage (**g**) (WT, $n = 8$; *Paqr4*^{ad}, $n = 10$), reduced fat pad weights and elevated liver weights (**h**) (WT, $n = 7$; *Paqr4*^{ad}, $n = 6$) in *Paqr4*^{ad} mice fed dox chow diet for 15 weeks. **i**, Smaller fat pads and fatty liver in *Paqr4*^{ad} mice. **j**, Haematoxylin and eosin (H&E) staining of adipose tissues and liver (WT, $n = 3$; *Paqr4*^{ad}, $n = 4$). Scale bar, 200 µm. **k**, Downregulation of mature adipocyte markers in different adipose tissues from *Paqr4*^{ad} mice fed a dox chow diet for 1 week (WT, $n = 6$; *Paqr4*^{ad}, $n = 9$). **l**, Progressive reduction of serum adiponectin levels in *Paqr4*^{ad} mice fed with a dox chow diet ($n = 5$). **m**, Reduced serum leptin levels in *Paqr4*^{ad} mice fed a dox chow diet for 1 week (WT, $n = 10$; *Paqr4*^{ad}, $n = 8$). **n**, *Paqr4*^{ad} mice display hypothermia upon acute cold exposure under fasting conditions fed a dox chow diet for 2 weeks (WT, $n = 7$; *Paqr4*^{ad}, $n = 6$). **o**–**q**, Impaired glucose tolerance (**o**), glucose-stimulated hyperinsulinaemia (**p**) and insulin-mediated glucose disposal (**q**) in *Paqr4*^{ad} mice fed a dox chow diet for 8–9 weeks (WT, $n = 7$; *Paqr4*^{ad}, $n = 6$). Data are mean ± s.e.m. and were analysed by two-way ANOVA (**d**–**g**,**l**,**n**–**q**), one-way ANOVA followed by Holm–Sidak multiple-comparison test (**a**), Pearson correlation test (**b**) and two-tailed unpaired *t*-test (**k**,**m**). CPM, counts per million.

https://doi.org/10.1038/s42255-024-01078-9

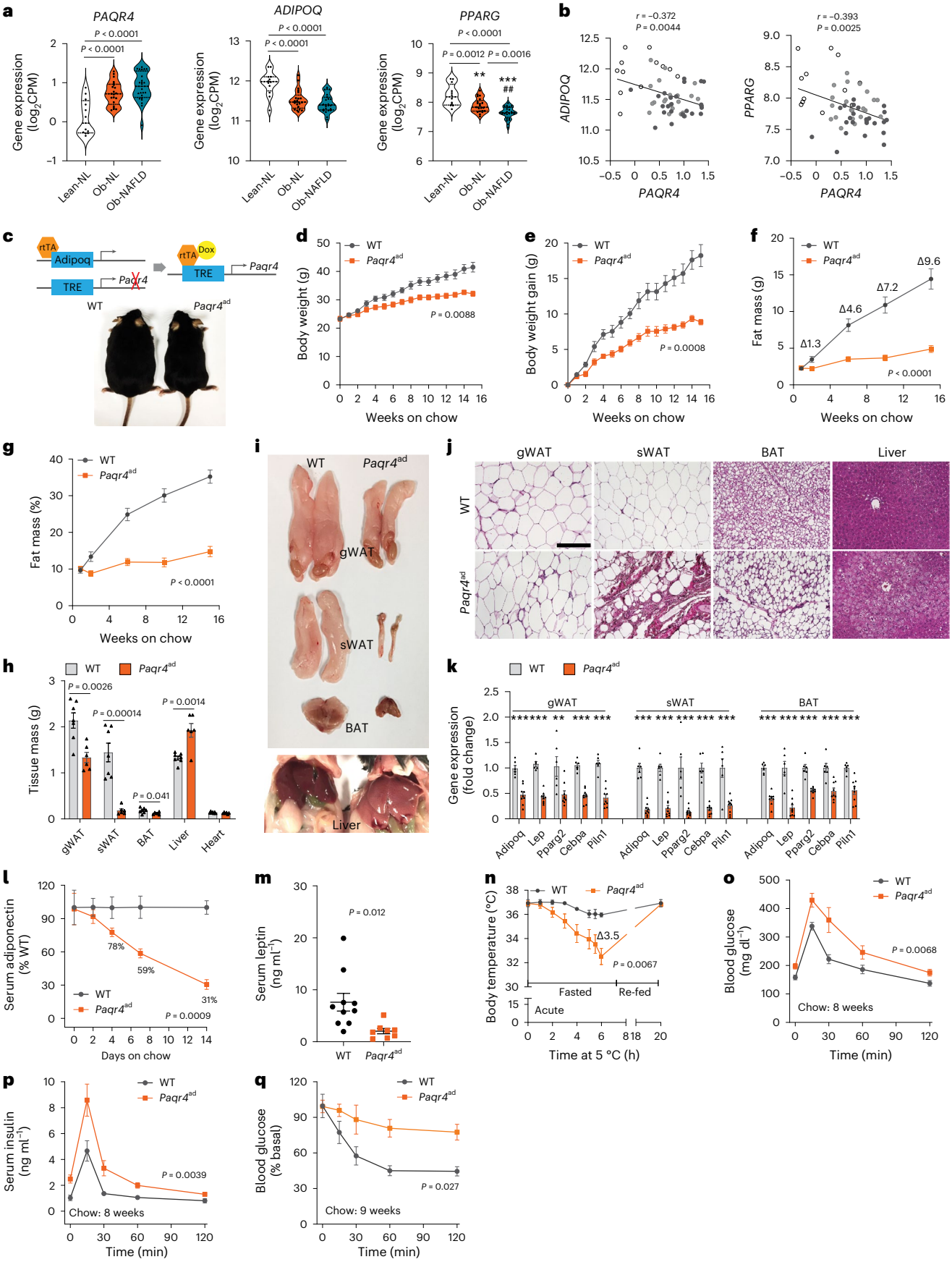

in a dox dose-dependent manner (Extended Data Fig. 2a), HFD-fed *Paqr4*^{ad} mice displayed a substantially reduced weight gain, mainly due to a reduction in fat mass, as well as severe hepatic steatosis with elevated alanine transaminase (ALT) levels (Fig. 2a–e and Extended Data Fig. 2b–g). Moreover, within 2 weeks of dox HFD feeding, *Paqr4*^{ad} mice exhibited remarkably reduced respiratory exchange ratios (RERs) under both fed and re-fed conditions, which were not altered upon overnight fasting (Extended Data Fig. 2h). This is reflective of a dramatically reduced metabolic flexibility in these mice. Thus, PAQR4 caused a shift from carbohydrate oxidation towards fat oxidation, with carbohydrate oxidation being reduced during feeding as well as upon re-feeding after a fast. In fact, carbohydrate use was maintained at constant levels during fasting as under fed conditions (Extended Data Fig. 2i). By contrast, fatty acid oxidation was elevated both in the fed state as well as upon re-feeding after a fast. During fasting, fatty acid oxidation remained at the same level as in the fed state (Extended Data Fig. 2j). VO_2, VCO_2 and energy expenditure were slightly reduced under fed conditions, whereas physical activity was unaltered (Extended Data Fig. 2k–n). Moreover, there was no impact on food intake during this time period when body weight differences were very small (Extended Data Fig. 2o). Thus, PAQR4 regulates metabolic homoeostasis by dramatically altering metabolic flexibility rather than food intake.

Histological analyses demonstrated enhanced macrophage infiltration in *Paqr4*-transgenic adipose tissues (Fig. 2e and Extended Data Fig. 3a). In addition, gene expression analyses revealed that anti-inflammatory M2 macrophages were increased in both gWAT and sWAT, concomitant with a suppression of some pro-inflammatory cytokines, such as *Il1b* and *Il6*, but not *Tnf* (Fig. 2f,g). Both M1 and M2 macrophages were elevated in BAT (Extended Data Fig. 3a,b). Moreover, fibrosis was markedly enhanced in all fat pads, including gWAT, sWAT and BAT from *Paqr4*^{ad} mice (Extended Data Fig. 3c). Consistent with the impaired adipose tissue function, lower circulating adiponectin and leptin levels were observed (Fig. 2h,i), concomitant with hyperglycaemia and hyperinsulinaemia (Extended Data Fig. 3d,e), in a dox dose-dependent manner. As a consequence, *Paqr4*^{ad} mice displayed glucose intolerance and impaired insulin-mediated glucose disposal upon 2–3 weeks of dox HFD feeding (Extended Data Fig. 3f,g) and this impairment was massively aggravated at later time points (Fig. 2j–m and Extended Data Fig. 3h,i). Compared with chow-fed conditions, where glucose-stimulated insulin release was elevated in *Paqr4*^{ad} mice, the effect was substantially decreased under HFD-fed conditions (Fig. 2k,l). Massive β cell hypertrophy was observed in the pancreas of *Paqr4*^{ad} mice, albeit with overall less insulin content (Fig. 2e), indicating impaired β cell function. In addition, insulin signalling was impaired in multiple metabolic tissues (Extended Data Fig. 3j,k).

Therefore, when *Paqr4* expression is initiated at the onset of obesogenic conditions and maintained using dox HFD, PAQR4 reduces adiposity but impairs glucose homoeostasis. We thus asked whether these effects would still occur if we induce *Paqr4* gene expression in mice with pre-existing obesity. We pushed the mice to an obese state with 6 weeks of HFD only (without dox supplementation), and then switched to dox HFD. Notably, even under these conditions, induction of *Paqr4* not only prevented further weight gain, but caused rapid weight loss, along with lower circulating leptin levels and impaired glucose tolerance (Fig. 2n–q). These findings indicate that PAQR4 exerts its potent effects on the adipocyte even in the obese state.

Amelioration of PAQR4-induced metabolic defects by fat transplants or leptin

Given that PAQR4 overexpression causes lipodystrophy, we next asked whether an adipose tissue transplant from a wild-type mouse would improve the metabolic state. To this end, we transplanted sWAT from control mice to the corresponding sites of *Paqr4*^{ad} mice. The transplants grew well in *Paqr4*^{ad} mice fed with dox chow, in sharp contrast to the atrophic endogenous sWAT (Fig. 3a,b). Of note, the transplants fully reversed hyperglycaemia and hyperinsulinaemia in *Paqr4*^{ad} mice (Fig. 3c,d). Accordingly, glucose tolerance and insulin-mediated glucose disposal were also normalized (Fig. 3e–g); however, overall body weight loss and the fatty liver phenotype were not rescued (Extended Data Fig. 4a–c). Furthermore, the transplants did not normalize circulating leptin and adiponectin levels (Fig. 3h and Extended Data Fig. 4d). In fact, leptin levels were even further reduced upon transplantation.

Leptin constitutes a treatment option for lipodystrophy in humans. In light of the partial lipodystrophy prevailing in the transgenic mice, we decided to infuse *Paqr4*^{ad} mice that were fed for 14 weeks with dox chow with a physiological leptin dose (Fig. 3i), which doubled the circulating levels in the transgenic mice. At this dose, leptin did not rescue body weight or fat mass (Extended Data Fig. 4e,f) and it also had only minimal effects on food intake (Extended Data Fig. 4g); however, leptin treatment improved hyperglycaemia and hyperinsulinaemia both under fed and fasted conditions (Fig. 3j,k). Leptin treatment moreover mitigated liver steatosis, reflected by a decreased liver:body weight ratio, liver triglyceride content and serum ALT levels (Fig. 3l–n and Extended Data Fig. 4h). In addition, glucose tolerance and insulin tolerance were normalized by leptin treatment (Fig. 3o–p). Notably, leptin infusion also improved the histological appearance of adipose tissue (Extended Data Fig. 4h) and slightly increased circulating adiponectin levels (Fig. 3q), suggesting that leptin supplementation partially improves metabolic stress in the adipose tissues of *Paqr4*^{ad} mice.

We also crossed the *Paqr4*^{ad} mice into the leptin-deficient *ob*/*ob* background. Of note, *ob*/*ob:Paqr4*^{ad} mice gained substantially less body weight than their *ob*/*ob* controls (Extended Data Fig. 4i). Notably, food intake was transiently reduced by PAQR4 assessed at the beginning of dox induction when body weight was similar; however, it recovered to control levels soon thereafter, both in *Paqr4*^{ad} and *ob*/*ob:Paqr4*^{ad} mice (Extended Data Fig. 4j). Surprisingly, glucose intolerance was even more severe in *ob*/*ob:Paqr4*^{ad} mice than in *ob*/*ob* mice, although glucose-stimulated insulin levels were comparable (Extended Data Fig. 4k,l). Thus, Paqr4-induced adipose tissue dysfunction occurs even in the complete absence of leptin. *Paqr4*^{ad} mice, therefore, do not exert their effects on metabolism through leptin; however, leptin is clearly able to improve the insulin resistance induced by *Paqr4* overexpression.

Paqr4-deletion in adipocytes improves glucose homoeostasis in obesity

As the overexpression of *Paqr4* in adipocytes clearly exerts detrimental effects, we also wanted to investigate the consequences of a loss of function of the *Paqr4* gene in adipocytes. We generated *Paqr4*-flox mice and crossed them with Adipoq-rtTA and TRE-Cre mice to achieve a dox-dependent, inducible knockout of *Paqr4* specifically in adipocytes (hereafter referred to *Paqr4*^{iAKO} mice) (Fig. 4a). With the ability to trigger the loss of function in adult animals, we eliminate any developmental issues that could arise from a loss of *Paqr4*. After 2 weeks of dox chow induction, gene rearrangements specifically occurred in adipose tissues, accompanied by a substantial decrease in *Paqr4* expression in *Paqr4*^{iAKO} mice (Extended Data Fig. 5a,b).

Under dox chow-fed conditions, *Paqr4*^{iAKO} mice displayed a subtle phenotype, with normal body weight, body composition, fat pad weights and slightly decreased liver weights (Extended Data Fig. 5c–e). There was no marked impact on glucose tolerance or insulin sensitivity, even after 8–9 weeks of dox chow feeding (Extended Data Fig. 5f,g); however, these parameters were slightly improved in older *Paqr4*^{iAKO} mice after 19–20 weeks of induction (Extended Data Fig. 5h–j).

We examined the metabolic effects of PAQR4 loss in *Paqr4*^{iAKO} mice fed a dox HFD. Body weight gain was comparable after 18 weeks of dox HFD feeding (Fig. 4b,c). *Paqr4*^{iAKO} mice also displayed normal food intake and energy expenditure without appreciable effects on RER, VO_2, VCO_2 or physical activity (Extended Data Fig. 5k–p). Furthermore, *Paqr4*^{iAKO} and control mice had comparable body composition and WAT mass (Fig. 4d and Extended Data Fig. 5q,r); however, the liver weight

https://doi.org/10.1038/s42255-024-01078-9

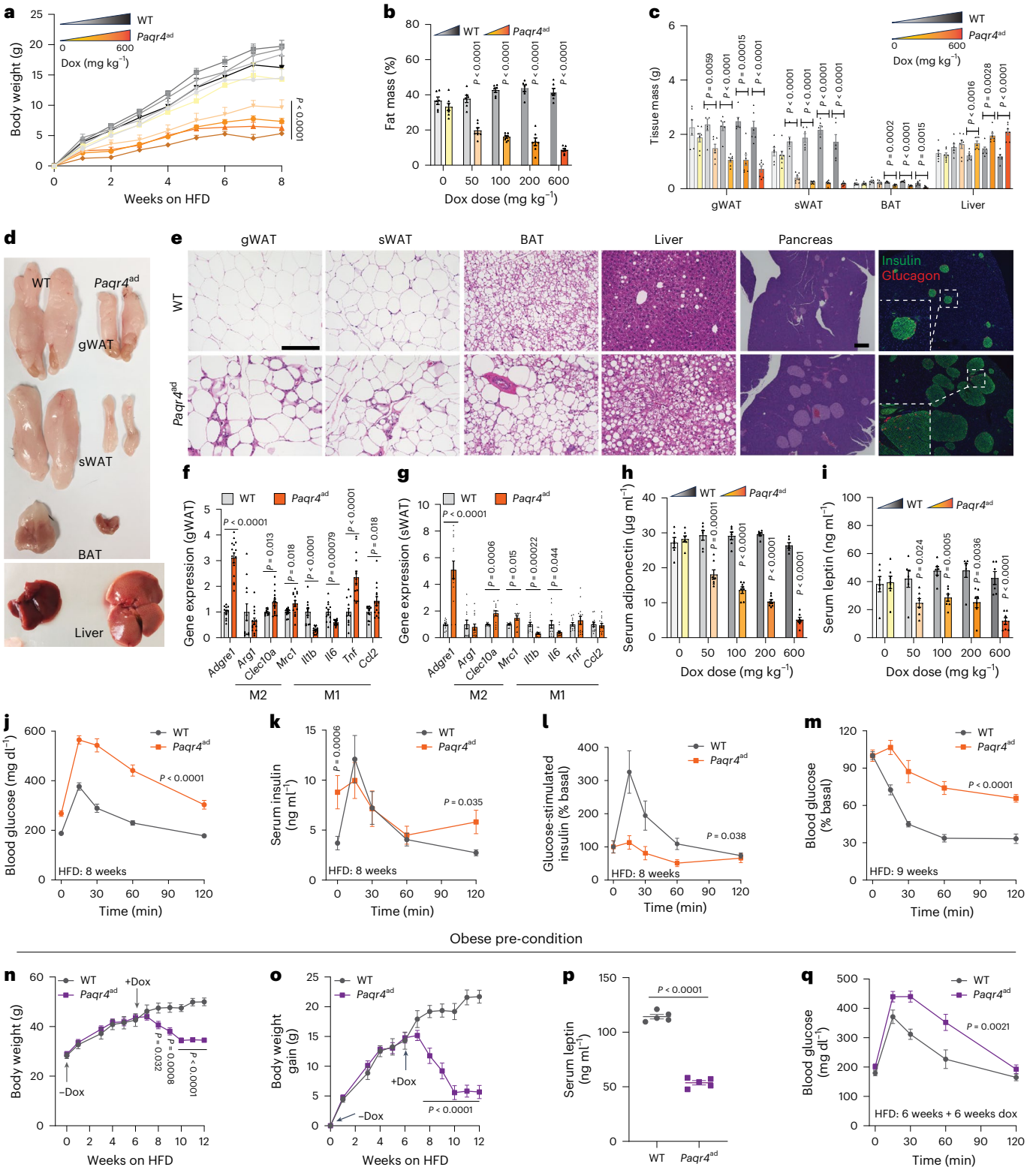

Fig. 2 | *Paqr4*-overexpressing mice display insulin resistance despite reduced weight upon HFD feeding. Mice were fed dox HFD (600 mg kg^{-1} except in the dox-response assays). **a**–**c**, Dox dose-dependent effects on reduction in weight gain, fat percentage, fat pad weights and liver weight in *Paqr4*^{ad} mice at week 8 (wild type (WT), $n = 6$; *Paqr4*^{ad}, $n = 7$). **d**, Smaller fat pads and fatty liver in *Paqr4*^{ad} mice. **e**, H&E staining of adipose tissues, liver and pancreas and immunostaining of insulin (green) and glucagon (red) of pancreas ($n = 3$). Scale bar for adipose tissues and liver, 200 μm; for pancreas, 400 μm. **f**,**g**, Inflammatory gene expressions in gWAT (**f**) and sWAT (**g**) at week 3 (WT, $n = 12$; *Paqr4*^{ad}, $n = 14$). **h**,**i**, Dox dose–response effects of reduction in levels of serum adiponectin (**h**) and leptin (**i**) in *Paqr4*^{ad} mice (WT, $n = 6$; *Paqr4*^{ad}, $n = 7$). **j**–**l**, Impaired glucose tolerance (**j**) (WT, $n = 14$; *Paqr4*^{ad}, $n = 12$) and glucose-stimulated insulin release (**k**,**l**) ($n = 6$) in *Paqr4*^{ad} mice. **m**, Impaired insulin-mediated glucose disposal in *Paqr4*^{ad} mice (WT, $n = 8$; *Paqr4*^{ad}, $n = 6$). **n**–**q**, Reduced body weight (**n**) and weight gain (**o**) in *Paqr4*^{ad} mice fed a HFD, and decreased serum leptin levels on week 2 (**p**) and impaired glucose tolerance on week 6 (**q**) upon switching to dox HFD in obese *Paqr4*^{ad} mice previously fed 6 weeks of HFD without dox ($n = 5$). Data are mean ± s.e.m. and were analysed by two-way ANOVA (**a**,**j**–**o**,**q**) and two-tailed unpaired *t*-test (**b**,**c**,**f**–**i**,**p**).

https://doi.org/10.1038/s42255-024-01078-9

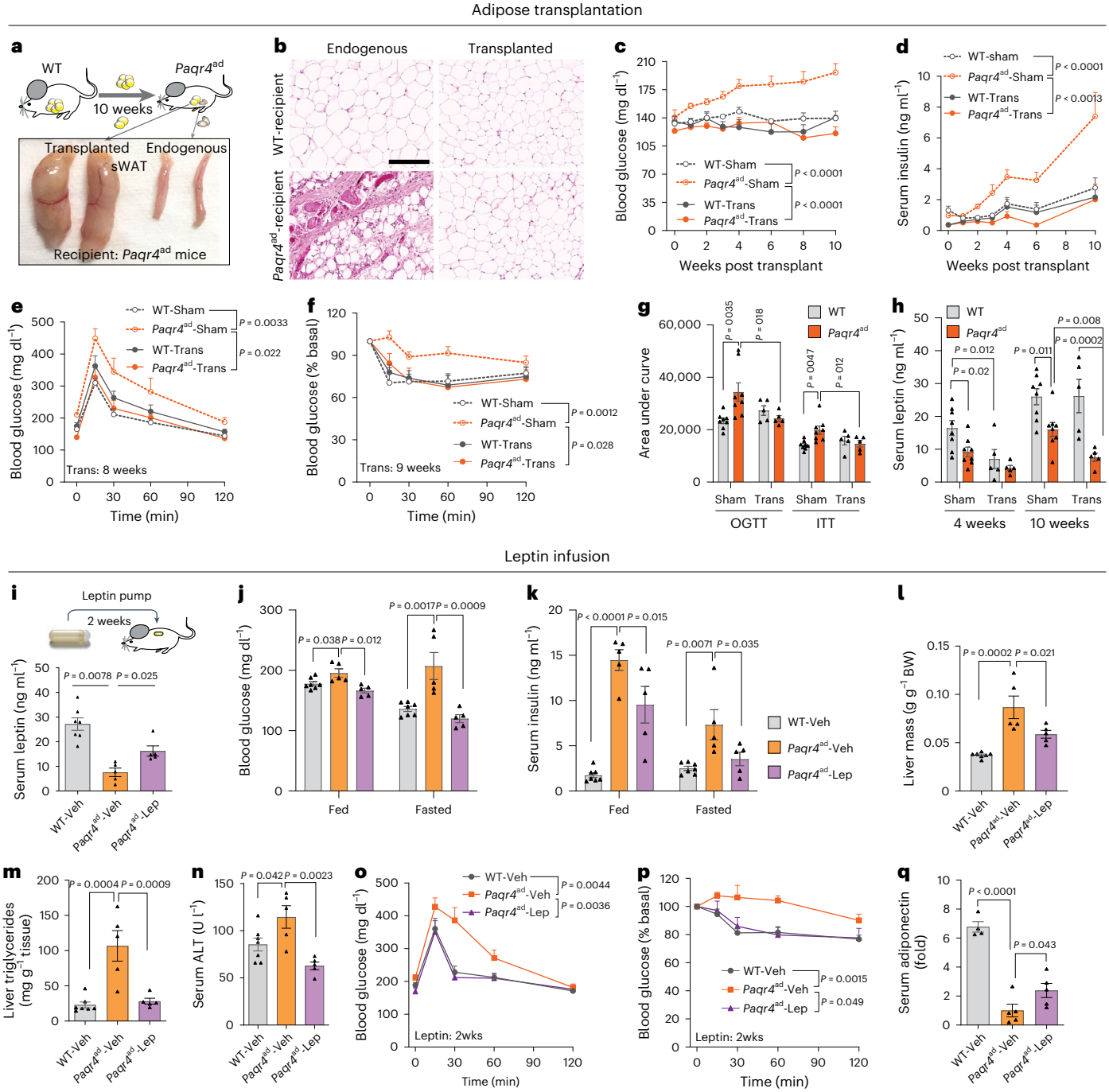

Fig. 3 | Amelioration of PAQR4-induced metabolic dysfunction with adipose tissue transplants or leptin administration. Mice receiving subcutaneous adipose tissue transplants (sWAT) were fed dox chow for 10 weeks. **a**, Endogenous and transplanted sWAT in *Paqr4*^{ad} mice. **b**, Transplanted sWAT displays healthy morphology in both wild-type (WT) and *Paqr4*^{ad} mice ($n = 3$). Scale bar, 200 µm. **c**–**g**, Adipose transplant normalizes hyperglycaemia (**c**), hyperinsulinaemia (**d**), glucose tolerance (**e**,**g**) and insulin-mediated glucose disposal (**f**,**g**) in *Paqr4*^{ad} mice (sham, $n = 8$ per group; transplant, $n = 5$ per group). ITT, insulin tolerance test; OGTT, oral glucose tolerance test; **h**, Adipose transplant does not recover serum leptin in *Paqr4*^{ad} mice (sham, $n = 8$ per group; transplant, $n = 5$ per group). **i**, Two weeks of leptin infusion increases serum leptin levels in *Paqr4*^{ad} mice that were previously exposed to dox chow for 14 weeks (WT, $n = 7$; *Paqr4*^{ad}, $n = 5$ per group). **j**,**k**, Leptin improves hyperglycaemia (**j**) and hyperinsulinaemia (**k**) in *Paqr4*^{ad} mice (WT, $n = 7$; *Paqr4*^{ad}, $n = 5$ per group). **l**–**n**, Leptin reduces liver/body weight (BW) ratio (**l**), liver triglyceride content (**m**) and serum ALT levels (**n**) in *Paqr4*^{ad} mice (WT, $n = 7$; *Paqr4*^{ad}, $n = 5$ per group). **o**,**p**, Leptin normalizes glucose tolerance and insulin-mediated glucose disposal in *Paqr4*^{ad} mice (WT, $n = 7$; *Paqr4*^{ad}, $n = 5$ per group). **q**, Leptin slightly increases serum adiponectin levels in *Paqr4*^{ad} mice (WT, $n = 4$; *Paqr4*^{ad}, $n = 5$ per group). Data are mean ± s.e.m. and analysed by two-way ANOVA (**c**–**h**,**o**,**p**) and one-way ANOVA followed by a Holm–Sidak multiple-comparison test (**i**–**n**,**q**).

was reduced with diminished steatosis (Fig. 4d–f and Extended Data Fig. 5r). In addition, BAT mass was decreased with reduced lipid-droplet size and enhanced *Ucp1* expression (Fig. 4d,e,g). Meanwhile, histological improvements were observed in WAT, accompanied by the downregulation of several inflammatory and fibrotic genes (Fig. 4e,h,i). Circulating leptin levels were decreased, whereas adiponectin levels were increased (Fig. 4j,k), suggesting improved adipose function without any impact on overall fat mass. Moreover, *Paqr4*^{iAKO} mice exhibited

https://doi.org/10.1038/s42255-024-01078-9

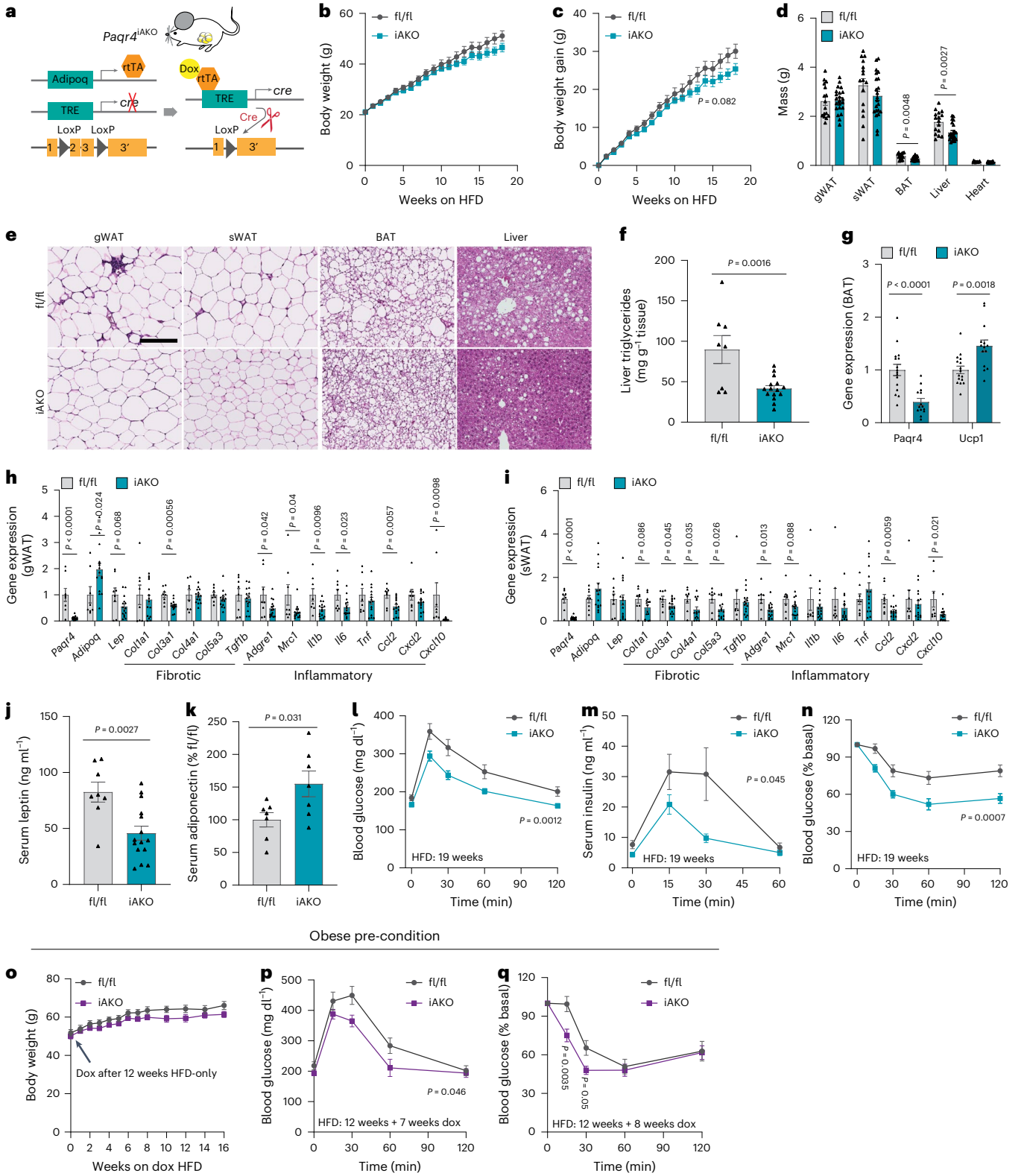

Fig. 4 | Adipocyte-specific deletion of *Paqr4* improves glucose homoeostasis in obesity. Mice were fed a dox HFD. **a**, Scheme of *Paqr4*^{iAKO} mouse model. **b**,**c**, Body weight (**b**) and weight (**c**) gain upon dox HFD feeding (*Paqr4*$^{fl/fl}$, $n = 16$; *Paqr4*^{iAKO}, $n = 22$). **d**, Tissue weight at week 20 (*Paqr4*$^{fl/fl}$, $n = 16$; *Paqr4*^{iAKO}, $n = 22$). **e**, H&E staining of adipose tissues and liver ($n = 6$). Scale bar, 200 µm. **f**, Reduced liver triglyceride content in *Paqr4*^{iAKO} mice (*Paqr4*$^{fl/fl}$, $n = 8$; *Paqr4*^{iAKO}, $n = 15$). **g**, Upregulation of *Ucp1* in *Paqr4*^{iAKO}-BAT (*Paqr4*$^{fl/fl}$, $n = 16$; *Paqr4*^{iAKO}, $n = 14$). **h**,**i**, Expression of genes related to fibrogenesis and inflammation in gWAT (**h**) and sWAT (**i**) (*Paqr4*$^{fl/fl}$, $n = 8$; *Paqr4*^{iAKO}, $n = 15$). **j**, Reduced serum leptin levels in *Paqr4*^{iAKO} mice (*Paqr4*$^{fl/fl}$, $n = 8$; *Paqr4*^{iAKO}, $n = 15$). **k**, Elevated serum adiponectin levels in *Paqr4*^{iAKO} mice ($n = 7$). **l**–**n**, Improved glucose tolerance (**l**) and enhanced insulin-mediated glucose disposal (**n**) (*Paqr4*$^{fl/fl}$, $n = 16$; *Paqr4*^{iAKO}, $n = 22$) with less glucose-stimulated insulin secretion (**m**) ($n = 15$) in *Paqr4*^{iAKO} mice. **o**–**q**, Deletion of *Paqr4* in obese preconditioned mice improves glucose tolerance (**p**) and insulin-mediated glucose disposal (**q**) without affecting body weight (**o**) (*Paqr4*$^{fl/fl}$, $n = 7$; *Paqr4*^{iAKO}, $n = 8$). Data are mean ± s.e.m. and analysed by two-way ANOVA (**b**,**c**,**l**–**q**) and two-tailed unpaired *t*-test (**d**,**f**–**k**).

moderately improved glucose tolerance and insulin tolerance after 2 weeks of dox HFD feeding (Extended Data Fig. 5s–u). Notably, under more severe conditions, 19–20 weeks of dox HFD feeding, *Paqr4*^{iAKO} mice displayed profound improvements in glucose tolerance and insulin-mediated glucose disposal (Fig. 4l–n), along with enhanced insulin signalling (Supplementary Fig. 1). In addition, we observed comparable improvements in glucose homoeostasis with unaltered body weight upon deleting *Paqr4* in mice with pre-existing obesity (Fig. 4o–q). Thus, in the absence of *Paqr4* in adipocytes, systemic metabolic homoeostasis improves in the obese state.

PAQR4 promotes adipose remodelling and adipocyte de-differentiation

Having demonstrated that PAQR4 is a critical regulator in adipose tissue remodelling and thus systemic glucose homoeostasis, we set out to determine the mechanistic basis of this connection. We first examined the role of PAQR4 on adipogenesis. Even though *Paqr4* is upregulated during adipocyte differentiation, its overexpression robustly downregulated mature adipocyte markers and inhibited adipogenesis in vitro (Extended Data Fig. 6a). In contrast, deletion of *Paqr4* elevated the expression of adipogenic markers *Pparg2, Plin1* and *Adipoq* during early adipogenesis (Extended Data Fig. 6b); however, PAQR4 exerted little effects on cell cycle during adipogenesis (Extended Data Fig. 6c). To test the impact of PAQR4 on adipogenesis in vivo, we fed *Paqr4*^{ad} mice from embryonic stage (E13) with dox chow and assessed adipose development. Of note, massive impairment was observed on postnatal day 7 (P7) in *Paqr4*^{ad}-gWAT, which develops postnatally (Extended Data Fig. 6d). Moreover, similar defects were also seen in sWAT and BAT, which develop during earlier embryonic stages, with a more pronounced impairment on P7 (Extended Data Fig. 6d–f). In *Paqr4*^{ad}-sWAT, prominent macrophage infiltration was observed on P7 (Extended Data Fig. 6e). Accordingly, the size of sWAT and BAT was reduced on day P7 (Extended Data Fig. 6g). At 6 weeks of age, *Paqr4*^{ad} mice displayed a 26% reduction in fat mass (Extended Data Fig. 6h). Thus, PAQR4 exerts a negative role on adipogenesis both in vitro and in vivo.

We subsequently performed single-cell RNA sequencing (scRNA-seq) to access the remodelling of adipocyte progenitor pool (Fig. 5a). We focused on *Pdgfra*$^+$ cells, as thay are expressed visually in all adipose stem and progenitor cells (ASPCs)[27]. These cells also express canonical ASPC markers, including *Pdgfrb*, *Ly6a* (also known as *Sca1)*, *Cd34* and *Cd29* (ref. 27)(Fig. 5b). Three subpopulations were identified which were resembling previously defined ASPC subpopulations according to the population-specific markers. P1 (*Dpp4*$^+$ cells) and P2 (*Icam1*$^+$) were represented as 'ASC2' and 'ASC1' as defined by Burl et al.[28] or 'group1' and 'group2' defined by Merrick et al.[29], respectively (Supplementary Fig. 2a–d). Whereas P3 was similar to 'group3' from Merrick et al.[29], which expressed *F3* (encoding CD142), *Fmo2* and *Gdf10* (Supplementary Fig. 2e). Schwalie et al.[30] defined an anti-adipogenic population of adipogenesis regulators (termed 'Aregs'), which expressed *F3* and *Abcg1*; however, we did not detect *Abcg1* in the P3 (*F3*$^+$) population (Supplementary Fig. 2e,f), in line with the mural-derived ASPCs (*Pdfgrb*$^+$*Dpp4*$^-$), which expressed *F3* but not *Abcg1* (ref. 31). DPP4$^+$ cells are considered as multipotent progenitors, whereas ICAM1$^+$ and CD142$^+$ cells are relatively restricted to the adipocyte lineage[29]. Gene Ontology (GO) enrichment analyses further indicated altered pathways were related to inflammation and smooth muscle cell activation in all the subpopulations; however, steroid metabolic pathways were found to be altered only in P1 (*Dpp4*$^+$ cells) (Fig. 5c and Supplementary Fig. 2g). Moreover, flow cytometry analysis indicated both ICAM1$^+$ and CD142$^+$ ASPCs were decreased by PAQR4, suggesting reduced adipogenic potential in the *Paqr4*^{ad} mice (Fig. 5d and Supplementary Fig. 3a). Thus, PAQR4 remodels the adipose stromal microenvironment into an environment less favourable towards adipogenesis.

Adipocyte turnover is tightly controlled under physiological conditions. As PAQR4 induction prompts a fat mass reduction in adult mice, we wondered what the impact is on adipocyte turnover. To study this, we crossed *Paqr4*^{ad} mice to our 'AdipoChaser' mice[4,32] (Adipoq-rtTA:TRE-Cre:Rosa26-mT/mG) (Fig. 5e). This allowed us to examine the effects of PAQR4 on adipocyte fate via a 'pulse–chase' labelling strategy. Following 2 weeks of dox induction, all adipocytes in control mice were efficiently labelled with enhanced green fluorescent protein (EGFP) (EGFP$^+$perilipin$^+$; Fig. 5e). Notably, in contrast to control adipose tissue, a lot of EGFP$^+$perilipin$^-$ fibroblast-like cells appeared in sWAT and, to a lesser extent, in gWAT of *Paqr4*^{ad} mice (Fig. 5e and Supplementary Fig. 3b). This reflects that these cells were in the fully developed mature adipocyte stage at induction during the labelling period, but subsequently lost their adipocyte identity and morphed into fibroblasts. Flow cytometry analysis further suggested that such de-differentiated adipocytes express the fibroblast marker PDGFRβ and can contribute up to ~9% of the stromal vascular pool of cells (Fig. 5f). Notably, these de-differentiated adipocytes re-differentiated into mature adipocytes within 4 weeks of dox withdrawal (Fig. 5e and Supplementary Fig. 3b), clearly reflecting that the process of PAQR4-induced de-differentiation is reversible. This suggests that we do not lose any cells due to necrosis or apoptosis upon PAQR4 induction. In fact, we were unable to observe any signs of adipocyte death (Supplementary Fig. 3c). In light of this, we also tested whether the withdrawal of dox could reverse the metabolic deficiencies in *Paqr4*^{ad} mice. We first fed *Paqr4*^{ad} mice with dox HFD for 6 weeks and then switched to HFD without dox. As expected, body weight gain increased shortly after dox withdrawal. Subsequent re-exposure to dox rapidly reduced weight again (Fig. 5g,h). Moreover, hyperglycaemia, hyperinsulinaemia and hypoleptinaemia were largely recovered following dox removal (Fig. 5i–k). Dox withdrawal even improved glucose tolerance (Fig. 5l), potentially reflecting enhanced leptin sensitivity after prolonged suppression of leptin, albeit this improvement eventually disappeared again (Fig. 5m).

Fig. 5 | PAQR4 promotes adipose remodelling and adipocyte de-differentiation. a, Aggregated uniform manifold approximation and projection (UMAP) plot of subcutaneous ASPCs from wild-type and *Paqr4*^{ad} mice. ASPCs were grouped into three subpopulations P1 (*Dpp4*$^+$), P2 (*Icam1*$^+$) and P3 (*F3*$^+$). **b**, ASPCs were identified based on well-established ASPC gene markers. The *y* axis is the log-scale-normalized read count. **c**, Gene ontology pathways related to biological processes with differentially expressed genes in P1 (*Dpp4*$^+$) subpopulation between genotypes. $P < 0.001$, false discovery rate (FDR) < 0.05. **d**, Cell frequency of ASPCs in sWAT analysed by flow cytometry ($n = 3$ mice per group). **e**, Immunofluorescent staining of Perilipin (red) and EGFP (green) in sWAT ($n = 3$) from Paqr4Chaser and control mice. Eight-week-old Chaser mice were fed dox chow for 2 weeks and then allowed to recover on dox-free chow for 4 weeks. Scale bar, 50 µm. **f**, Flow cytometry analysis of sWAT-SVF cells from Paqr4Chaser mice indicates adipocyte de-differentiated into PDGFRβ$^+$ precursor cells ($n = 3$ biological samples). **g**,**h**, Body weight (**g**) and ΔΔ weight gain (**h**) during dox recovery (Rev). ΔΔ weight gain represents body weight minus respective Δ weight gain; Δ weight gain represents body weight minus respective body weight at start point of dox withdrawal (dox, $n = 5$ for each group; Rev, $n = 7$ for each group). Mice were first fed dox HFD for 6 weeks, and then switched to HFD without dox (groups of WT-Rev and *Paqr4*^{ad}-Rev) or kept on dox HFD (groups of WT+dox and *Paqr4*^{ad}+dox). Dox HFD was re-introduced after 28 weeks of dox recovery. *P* values indicate comparisons between groups of *Paqr4*^{ad}-Rev and *Paqr4*^{ad} + dox. The arrows indicated dox intervention in the dox-recovery groups. **i**–**k**, Blood glucose (**i**), serum insulin (**j**) (before, $n = 12$ for each group; recovery, $n = 7$ for each group) and serum leptin (**k**) (before, $n = 5$ for each group; recovery, $n = 7$ for each group) during dox recovery. **l**,**m**, Glucose tolerance tests during dox recovery ($n = 7$). Data are mean ± s.e.m. and analysed by two-way ANOVA (**g**–**m**) and two-tailed unpaired *t*-tests (**d**, **f**).

https://doi.org/10.1038/s42255-024-01078-9

Blocking ceramide synthesis improves PAQR4-induced metabolic defects

PAQR4 displays a high sequence similarity with other class I PAQR family members, such as AdipoR1/AdipoR2. Given the critical role of AdipoR1/AdipoR2 in ceramide metabolism, we wondered whether PAQR4 is involved in the regulation of ceramide levels as well. PAQR4 indeed exhibited profound effects on sphingolipid metabolism. In contrast to the role of AdipoR1/AdipoR2 that effectively lower ceramide levels, PAQR4 increased multiple ceramide species in gWAT and sWAT, with the most pronounced increases observed in very long-chain ceramides

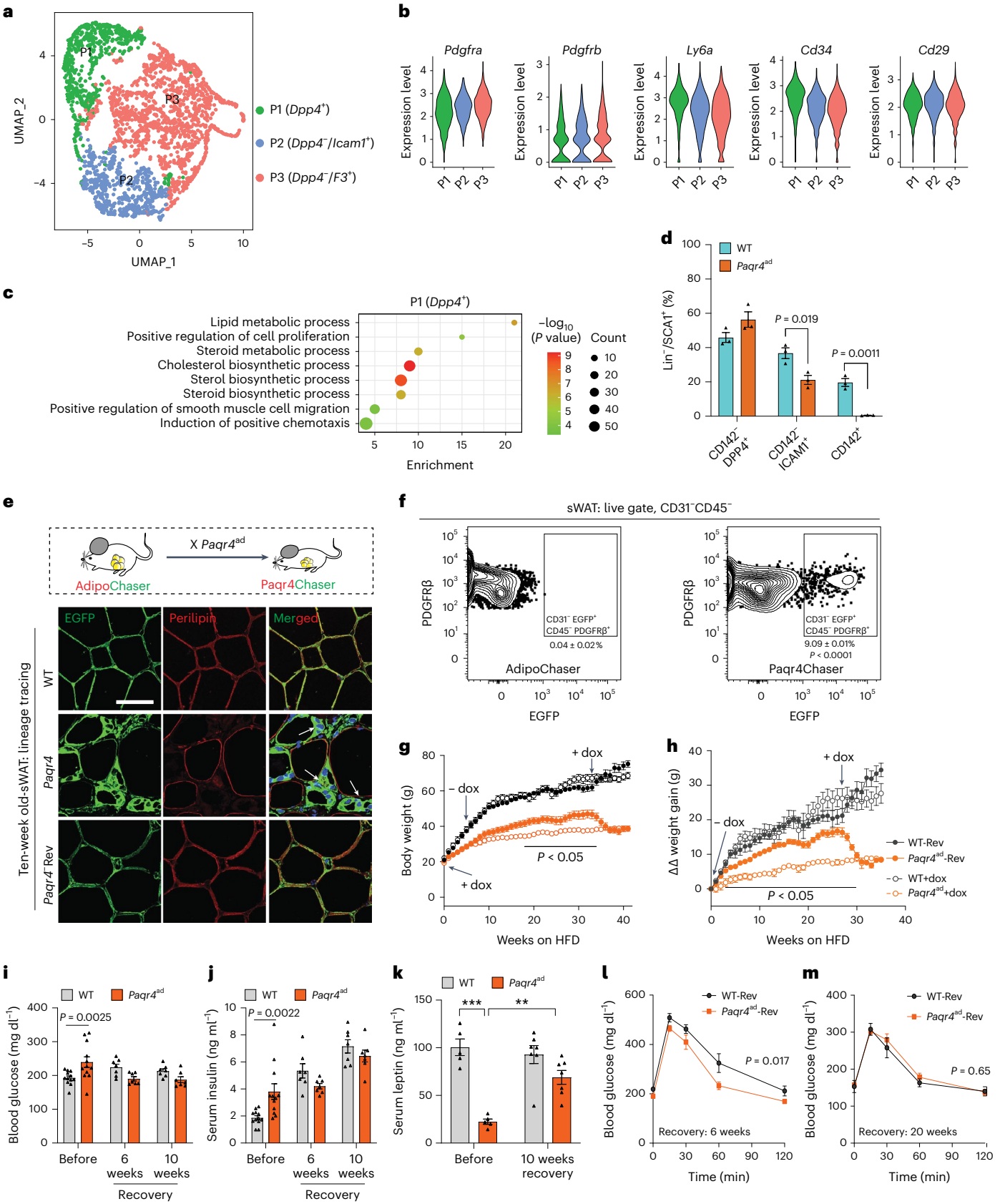

(C24:1 and C24:0) and more moderate increases in long-chain C16:0 ceramide (Fig. 6a and Extended Data Fig. 7a). Moreover, multiple species of dihydroceramides, hexosylceramides, sphingomyelin and lactosylceramides were also elevated in *Paqr4*^{ad} adipose tissues. We also saw an increase in sphinganine, sphingosine and sphingosine-1-phosphate in *Paqr4*^{ad} gWAT and sWAT (Extended Data Fig. 7b,c). This was also observed when these species were measured in serum, where ceramides, dihydroceramides and hexosylceramides were significantly increased (Supplementary Fig. 4a,b). Thus, PAQR4 seems to induce multiple lipids in the sphingolipid pathway (Fig. 6b). By contrast, in *Paqr4*^{iAKO} mice, various components of the sphingolipid pathway were decreased, an effect that was more pronounced in gWAT than in sWAT (Fig. 6a and Extended Data Fig. 7a–c). As for ceramides, C16:0 and C18:0 ceramides were most significantly reduced in *Paqr4*^{iAKO} gWAT and sWAT; however, compared with the changes in serum sphingolipids in *Paqr4*^{ad} mice, *Paqr4*^{iAKO} mice showed more moderate changes (Supplementary Fig. 4a,b), suggesting other tissues may compensate for the lack of PAQR4 in adipocytes in *Paqr4*^{iAKO} mice. Nevertheless, these gain- and loss-of-function findings suggest PAQR4 exerts profound effects on ceramide homoeostasis.

Similar to our observations in vivo, PAQR4 increased ceramide species in vitro in adipocytes, perturbing sphingolipid metabolism (Supplementary Fig. 5a,b). Deletion of *Paqr4* in adipocytes showed a more subtle impact on sphingolipid levels, indicating a compensatory mechanism for ceramide generation may present (Supplementary Fig. 5a,b). *Adipor1* and *Adipor2* were downregulated by PAQR4, which may contribute to the ceramide accumulation due to the overall cellular reduction of ceramidase activities (Supplementary Fig. 6a,b).

Ceramide overload may affect glycerolipid metabolism due to fatty acid availability. We thus examined glycerolipids including triacylglycerol and phospholipids (Supplementary Fig. 7). Indeed, most of the triacylglycerol species were reduced with the exception of a few that were increased in both *Paqr4*^{ad} gWAT and sWAT (Supplementary Fig. 8a). In addition, multiple classes of glycerophospholipids and lyso-glycerophospholipids were largely increased, except that, lyso-phosphatidylserine (LPS) and lyso-phosphatidylinositol (LPI) were exclusively reduced in *Paqr4*^{ad} sWAT (Supplementary Figs. 8b and 9a,b). Notably, multiple polyunsaturated triacylglycerols were increased and saturated or monounsaturated triacylglycerols were reduced in *Paqr4*^{iAKO} gWAT and sWAT (Supplementary Fig. 10a). Another lipid classed altered by *Paqr4* deletion was phosphatidylserine with a number of species increased especially 38:6, 36:5, 36:4, 34:2 phosphatidylserine, both in gWAT and sWAT; however, other classes were largely unaltered (Supplementary Figs. 10a,b and 11a,b). Thus, ceramide homoeostasis is clearly closely associated with lipid metabolism in adipose tissues.

Ceramide signalling has a detrimental role on adipose function. We found that the presence of C2-ceramide potently inhibited adipogenesis in vitro, although we did not see an effect on the cell cycle (Extended Data Figs. 6c and 8a). Moreover, exposing mature adipocytes to C2-ceramide promoted the de-differentiation of mature adipocytes into 'fibroblast'-like cells (Extended Data Fig. 8b). By contrast, deletion of *Paqr4* diminished the inhibitory effects of C2-ceramide on adipogenesis (Extended Data Fig. 8c). Thus, PAQR4 impairs adipocyte function due to aberrant ceramide accumulation.

We therefore wondered whether blocking de novo ceramide biosynthesis could rescue the metabolic effects triggered by PAQR4 overexpression. We used myriocin, a specific inhibitor of the rate-limiting ceramide synthesis enzyme SPT[9,33] (Fig. 6b), in *Paqr4*^{ad} mice pre-exposed to 12 weeks of dox HFD. In line with previous studies, myriocin reduced weight gain and improved systemic metabolism by enhancing liver and adipose tissue function in obese mice (Fig. 6c–f and Extended Data Fig. 8d–h). Myriocin also reduced food intake both in *Paqr4*^{ad} and control mice, but only during the early treatment (Extended Data Fig. 8i). Of note, the inhibitor partially rescued the weight loss usually seen in the *Paqr4*^{ad} mice (Extended Data Fig. 8d,e). Myriocin also improved adipose tissue health and reduced liver steatosis, albeit it did not affect fat pad weights (Fig. 6c and Extended Data Fig. 8g,h). In addition, myriocin lowered hyperglycaemia and hyperinsulinaemia and improved glucose tolerance in *Paqr4*^{ad} mice (Fig. 6d–f). In sWAT, gWAT and adipocytes, ceramide synthases 2 (CERS2) is the major isoform (producing C24 ceramides), followed by CERS5 (producing C16 ceramides) (Supplementary Fig. 12a,b). We hence examined whether knockdown these *Cers* isoforms could mitigate adipose dysfunction in *Paqr4*^{ad} mice. Indeed, a local knockdown of *Cers2* or *Cers5* in sWAT mediated adipocyte size and reduced adipose fibrosis, reflecting improvements in adipose tissue function, albeit it did not rescue weight gain or sWAT mass (Fig. 6g–j and Supplementary Fig. 12c–g). Nevertheless, it further improved glucose tolerance and insulin-mediated glucose disposal in *Paqr4*^{ad} mice (Fig. 6k,l and Supplementary Fig. 8h). Therefore, PAQR4-mediated changes in the sphingolipid pathway have a critical impact on adipose tissue metabolism. Blocking ceramide biosynthesis in the context of PAQR4 overactivation diminishes the negative effects of PAQR4 on adipose tissues.

PAQR4 regulates ceramide levels by mediating CERS activity

As AdipoR1/AdipoR2 regulate ceramide metabolism through their ceramidase activities, we wondered whether PAQR4 also exhibits enzymatic activity. While we observed increases in ceramide levels by *Paqr4* overexpression (Fig. 7a), PAQR4 itself did not show ceramide synthase (CERS) or ceramidase activities (Extended Data Fig. 9a–c). We thus hypothesized that PAQR4 may act as an essential cofactor that promotes CERS activity. We hence examined whether co-expression of *Cers2* or *Cers5* together with *Paqr4* would further promote ceramide production. Indeed, *Paqr4* overexpression drastically elevated ceramide levels in cells co-expressing either *Cers2* or *Cers5* (Fig. 7a). Moreover, PAQR4 potently enhanced CERS2 activity with C24:1 CoA as a substrate as judged by an increased production of C24:1 D7-dehydroceramide and the disappearance of D7-sphinganine (Fig. 7b,d). PAQR4 also increased CERS5-induced consumption of D7-sphinganine, although no changes in C16:0 D7-dyhydroceramide levels were observed (Fig. 7c,d). Notably, CERS2 activity was also enhanced by PAQR4 using C16:0 CoA as substrate, suggesting an indirect enhancement of activity (Fig. 7b). Likewise, similar enhancement of CERS5 activity by PAQR4 was observed

Fig. 6 | Blocking ceramide de novo biosynthesis improves PAQR4-induced metabolic dysfunction. a, Sphingolipids are largely elevated in *Paqr4*^{ad} gWAT (WT, $n = 10$; *Paqr4*^{ad}, $n = 6$) and decreased in *Paqr4*^{iAKO} gWAT (*Paqr4*$^{fl/fl}$, $n = 8$; *Paqr4*^{iAKO}, $n = 15$) upon dox HFD feeding. **b**, Sphingolipid metabolic pathway. **c**, H&E staining of adipose tissues and liver after 5 weeks of vehicle (Veh) or myriocin (Myr) treatment (Veh, $n = 3$; Myr, $n = 4$). Scale bar, 200 µm. **d**–**f**, Myriocin improves hyperglycaemia (**d**), hyperinsulinaemia (**e**) and glucose tolerance (**f**) 4 weeks post-treatment ($n = 6$). In **f**, asterisk indicates comparisons between groups of WT-Veh and *Paqr4*^{ad}-Veh; hash symbol (#) indicates comparisons between groups of *Paqr4*^{ad}-Veh and *Paqr4*^{ad} Myr. **g**–**j**, Local knockdown (KD) of *Cers2* (C2) or *Cers5* (C5) via targeted CRISPR gRNAs using adeno-associated virus (AAV) improves local adipose tissue fibrosis in *Paqr4*^{ad} mice. Mice were previously fed HFD without dox for 2 weeks, and then received local injection of AAVs in the inguinal fat pads; mice were then switched to dox HFD 2 weeks post-AAV injection. Fibrosis was analysed from histological images in **g** ($n = 3$ for WT; $n = 7$ for other groups). Scale bar, 200 µm. **k**,**l**, Glucose tolerance (**k**) and insulin tolerance (**l**) tests 4 weeks post-AAV injection ($n = 7$ for each group). Asterisk indicates comparisons between groups of WT-AAV-LacZ and *Paqr4*^{ad}-AAV-LacZ; hash symbol or section sign (§) indicate comparisons between groups of *Paqr4*^{ad}-AAV-LacZ and *Paqr4*^{ad}-AAV-gC2 or *Paqr4*^{ad}-AAV-gC5, respectively. Data are mean ± s.e.m. or in box plots (line indicates the median and whiskers indicate minima to maxima) and were analysed by a two-way ANOVA (**d**–**f**,**k**,**l**), one-way ANOVA followed by Holm–Sidak multiple-comparison test (**h**–**j**) or two-tailed unpaired *t*-test (**a**). ECM, extracellular matrix.

https://doi.org/10.1038/s42255-024-01078-9

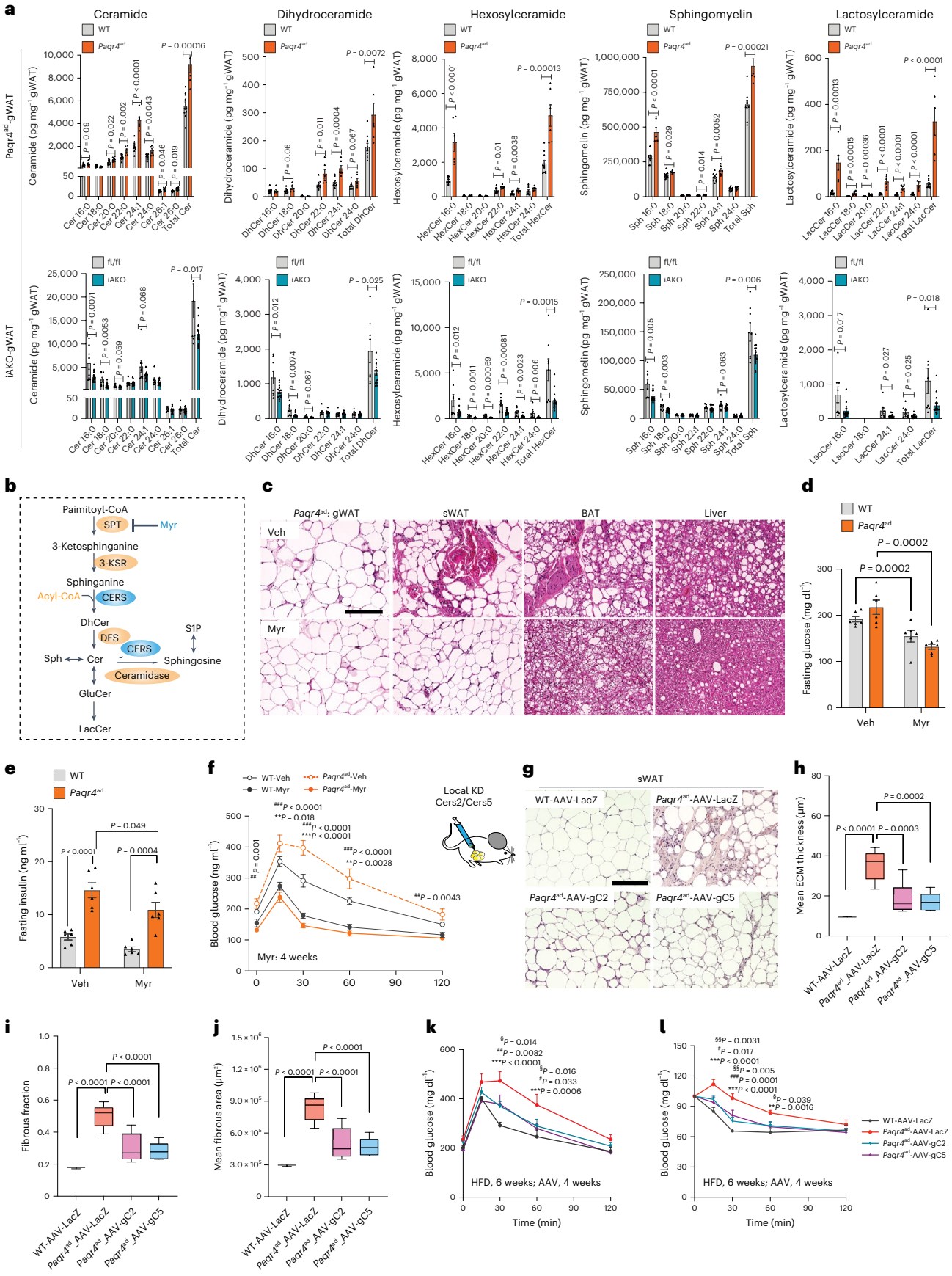

in the presence of C24:1 CoA (Fig. 7c). Sphingolipids undergo degradation to provide sphingosine for ceramide synthesis through the salvage pathway. Increased CERS5-produced C16 ceramide upon PAQR4 co-expression might indirectly originate from this pathway, as CERS5 consumes much more sphingosine than CERS2 (Extended Data Fig. 9d). Moreover, similar increases in ceramide production and enhancement of CERS2 activity were observed by in vitro combining lysates from cells individually overexpressing *Paqr4* or *Cers2*/*Cers5* (Extended Data Fig. 9e–h). This further suggests that PAQR4 is a critical cofactor for CERS. Finally, we also observed enhanced CERS2 activity by PAQR4 overexpression when analysing adipose tissue microsomes from *Paqr4*^{ad} mice (Fig. 7e).

This raises the question as to the potential mechanism by which PAQR4 may enhance CERS activity. Gene expression levels of *Cers* were largely downregulated in adipocytes and *Paqr4*^{ad} sWAT (Extended Data Fig. 10a,b). However, CERS2 protein levels were increased in both sWAT and gWAT of *Paqr4*^{ad} mice (Extended Data Fig. 10c). This increase was also observed in *Paqr4*-overexpressing cells (Fig. 7f,g). CERS2 protein accumulated upon treatment with the lysosomal inhibitor bafilomycin A1 (BFA), but was not affected by the proteasome inhibitor MG132 (Fig. 7f and Extended Data Fig. 10d,e). This suggests that CERS2 is predominantly subjected to lysosomal rather than proteasomal degradation. By using cycloheximide (CHX) or 'pulse chasing' with a CERS2–HaloTag, we determined that CERS2 has a relatively short half-life (~4 h), but its protein stability was enhanced by PAQR4 through inhibition of its lysosomal translocation and degradation (Fig. 7f,h and Extended Data Fig. 10f,g). Similarly, CERS5 protein also undergoes lysosomal degradation, but it has a relatively long half-life (>24 h), while its level was also increased by PAQR4 (Fig. 7g and Extended Data Fig. 10h,i). However, CERS5 protein levels eventually declined at 24 h post-treatment, possibly resulting from increased cellular toxicity due to accumulating C16 ceramide in presence of PAQR4 (Extended Data Fig. 10h).

From unbiased proteomics, we found that PAQR4 interacted with CERS2 in adipocytes and HEK293T cells (Fig. 7i and Supplementary Fig. 13a). The interaction was confirmed by co-immunoprecipitation (Fig. 7j and Supplementary Fig. 13b) or NanoBiT proximity assays (Supplementary Fig. 13c). Similar interactions of PAQR4 and CERS5 were also observed (Supplementary Fig. 13a,c). Moreover, we found that PAQR4 bound various ceramide species (Fig. 7k–m). In addition, PAQR4 protein levels were decreased by ceramide but increased by myriocin treatment (Fig. 7n and Supplementary Fig. 13d). Myriocin further stabilized the PAQR4–CERS2/CERS5 interactions, whereas these interactions were diminished by ceramide treatment (Fig. 7o and Supplementary Fig. 13e). Finally, in a classical Cleveland limited proteolysis assay, the presence of PAQR4 reduced the trypsin sensitivity of CERS2/CERS5. In contrast, ceramide treatment enhanced trypsin sensitivity (Fig. 7p and Supplementary Fig. 13f,g), reflecting a conformational change stimulated by PAQR4 interacting with CERS. Thus, PAQR4 plays a critical role in ceramide homoeostasis by mediating the stability and activity of CERS (Fig. 7q).

Discussion

Adipose tissue remodelling is critical for maintaining normal adipose tissue function and systemic metabolic homoeostasis. Our study also indicates that metabolic health can be influenced more significantly by the quality of adipose tissues rather than overall adiposity, a phenomenon also seen in *Ppara* or *Stk25*-deficient mice[34,35]. Many studies suggest that ceramide accumulation in multiple tissues, including adipose tissue, has considerable detrimental effects on local and systemic metabolism, and reducing ceramide levels in adipocytes has considerable beneficial effects[36]. Thus, targeting the sphingolipid pathway provides a promising strategy for multiple pathological conditions, including metabolic disorders and cancer[12,37]. Our study implicates PAQR4 as an important player in adipose tissue remodelling through its impact on ceramide metabolism. Moreover, manipulating ceramide levels by PAQR4 closely impacts adipose tissue health and systemic glucose control, highlighting PAQR4 as an attractive target in metabolic diseases.

Adipocyte cellularity is set at a young age and maintained at a relatively constant level during obesity and weight loss in adulthood[38]. However, defects in adipogenesis are frequently associated with dyslipidaemia and insulin resistance[39]. Modulating ceramide levels by PAQR4 exerts a profound impact on adipose remodelling, by both suppressing adipogenesis and triggering adipocyte de-differentiation. Our findings are in line with previous studies that ceramides robustly inhibit adipogenesis and impair adipocyte function[9,40]. Moreover, adipocyte de-differentiation may be a major cause of metabolic defects in adulthood when de novo adipogenesis is limited, particularly in subcutaneous depots[32]. We believe that adipocyte de-differentiation contributes to the regulation of inflammation and fibrosis during adipose remodelling. Adipocyte de-differentiation is frequently seen in liposarcomas where it promotes inflammation and disease development[6]. Our recent observations suggest widespread de-differentiation of mammary adipocytes in proximity to tumour lesions[8]. These de-differentiated adipocytes morph into myofibroblasts and macrophage-like cells, exerting potent pro-mitogenic effects on surrounding breast cancer cells. Of note, adipocytes fail to maintain their cellular identity and exhibit myofibroblast-like features with mitochondrial deficits upon long-term HFD feeding in mice[41,42]. This 'adipocyte-to-myofibroblast transition' occurs and bestows adipose tissue fibrosis and inflammation under severe obese conditions[43]. However, the role of adipocyte de-differentiation is probably underestimated under these conditions due to the lack of specific markers to detect this phenomenon in human samples. The seemingly reversible nature of de-differentiation events may contribute to the rebound in body fat that commonly occurs after weight loss. Yet, the exact molecular mechanisms underlying this unique plasticity of adipocytes remain largely unclear. Our findings

Fig. 7 | PAQR4 regulates ceramide levels by mediating ceramide synthase activity. a, PAQR4 (P4) increases CERS2 (C2)/CERS5 (C5)-induced ceramide (Cer) levels, as measured in lysates with overexpression of P4, C2 and C5 alone or in combination in HEK293T cells ($n = 3$ biological samples). Con, control. **b**,**c**, Enzymatic activities of CERS2 (**b**) and CERS5 (**c**) are determined from **a** using stable isotope-labelled D7-sphinganine ($n = 3$ biological samples). **d**, Consumption of D7-sphinganine ($n = 3$ biological samples). **e**, CERS2 activity in adipose microsomes (gWAT, $n = 3$; sWAT, $n = 4$ per group). **f**, CERS2 protein levels in presence of cycloheximide (CHX), MG132 or bafilomycin A1 (BFA) ($n = 3$). **g**, PAQR4 increases CERS2/CERS5 protein levels in HEK293T cells ($n = 3$ biological samples). **h**, PAQR4 increases CERS2 stability ($n = 3$ independent assays with similar results). **i**, Unbiased proteomics identified CERS2 as a PAQR4 interactor in adipocytes ($n = 3$ biological samples). **j**, PAQR4 binds CERS2 in adipocytes. Representative blots from two independent assays with similar results. **k**, Ceramides bind CERS2 and PAQR4. Representative blots from two independent assays with similar results. **l**, PAQR4 binds exogenous ceramides. **m**, PAQR4 binds endogenous ceramides. Flag–PAQR4 was pulled down from HEK293T lysates, total lipids were extracted and bound ceramides were measured by LC–MS/MS ($n = 3$ biological samples). **n**, C2-ceramide reduces, whereas myriocin increases PAQR4 levels in HEK293T cells ($n = 4$). **o**, PAQR4 interacts with CERS2/CERS5, which are stabilized by myriocin but diminished by C2-ceramide ($n = 3$). **p**, Ceramides affect the binding of PAQR4 with CERS2/CERS5. Individual PAQR4 or CERS2/CERS5 overexpressing lysates were combined and treated with ceramides before trypsin digestion ($n = 2$). **q**, Proposed model of PAQR4 in the regulation of ceramide levels. At low ceramide levels, PAQR4 binds and stabilizes CERS, thus promoting CERS activity to recover ceramide levels; at high ceramide levels, ceramides bind PAQR4, causing it to dissociate from the PAQR4–CERS complex, resulting in the lysosomal degradation of CERS. Data are mean ± s.e.m. and analysed by two-way ANOVA (**h**), one-way ANOVA (**a**–**d**) or two-tailed unpaired *t*-tests (**e**,**g**,**i**,**m**).

https://doi.org/10.1038/s42255-024-01078-9

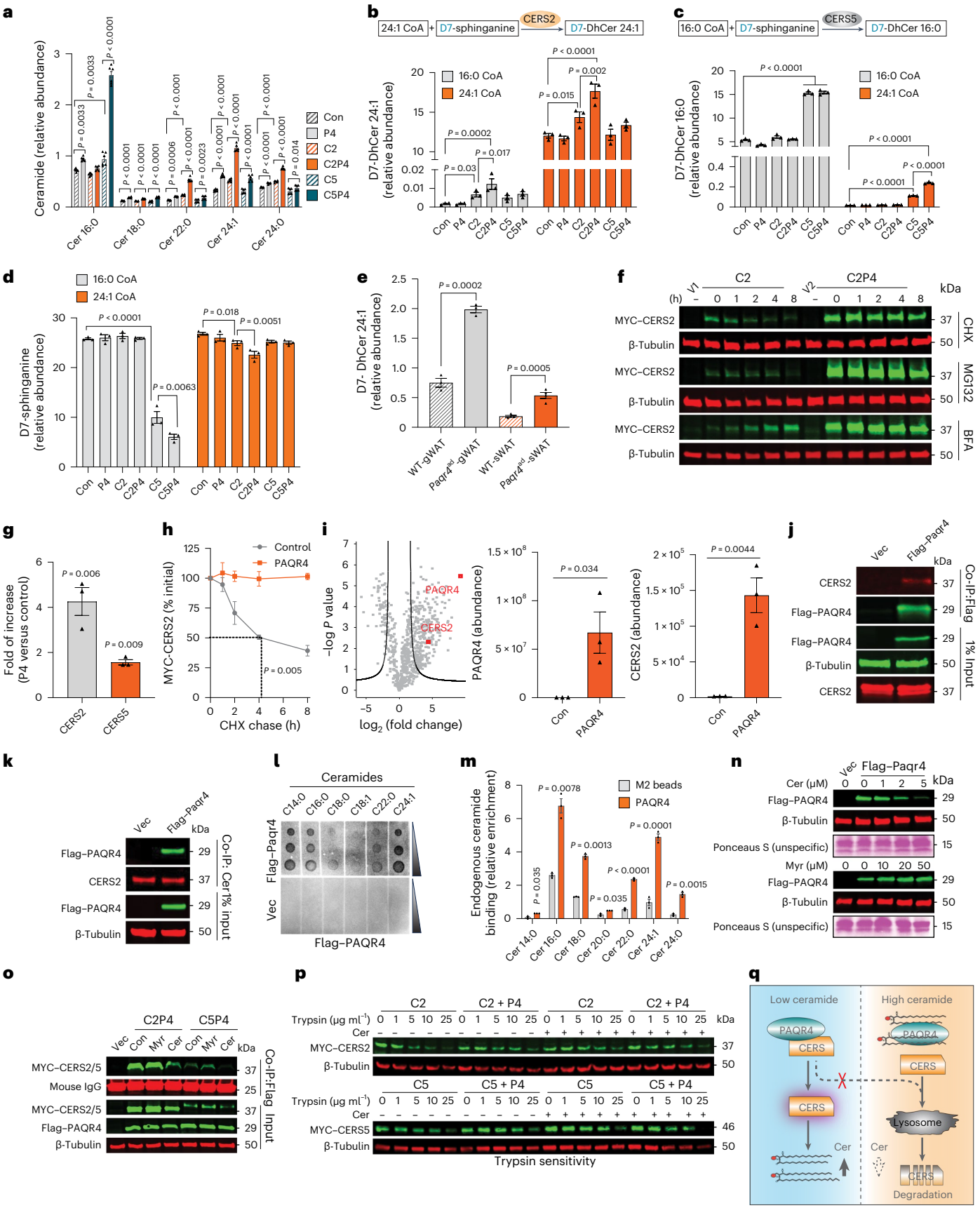

suggest that increased ceramide levels are a main trigger of adipocyte de-differentiation in *Paqr4*^{ad} mice; however, further studies are needed to see how common a phenomenon this ceramide effect is in different settings. We further found that blocking ceramide biosynthesis can improve metabolic dysfunction not only in the obese state, but also under lipodystrophic conditions.

The adipocyte progenitor pool is critical for healthy adipose tissue remodelling under metabolic stressful conditions[31,44]. It is plausible that ceramides have a critical role for the cellular homoeostasis of ASPCs and their functions. Our studies suggest that the activation of the PAQR4–ceramide axis disrupts the progenitor pool and alters their transcriptional characteristics, probably contributing to the impairment of adipocyte turnover in the *Paqr4*^{ad} mice. ASPCs are highly responsive to metabolic challenges and are also involved in fibrogenesis and immunological functions[44]. For instance, overfeeding reduced the DPP4^{+} stem population and increased CD142 (*F3*$^{+}$) fractions in visceral fat[29]. One specific visceral ASPC population referred to as 'FIPs' (fibro-inflammatory progenitors, PDGFRβ^{+}LY6C^{+}) was rapidly increased and further promoted adipose inflammation upon HFD feeding[44]. In subcutaneous fat, both PDGFRβ^{+}DPP4^{-} and PDGFRβ^{+}DPP4^{+} ASPC fractions are altered in response to hypoxia signalling in obesity and contribute to adipose tissue fibrosis[31]. Our pathway analysis reflects inflammatory and fibrogenic features in the *Paqr4*^{ad} ASPCs. It will be interesting to further examine the interactions between the de-differentiated adipocytes and the ASPCs. At this stage, it remains largely unknown how ceramide overload in adipocytes conveys signals to the progenitor cell pool.

Our findings suggest that the PAQR4–CERS axis serves as a feedback mechanism to maintain cellular ceramide levels. In this regard, PAQR4 may function as a 'ceramide sensor' by mediating CERS; however, more structural insights are needed to affirm this role of PAQR4. It is conceivable that the physical interaction of PAQR4 with CERS facilitates substrate accessibility of CERS, as PAQR4 alters their enzymatic activities, particularly for CERS2. PAQR4 does not show a preference for specific ceramide species. Rather, PAQR4 may depend on the cell type-specific expression pattern of *Cers* and the cellular status. We found both CERS2 and CERS5, the major two isoforms in adipocytes, are regulated by PAQR4. CERS activity is regulated by dimerization between different isoforms, such as dimers of CERS2 and CERS5 (ref. 45). Thus, the interactions between the two CERS isoforms and PAQR4 may lead to alterations in different ceramide species from the salvage pathway. As such, we observed multiple ceramides are altered by PAQR4, although we did not see direct effects on CERS5 activity. Notably, manipulating only certain ceramide species rather than altering the entire ceramide profile may be sufficient to cause significant metabolic effects. For instance, *Cers6* deletion reduced C16 ceramides and protected against diet-induced obesity and liver steatosis[46], whereas mice with *Cers2* haploinsufficiency reduced C24 ceramides but increased C16 ceramides in the liver as a compensatory event and promoted liver steatohepatitis[47]. While we observe more robust changes in C24 ceramides in the *Paqr4*^{ad} adipose tissues, we see a more selective reduction in C16 and C18-ceramides upon *Paqr4* deletion. Therefore, the regulation of ceramide species may be dependent on the metabolic context.

Ceramide and glycerolipid homoeostasis are closely associated[48]. We observed widespread changes for the glycerolipid composition by PAQR4 in adipose tissues. In *Paqr4*^{ad} fat, the majority of the triacylglycerol species were reduced. Excess fatty acids progress to ceramide synthesis when they fail to be incorporated into triacylglycerol storage in adipocytes. Notably, *Paqr4* deletion reduced saturated and monounsaturated triacylglycerols, but increased polyunsaturated triacylglycerols. This is in line with the notion that saturated but not unsaturated fatty acids are used for ceramide generation[49]. In addition, multiple species of glycerophospholipids and lyso-glycerophospholipids are altered by PAQR4, reflecting the tight connection between sphingolipid and glycerolipid metabolism. Many of these lipids are critical for membrane structure and signal transduction and are critically involved in the regulation of inflammation and insulin resistance[11,48]. However, the exact function of these lipids may be context-dependent, as many lipid species are regulated by PAQR4 in a distinct manner in different fat depots.

It is noteworthy that PAQR4 promotes tumorigenicity in multiple cancer types, including skin cancer, non-small cell lung cancer, prostate cancer and breast cancer[50]. Moreover, *PAQR4* expression is negatively correlated with survival rate in patients with multiple cancer types[50]. Ceramide metabolism has a profound effect on tumour growth and chemoresistance[37,51,52]; however, in cancer, the impact of ceramides may trigger dichotomous outcomes that likely depend on ceramide species and cellular responses[52]. While ceramides can induce apoptosis, increased ceramide levels and *CERS* expression can be found in different tumour types, and these can offer a distinct advantage for tumour progression[53–55]. Our findings reported here seem to be different from our previous study regarding the possible 'ceramidase' activity of PAQR4, which lowered ceramide levels in the context of tumour cells[18]. This difference may be attributed to the distinct cellular conditions, especially considering the substantial differences between highly proliferative and metabolically distinct cancer cells versus adipocytes. For instance, knockdown of PAQR4 elicited remarkable cell apoptosis in cancer cells but not in adipocytes[18]. However, ceramidases are substrate driven and can also exert the reverse activity to generate ceramides. This is dependent on the overall cellular context as well as the enzymatic microenvironment, such as substrate availability, pH values and iron levels[56–58]. Future efforts will have to determine the exact mechanism underlying the potential directional enzymatic activity of PAQR4.

Our studies have certain limitations. First, although we used inducible systems to mitigate possible developmental compensations, manipulations of gene expression levels in mice via overexpression or deletion may not accurately reflect its normal function in the native context. Second, our findings suggest that PAQR4 regulates ceramide levels by influencing the stability of CERS; generic alterations in sphingolipids and glycerolipids in membranes may also affect the half-life of CERS and the interactions of PAQR4 and CERS were determined using overexpression systems. Additionally, our proteomics data do not rule out other potential interactors with PAQR4 that may also contribute to its effects in adipocytes. Nevertheless, our findings unambiguously demonstrate that the activation of PAQR4 in adipocytes induces metabolic dysfunction.

Given the involvement of PAQR4 in mitogenesis in tumour cells, targeting PAQR4 is likely to benefit patients with metabolic diseases and different types of cancer and it may be particularly powerful in the context of obese cancer patients.

Methods

Mouse models

All mice used for experiments were on a pure C57BL/6J background. All mouse protocols were approved by the Institutional Animal Care and Use Committee of the University of Texas Southwestern (UTSW) Medical Center (APN 2015-101207G). The following mouse lines were used.

- TRE-*Paqr4*
- *Paqr4*-flox
- Adipoq-rtTA
- TRE-Cre
- *ob*/*ob*
- Flp (neomycin) deleter;
- Rosa26-mT/mG

TRE-Cre (stock no. 006234), *Lep*^{ob} (*ob*/*ob*, stock no. 000632), Flp (neomycin) deleter (stock no. 007844) and Rosa26-mT/mG mice (stock no. 007676) were obtained from The Jackson Laboratory. Adipoq-rtTA[59,60] and TRE-Paqr4 mouse lines were generated in house.

The Paqr4-flox mouse line was generated by Shanghai Model Organisms (www.modelorg.com) in collaboration with the Helmholtz Zentrum München. The details for both constructs are below:

The gene encoding mouse PAQR4, *Paqr4*, is located on chromosome 17 and features three exons. The construct used to generate *Paqr4*-transgenic and flox mice was based on the sequence of the mouse *Paqr4* gene (Ensembl ENSMUSG00000023909). To generate TRE-*Paqr4* mice, the full-length *Paqr4* coding sequence was subcloned into the TRE vector[59,60] with a rabbit β-globin 3′ untranslated region. The construct was injected into fertilized (C57BL/6N) F_1 mouse eggs at the UT Southwestern Medical Center Transgenic Core. The resulting transgenic mice were bred to C57BL/6J mice. Founders were screened for expression and specificity by crossing TRE-*Paqr4* mice with Adipoq-rtTA mice (referred to as the *Paqr4*^{ad} mice) to ensure specific and inducible expression in adipocytes.

To generate *Paqr4*-flox mice, a LoxP site was inserted in exon 3. A phosphoglycerine kinase (PGK)/Neo cassette flanked by FLP recombinase target and another LoxP site was inserted between exons 1 and 2. These mice were first crossed with Flp deleter mice to excise the PGK/Neo cassette to generate *Paqr4*$^{fl/fl}$ mice. Homozygous *Paqr4*$^{fl/fl}$ mice were then crossed with TRE-Cre and Adipo-rtTA mice to obtain inducible and adipocyte-specific iAKO (*Paqr4*$^{fl/fl}$:TRE-Cre:Adipoq-rtTA) mice, which were verified by PCR with adipose tissue-specific *Paqr4* recombination and mRNA levels.

The AdipoChaser (TRE-Cre:Adipoq-rtTA:Rosa26-mT/mG) mice were generated as previously reported[4]. Paqr4Chaser (TRE-Cre:TRE-Paqr4:Adipoq-rtTA:Rosa26-mT/mG) mice were generated by crossing TRE-Paqr4 mice with AdipoChaser mice.

The *ob*/*ob*:*Paqr4*^{ad} mice were generated by crossing *ob*/*ob* (heterozygous) mice with *Paqr4*^{ad} mice. Offspring inheriting both heterozygous *ob* mutant and TRE-*Paqr4* genes were crossed back with *ob*/*ob* mice to obtain *ob*/*ob*:*Paqr4*^{ad} (*ob*/*ob*:TRE-Paqr4:Adipoq-rtTA) mice. The *ob*/*ob* mice were used as controls.

Mouse studies

Mice were housed at 22 °C, 45% humidity with a 12-h light–dark cycle and free access to water and food unless otherwise indicated. Standard chow (Lab Diet, 5058), 60% HFD paste (S3282, BioServ), dox-containing chow (S4107, BioServ) or dox-containing HFD paste (S7067, BioServ) (600 mg kg^{-1} unless otherwise indicated), were provided for the indicated time periods. In the dox dose–response studies, HFD pastes containing 0, 50, 100, 200 and 600 mg kg^{-1} of dox were applied. Male mice and their littermate controls were used as female mice are more resistant to develop obesity and type 2 diabetes. Adipo1-rtTA mice were used as controls for *Paqr4*^{ad} mice; Adipoq-rtTA X *Paqr4*$^{fl/fl}$ were used as controls for *Paqr4*^{iAKO} mice. Experiments were started with mice at 8 weeks of age except for the in vivo adipogenic studies. To access in vivo adipogenesis, mice were fed with dox chow at adipose developmental stage on embryonic day 13 (E13)[32]. Adipose tissues were collected at E18, postnatal day 1 (P1) and 7 (P7) for histological analyses.

Adipocyte lineage tracing

Paqr4Chaser mice and their littermate controls were fed dox chow for 2 weeks to label adipocytes. For adipocyte recovery, mice were switched to standard chow (lacking dox) for 4 weeks. Adipose tissues were collected for histological analyses.

Pharmacological treatments

To avoid the effects of obesity-associated leptin resistance, in vivo leptin treatment was performed with chow-fed mice. *Paqr4*^{ad} and control mice were first fed dox chow for 14 weeks and then treated with recombinant mouse leptin (~5 μg day^{-1} per mouse, lot no. AFP1819, National Hormone & Peptide) via an ALZET osmotic minipump (Model 1002, DURECT Corporation) for another 2 weeks.

For myriocin treatment, *Paqr4*^{ad} and control mice were first fed dox HFD for 12 weeks and then switched to myriocin containing dox HFD (0.5 mg kg^{-1}, cat. no. M1177, Sigma) for another 5 weeks.

For insulin-stimulated Akt signalling studies, mice were anaesthetized and a portion of the tissues was collected (for basal conditions). Surgical threads were applied to prevent bleeding. Mice then received insulin (1 U kg^{-1} body weight) via retro-orbital injections. After 10 min, tissues of interest were quickly removed (insulin-stimulated condition) and frozen in liquid nitrogen and then −80 °C. Tissue lysates were prepared and Akt signalling was examined by immunoblotting, as described below.

Biochemical analyses

Serum insulin, leptin and adiponectin were determined by commercially available ELISA kits (for insulin, cat. no. 80-INSMS-E10, ALPCO; for leptin, cat. no. 90030, CrystalChem; for adiponectin, cat. no. EZMADP-60K, EMD Millipore) following the manufacturers' instructions. Alternatively, serum adiponectin levels were determined by western blotting as described below. Serum ALT was measured using a commercial kit (cat. no. 700260, Cayman Chemical).

Body composition analyses

Fat mass and lean mass of chow-fed and HFD-fed mice were measured using a Bruker Minispec mq10 system (Bruker).

CT imaging

Mice computed tomography (CT) imaging was performed with Mediso NanoScan. In brief, mice were anaesthetized using 3% isoflurane and then placed onto the imaging bed under 2% isoflurane during the scanning. CT images were acquired with the following parameters: X-ray power 70 kVp and 800 μA, exposure 300 ms and a binning factor of 1:4. Regions of interest were selected and fat pad volume was measured by using VivoQuant workstation (Invicro).

Cold tolerance test

Body temperature was measured by Transponder and Reader Systems (BMDS). In brief, mice were implanted with a transponder (IPTT-300) on the back and allowed to recover for 1 week. An acute cold challenge was performed by placing the mice in a temperature-controlled room (5 °C) in the absence of food. Body temperature was measured at the indicated time points with the IPTT Reader. After the acute test, mice were re-fed and acclimated to 5 °C ambient temperature for 3 weeks. Afterwards, food was removed and body temperature was measured again at the indicated time points.

Adeno-associated virus-based knockdown

Two separated CRISPR guide RNAs targeted for mouse *Cers2* (g1, GCCTCTGATGTCAAGCGAAAG; g2, GCCAGGGGTGTTGCCACATAA) and *Cers5* (g1, CAATGCTGGTTTCGCCATCGG; g2, GGAATCAGATTTCTCTGGTCG) and control *lacZ* (CTTCATACTGCACCGGGCGGG) were cloned into pX601 (Addgene 61591). Adeno-associated viruses (AAVs) (serotype of AAV2/Rec2) were produced, and the titres were determined as described previously[61]. Mice were fed HFD (without dox) for 2 weeks and then AAVs (mix of the two gRNAs) were injected locally in both sites of inguinal fat pads (5×10^{11} genome copies per site). After another 2 weeks, mice were switched to a dox HFD for the indicated time periods. The knockdown of *Cers2* was confirmed at the protein level in mouse AML12 cells but not in sWAT and *Cers5* was not confirmed by western blotting due to the lack of a viable antibody that works in tissue lysates; however, the specific guide RNAs targeting *Cers2*/*Cers5* successfully ameliorated adipose dysfunction in the *Paqr4*^{ad} mice, indicating effective gene knockdown.

Metabolic cage studies

The metabolic cage studies were performed by the UTSW Medical Center Metabolic Phenotyping Core facility as previously described[60].

In brief, mice were acclimated with single housing for 1 week and then metabolic parameters, including oxygen consumption (VO_2), CO_2 generation, food intake and physical activities were monitored and recorded using a TSE Calorimetric System. Under fasting conditions, mice were fasted at night (~18:00) and re-fed the next day (~18:00). Mice had free access to water during the whole experiment. RER, energy expenditure and carbohydrate/fat oxidation were calculated as previously described[62].

Adipose transplantation

Paqr4^{ad} and control mice were fed dox chow for 10 weeks and then received sWAT from three 4-week-old male C57BL/6J donor mice as previously described[63]. In brief, recipient mice were anaesthetized with 2–5% (v/v) isoflurane vapour with 95% O_2 (v/v) during the surgery. Donor fat pads were quickly isolated and immediately loaded to the corresponding subcutaneous site with a 16-gauge syringe. The process was performed within 10 min to minimize the ischaemia time. Mice were maintained on dox chow after the transplantation.

Systemic metabolic tests

Oral glucose tolerance tests and insulin tolerance test were performed following standard protocols[62]. In brief, mice were fasted for 6 h before administration of glucose (2 g kg^{-1} body weight by gastric gavage) or insulin (0.5 U kg^{-1} for chow diet and 0.75 U kg^{-1} body weight for HFD-fed mice by intraperitoneal (i.p.) injection). During the tests, blood glucose levels were monitored with a glucose meter at the indicated time points. In addition, blood samples were collected during oral glucose tolerance tests from tail vein during the tests. Serum levels of insulin were determined as described below.

Histology and immunostaining

Mouse tissues were dissected and fixed in 10% formalin overnight. Paraffin processing, embedding, sectioning and haematoxylin and eosin (H&E) staining as well as trichrome staining were performed by J. Sheldon at UTSW Medical Center. Adipocyte size and fibrosis including extracellular matrix thickness, fibrous area and fibrous fraction were analysed by ImageJ as previously described[8]. Immunostaining was performed following standard protocols with the following primary antibodies: Perilipin (1:700 dilution, cat. no. 20R-PP004, Fitzgerald), EGFP (1:500 dilution, cat. no. ab13970, Abcam), Mac2 (1:750 dilution, cat. no. CL8942AP, CEDARLANE), S100A4 (1:200 dilution, cat. no. ab41532, Abcam), KDEL (1:200 dilution, cat. no. ab176333, Abcam), LASS2/CERS2 (1:200 dilution, Santa Cruz, cat. no. sc-390745), insulin (1:500 dilution, cat. no. A0564, Dako) and glucagon (1:500 dilution, cat. no. ab92517, Abcam) and secondary antibodies (all 1:400 dilution), respectively: goat anti-guinea pig IgG (H+L) Alexa Fluor 594 (Invitrogen, cat. no. A11076), goat anti-chicken IgY (H+L) Alexa Fluor 488 (Invitrogen, cat. no. A11039), donkey anti-rat IgG (H+L) Alexa Fluor 488 (Invitrogen, cat. no. A21208), goat anti-rabbit IgG (H+L) Alexa Fluor Plus 488 (Invitrogen, cat. no. A32731), chicken anti-mouse IgG (H+L) Alexa Fluor 594 (Invitrogen, cat. no. A21201), goat anti-guinea pig IgG (H+L) Alexa Fluor 488 (Invitrogen, cat. no. A-11073) and donkey anti-rabbit IgG (H+L) Alexa Fluor 594 (Invitrogen, cat. no. A-21207). To determine apoptosis, TUNEL staining was performed with a commercial kit (cat. no. C10617, Invitrogen). Samples treated with DNase I were used as positive controls. Images were acquired on an Olympus FSX100 Microscope or LSM510 confocal microscope (Zeiss) and analysed with ImageJ software. Representative of 3–7 biological replicates for histological analyses were shown.

Lipidomics studies

Ceramides and other sphingolipids were quantified by liquid chromatography-electrospray ionization–tandem mass spectrometry using a Nexera ultra-high-performance liquid chromatograph coupled to an LC–MS-8060 (Shimadzu Scientific Instruments) as previously described[64]. Data are provided as pg mg^{-1} tissue for tissue samples, pg ml^{-1} for serum samples and pg μg^{-1} protein for cellular samples.

For triacylglycerol profiling, an equivalent to 500 μg of adipose tissue lipid extract containing 20 μl of SPLASH LIPIDOMIX Mass Spec Standard (diluted 1:10 in methanol, Avanti Polar Lipids) were reconstituted in 225 μl of organic solvent mixture (CH_2Cl_2:methanol 25:200, *v*/*v*). Then, 0.3 μl of final extract was injected onto a Nexera LC-40 UHPLC system coupled to a Shimadzu LC–MS-9030 Q-TOF mass spectrometer (Shimadzu Scientific Instruments). Triacylglycerol species were resolved on a reverse-phase C18 column as described by Rampler et al.[65] Triacylglycerols were identified as ammoniated adducts in positive-ion mode (putative identification of *m*/*z* at 5 ppm tolerance via cross-referencing with the LIPID MAPS database; the LIPID MAPS Lipidomics Gateway, https://www.lipidmaps.org/). For phospholipid profiling, samples containing an equivalent to 10 mg of adipose tissue lipid extract were analysed as previously described[61]. For triacylglycerols and phospholipids, relative abundance was presented.

Fluorescent enzymatic assay

CERS assays were performed as previously described[66]. In brief, HEK293T cells were transfected with pCMV-3×Flag-Paqr4 or empty vector for 48 h. Cell lysates were prepared in a buffer containing 20 mM HEPES (pH 7.4), 25 mM KCl, 2 mM $MgCl_2$, 250 mM sucrose and protease 1× inhibitor cocktail (Thermo Fisher Scientific). Then, 50 μg lysate were used in the assay in a reaction buffer containing 20 mM HEPES (pH 7.4), 25 mM KCl, 2 mM $MgCl_2$, 0.5 mM dithiothreitol, 0.1% (*w*/*v*) fatty acid-free BSA, 10 μM NBD-sphinganine (Avanti) and 50 μM fatty acid-CoA (Avanti). The reactions were conducted at 35 °C for 30 min and lipids were extracted with chloroform:methanol (2:1). Samples were resolved in chloroform:methanol:H_2O (8:1:0.1, *v*/*v*/*v*) with aluminium-backed Silica Gel 60 TLC plates (Millipore). Alkaline ceramidase assays were examined as previously described[67]. In brief, 100 μg lysate was used in the assay in a buffer containing 25 mM Tris-HCl buffer (pH 8.5) and 5 μM NBD-C12 ceramide (Cayman). The reactions were carried out at 37 °C for 16 h. Lipids were then extracted with chloroform:methanol (2:1) and resolved in a TLC plate as above with a developing buffer containing chloroform:methanol:25% ammonia (90:20:0.5, *v*/*v*/*v*). Fluorescence-labelled products in the plate were detected with a ChemiDoc MP Imaging System (Bio-Rad).

LC–MS/MS-based CERS enzymatic assay

As CERS2 and CERS5 are the major isoforms of ceramide synthases in adipocytes, which mainly produce C24 and C16 ceramides, respectively, we examined the effect of PAQR4 on the enzymatic activities of CERS2 and CERS5. In brief, HEK293T cells were co-transfected with pRB–MYC–Cers2 or pRB–MYC–Cers5 along with pCMV–3×Flag–Paqr4 or control empty vector for 48 h. Cell lysates were prepared and used in the enzymatic assay as aforementioned. In the assays with combined lysates, individual lysates overexpressed CERS2 or CERS5 were combined with PAQR4-expressed lysates for 30 min on ice, respectively and then the enzymatic assay was performed as mentioned previously.

To measure the effect of PAQR4 on ceramide synthase activity in vivo, adipose tissue microsomes isolated from *Paqr4*^{ad} and WT control mice were used. In brief, mice were fed with dox chow for 2 weeks and gWAT and sWAT were dissected. Samples from three mice were pooled together and homogenized in the lysis buffer mentioned above by using a Dounce homogenizer. Samples were then centrifuged at 680*g* for 15 min and the fat-free extract was collected, followed by centrifugation at 10,000*g* for 20 min. The clear, post-mitochondrial supernatant fraction was collected and further centrifuged at 105,000*g* for 1 h. The final pellet which provided the microsomal fraction was resuspended in the lysis buffer and used for the activity assay. A total of 25 μg microsomal protein was used in each reaction.

Ceramide formation with the cell lysates and adipose tissue microsomes were determined using LC–MS/MS. The assay was

conducted essentially as the fluorescent assay described above except that NBD-sphinganine was replaced with stable isotope-labelled D7-sphinganine (Avanti). C24:1 CoA and C16:0 CoA were used as substrates for accessing CERS2 and CERS5's activity, respectively. Products of C24:1 and C16:0 D7-dehydroceamide (D7-DhCer) that are generated from the substrates D7-sphinganine and C24:1 or C16:0 acyl-CoA, which are mainly utilized by CERS2 and CERS5, respectively, reflecting their enzymatic activities. Peak area of metabolite versus internal standard was calculated. Internal standards were all added at 0.25 μM. The area ratios directly correlate with concentrations and were used to present the data as relative abundance.

Stromal vascular cells and adipocyte differentiation

Paqr4^{ad} and iAKO mice and their respective littermate control mice were used. Stromal vascular fraction (SVF) cells were isolated from sWAT as previously described[62]. To induce adipogenesis, confluent SVF cells were switched to adipogenic induction medium contained 5 μg ml^{-1} insulin, 1 μM dexamethasone, 500 μM isobutylmethylxanthine and 0.5 μM rosiglitazone. Cells were supplied with maintenance medium containing 5 μg ml^{-1} insulin 2 days after induction. To test the effect of PAQR4 on adipogenesis, dox (2.5 μg ml^{-1}) was added to the adipogenic induction medium to induce *Paqr4* expression or deletion and maintained at the same dose during the differentiation process. C2-ceramide (5 μM, cat. no. sc-201375, Santa Cruz) was added from the beginning of differentiation to examine its effect on adipogenesis. To induced de-differentiation, SVF cells were first differentiated into mature adipocytes and C2-ceramide (5 μM) was added from day 8 post-differentiation. Adipogenesis was assessed by Oil Red O staining as previously described[68].

Flow cytometry

Subcutaneous adipose tissues (sWAT) from two mice were pooled for each sample. To examine adipocyte de-differentiation, SVF cells were isolated from Paqr4Chaser and AdipoChaser control mice fed with dox chow for 2 weeks. Red blood cells in the SVF pellets were lysed with RBC lysis buffer (Sigma). For blocking, cells were incubated in 2% FBS/PBS blocking buffer containing anti-mouse CD16/CD32 Fc Block (1:200 dilution) for 15 min on ice. Cells were stained with anti-mouse antibodies against BV421-CD31 (cat. no. 102423, BioLegend), BV421-CD45 (cat. no. 103133, BioLegend) and APC-PDGFRβ (cat. no. 136007, BioLegend) at 1:100 dilution for 30 min on ice in the dark. After incubation, the cells were washed twice with 2% FBS/PBS and analysed using a BD Biosciences LSR II cytometer (UTSW Flow Cytometry Core Facility). To quantify the ASPCs, SVF cells were stained and analysed as above using the following antibodies: PE/Cy7-CD31 (cat. no. 102418, BioLegend, 1:600 dilution), PE/Cy7-CD45 (cat. no. 103114, BioLegend, 1:600 dilution), PE/Cy7-TER119 (cat. no. 116222, BioLegend, 1:600 dilution), FITC-CD26/DPP4 (cat. no. 137806, BioLegend, 1:200 dilution), PE-CD54/ICAM1 (cat. no. 116108, BioLegend, 1:100 dilution), BV711-SCA1/LY6a (cat. no. 108131, BioLegend, 1:600 dilution) and APC-CD142/F3 (cat. no. 50413-R001, SinoBiological, 1:100 dilution) as previously described[29]. CD142 was preconjugated with APC using APC Conjugation kit - Lightning-Link (cat. no. ab201807, Abcam). Live single cells were first gated for ASPCs with Lin$^-$(CD31$^-$/CD45$^-$/TER119$^-$) SCA1$^+$ and then gated for CD142$^+$ and CD142$^-$ populations. The CD142$^-$ population was further gated for ICAM1$^+$ and DPP4$^+$ subpopulations. Flow cytometry plots were generated using FlowJo (v.10.8.1).

Single-cell RNA sequencing

Paqr4^{ad} and littermate control mice at 8 weeks of age were fed with dox HFD for 2 weeks. Inguinal adipose tissues were dissected and pulled together from three mice for each group. SVF cells were isolated, stained with anti-CD45-BV421 antibody (cat. no.103133, BioLegend) to exclude leucocytes. CD45$^-$ cells were sorted by flow cytometry (BD Biosciences FACSAria) and used for scRNA-seq. Sample preparation and library construction were performed following standard procedures provided from 10x Genomics Chromium as described previously[8]. Sequencing was conducted on an Illumina NovaSeq 6000 system by Novogene, yielding ~220 million reads per sample. Data pre-processing was conducted with Cell Ranger (v.7.0.0) with default parameters, including sample demultiplexing, alignment, unique molecular identifier collapsing, counting and initial quality control. Seurat R package (v.4.1.1; Satija Laboratory, Seurat; https://satijalab.org/seurat/) was further used for data quality control and data visualizing in RStudio (v.2023.06.2+561). In brief, cells with very few genes (<200), genes with non-zero counts in at most three cells or unexpected very high feature counts (>8,000) were filtered out. The majority of cells were *Pdgfra*$^+$, a canonical marker for ASPCs. These cells (1,368 cells from *Paqr4*^{ad} and 1,173 cells from control data) were aggregated for single-cell transcriptional comparisons. ASPCs were clustered into three subpopulations based on the upregulated signature genes and consensus knowledge of canonical gene markers of adipose stem cells. GO enrichment analyses were conducted between control and *Paqr4*^{ad} samples for each subpopulation with DAVID 2021 (https://david.ncifcrf.gov/).

Cell cycle analysis

Upon starting adipocyte differentiation, SVF cells were infected with AAVs (pAAVK CAG–(3×) Flag–Paqr4 or pAAVK CAG–EGFP, multiplicity of infection (MOI) of 10, 000 genome copies per cell) in the presence of vehicle or C2-ceramide (5 μM) for 2 days. Cells were collected and fixed in ice-cold 70% ethanol, and then cells were treated with 100 μg ml^{-1} ribonuclease for 5 min at room temperature. After staining with propidium iodide (50 μg ml^{-1}), the cell cycle stage was analysed by flow cytometry.

Assessment of protein degradation

To determine the effect of PAQR4 on the protein stability of CERS2 and CERS5, HEK293T cells were co-transfected with pRB–MYC–Cers2 or pRB–MYC–Cers5 along with pCMV–3×Flag–Paqr4 or control empty vector for 40 h and then treated with 100 μg ml^{-1} cycloheximide, 10 μM MG132 or 1 μM bafilomycin A1 (Sigma), respectively, for the indicated time points. Alternatively, HEK293A cells transfected with pcDNA3.1(+)–Cers2–Halo or pcDNA3.1(+)–Cers2–Halo, with pcDNA3.1(+)–SNAP–Paqr4 or control vectors for 24 h. Cells were then treated with 1 μM bafilomycin A1 for 8 h. CERS2 or CERS5 was labelled with HaloTag TMR ligand (cat. no. G8251, Promega) and PAQR4 was labelled with SNAP-Cell Oregon Green (cat. no.S9104, New England BioLabs). Cells were then fixed and stained with anti-LAMP1 antibody (1:200 dilution, Cell Signaling, cat. no. 9091). Images were acquired using a confocal microscope. For 'pulse tracing' studies, CERS2 and PAQR4 were first labelled as described above and images were taken at the indicated time points. Florescent density was measured using ImageJ software.

Protein–protein interaction studies

Unbiased proteomics was performed to identify potential PAQR4 interactors. For differentiated adipocytes, cells were infected with AAVs (pAAVK CAG–(3×) Flag–Paqr4 or pAAVK CAG–eGFP, MOI of 10,000 genome copies per cell) for 2 days. For HEK293T, cells were transfected with pCMV–3×Flag–Paqr4 or a control empty vector for 2 days. Cell lysates were immunoprecipitated with anti-Flag M2 magnetic beads (Sigma, cat. no. M8823), followed by SDS–PAGE and analysed by mass spectrometry. Data were processed with the Perseus software platform (v.2.0.11) (https://maxquant.net/perseus/), with fold change >2 and FDR < 0.01. Undetermined values were imputed with the sample minimum.

To examine the interaction of PAQR4 and ceramide synthases, cells overexpressing MYC–CERS2 or MYC–CERS5 combined with Flag–PAQR4 for 24 h were treated with 10 μM myriocin or 5 μM C2-ceramide for another 24 h. Cell lysates were immunoprecipitated with mouse

anti-Flag M2 magnetic beads, western blotted and analysed with rabbit anti-MYC antibody. The binding of Flag–PAQR4 and endogenous CERS2 was examined both in adipocytes and HEK293T cells. After immunoprecipitation, samples were subjected to immunoblotting and detected by rabbit anti-CERS2 antibodies as described below. The interaction of ceramides with Flag–PAQR4 and CERS2 was tested using anti-ceramide IgM (Enzo Life Sciences, cat. no. ALX-804-196-T050) for immunoprecipitation and further detected with anti-Flag and CERS2 antibodies, respectively.

For NanoBiT protein–protein interaction, HEK293A cells were transfected with pcDNA3.1(+)–N-SmBit–Paqr4 together with pcDNA3.1(+)–Cers2–C-LgBit or pcDNA3.1(+)–Cers2–C-LgBit overnight. Luminescence was detected using the Nano-Glo Live Cell Assay System (Promega). Co-transfection of FRB–LgBiT and FKBP–SmBiT vector was severed as a positive control, with the stimulation of rapamycin (30 nM).

Trypsin sensitivity assay

A trypsin sensitivity assay was performed as previously described[69]. In brief, HEK293T cells were co-transfected with pRB–MYC–Cers2 or pRB–MYC–Cers5 along with pCMV–3×Flag–Paqr4 or control empty vector for 24 h and then cells were treated with C2-ceramide (5 μM) overnight. Lysates were prepared with lysis buffer containing 50 mM Tris-HCl (pH 8.0), 150 mM NaCl, 1% NP-40, 2 μM Z-VAD-fmk, 20 μM MG132 and 5 μM bafilomycin A1. Trypsin digestion was performed at various doses as indicated at room temperature for 15 min. The reactions were terminated by adding 2× SDS sample buffer containing 100 mM dithiothreitol and 8 mM phenylmethylsulfonyl fluoride. Samples were boiled for 5 min and subjected to SDS–PAGE and immunoblotting. For the assays with combined lysates, individual PAQR4 or CERS2/CERS5 overexpressed lysates were first combined and treated with C24:1 and C16:0 ceramides (50 μM) for 45 min before trypsin digestion.

Lipid overlay assay

A lipid overlay assay was performed as previously described[54]. In brief, a panel of natural ceramides (Cayman) were spotted on PVDF membranes, ranging 0.5–2 nmol and left to dry at room temperature for 60 min. Membranes were then blocked with 3% BSA in PBS containing 0.1% Tween 20 (*v*/*v*). Adipocyte lysates with Flag–Paqr4 overexpressed were added and incubated at 4 °C overnight. Bound PAQR4 was detected with rabbit anti-Flag antibody.

Western blotting

Tissues and cells were lysed and protein concentrations were determined using the BCA method. Tissue or cell lysates (10 μg per lane) or serum samples (0.5 μl per lane) were boiled at 95 °C in a protein-loading buffer and separated on 4–12% SDS–PAGE gels (Bio-Rad). Antibodies against mouse adiponectin (1:1,000 dilution, homemade), phospho-Akt (Ser473) (1:1,000 dilution, cat. no. 4060, Cell Signaling), Akt (pan) (1:1,000 dilution, cat. no. 2920, Cell Signaling), MYC tag (1:1,000 dilution, cat. no. 2278T, Cell Signaling), Flag-tag (1:1,000 dilution, cat. no. 14793, Cell Signaling), CERS2 (1:1,000 dilution, cat. no. HPA027262, Sigma) and β-tubulin (1:1,000 dilution, cat. no. 86298, Cell Signaling) followed by the respective fluorescence-conjugated secondary antibodies (1:10,000 dilution, IRDye, LI-COR): 800CW goat anti-rabbit IgG (cat. no. 926-32211), 680RD donkey anti-mouse IgG (cat. no. 926-68072), 800CW goat anti-mouse IgG (cat. no. 926-32210) or 680RD goat anti-rabbit IgG (cat. no. 926-68071) were used. Images were acquired and the fluorescent density was quantified by utilizing a LI-COR Odyssey Imager (LI-COR) or ImageJ.

RNA isolation and qRT–PCR

Total RNA was extracted by using the traditional Trizol method (Invitrogen). Quantitative gene expression was performed by two-step quantitative RT–PCR using iScript cDNA Synthesis kits (cat. no. 170-8891, Bio-Rad) and SYBR Green PCR Master Mix (Applied Biosystems) with QuantStudio 5 and 6 Flex Real-Time PCR System. mRNA expression levels were determined using the ΔΔCT method and normalized to the housekeeping genes *Rps16* and *Rps18*. The primers used are listed in Supplementary Table 1.

Statistical analyses

No statistical methods were used to predetermine sample sizes, but our sample size is similar to previous publications with similar procedures. The number of experimental repeats or mice (*n*) are indicated in the figure legends. All results from the representative experiments described in this study were reproduced at least twice in independent experiments. Studies were not performed blinded as mouse genotypes were predetermined. Mice were randomly grouped based on their genotypes for treatments. Mice in the transgenic cohorts that occasionally have malocclusions were excluded from studies, as this affects their nutritional status. Two sample in the lipidomics analysis of sWAT was excluded due to sample loss. All data were expressed as mean ± s.e.m. Data distribution was assumed to be normal but this was not formally tested. For two independent datasets, a two-tailed unpaired Student's *t*-test was used. For multiple comparisons, one-way or two-way analysis of variance (ANOVA) were used followed by a Holm–Sidak post hoc test. The statistical analyses were performed with GraphPad Prism 8.0 (GraphPad Software).

Reporting summary

Further information on research design is available in the Nature Portfolio Reporting Summary linked to this article.

Data availability

scRNA-seq data are available in the Gene Expression Omnibus (GSE246712). All other data from this study are available with this paper. Source data are provided with this paper.

References

1. Zhu, Q. & Scherer, P. E. Immunologic and endocrine functions of adipose tissue: implications for kidney disease. *Nat. Rev. Nephrol.* **14**, 105–120 (2018).
2. Zhu, Q., An, Y. A. & Scherer, P. E. Mitochondrial regulation and white adipose tissue homeostasis. *Trends Cell Biol.* **32**, 351–364 (2022).
3. Wang, Q. A. et al. Reversible de-differentiation of mature white adipocytes into preadipocyte-like precursors during lactation. *Cell Metab.* **28**, 282–288.e3 (2018).
4. Zhang, Z. et al. Dermal adipose tissue has high plasticity and undergoes reversible dedifferentiation in mice. *J. Clin. Invest.* **129**, 5327–5342 (2019).
5. Shook, B. A. et al. Dermal adipocyte lipolysis and myofibroblast conversion are required for efficient skin repair. *Cell Stem Cell* **26**, 880–895.e6 (2020).
6. Bi, P. et al. Notch activation drives adipocyte dedifferentiation and tumorigenic transformation in mice. *J. Exp. Med.* **213**, 2019–2037 (2016).
7. Liu, S. C. et al. Epstein–Barr virus induces adipocyte dedifferentiation to modulate the tumor microenvironment. *Cancer Res.* **81**, 3283–3294 (2021).
8. Zhu, Q. et al. Adipocyte mesenchymal transition contributes to mammary tumor progression. *Cell Rep.* **40**, 111362 (2022).
9. Chaurasia, B. et al. Adipocyte ceramides regulate subcutaneous adipose browning, inflammation, and metabolism. *Cell Metab.* **24**, 820–834 (2016).
10. Scherer, P. E. The many secret lives of adipocytes: implications for diabetes. *Diabetologia* **62**, 223–232 (2019).
11. Turpin-Nolan, S. M. & Brüning, J. C. The role of ceramides in metabolic disorders: when size and localization matters. *Nat. Rev. Endocrinol.* **16**, 224–233 (2020).

12. Chaurasia, B. et al. Targeting a ceramide double bond improves insulin resistance and hepatic steatosis. *Science* **365**, 386–392 (2019).
13. Kupchak, B. R., Garitaonandia, I., Villa, N. Y., Smith, J. L. & Lyons, T. J. Antagonism of human adiponectin receptors and their membrane progesterone receptor paralogs by TNFα and a ceramidase inhibitor. *Biochemistry* **48**, 5504–5506 (2009).
14. Tang, Y. T. et al. PAQR proteins: a novel membrane receptor family defined by an ancient 7-transmembrane pass motif. *J. Mol. Evol.* **61**, 372–380 (2005).
15. Yamauchi, T., Iwabu, M., Okada-iwabu, M. & Kadowaki, T. Adiponectin receptors: a review of their structure, function and how they work. *Best. Pract. Res. Clin. Endocrinol. Metab.* **28**, 15–23 (2014).
16. Holland, W. L. et al. Receptor-mediated activation of ceramidase activity initiates the pleiotropic actions of adiponectin. *Nat. Med.* **17**, 55–63 (2011).
17. Garitaonandia, I., Smith, J. L., Kupchak, B. R. & Lyons, T. J. Adiponectin identified as an agonist for PAQR3/RKTG using a yeast-based assay system. *J. Recept. Signal Transduct.* **29**, 67–73 (2009).
18. Pedersen, L. et al. Golgi-localized PAQR4 mediates antiapoptotic ceramidase activity in breast cancer. *Cancer Res.* **80**, 2163–2174 (2020).
19. Xu, D. et al. PAQR3 modulates cholesterol homeostasis by anchoring Scap/SREBP complex to the Golgi apparatus. *Nat. Commun.* **6**, 8100 (2015).
20. Jiang, Y. et al. Functional cooperation of RKTG with p53 in tumorigenesis and epithelial-mesenchymal transition. *Cancer Res.* **71**, 2959–2968 (2011).
21. Yu, X., Li, Z., Chan, M. T. V. & Wu, W. K. K. PAQR3: a novel tumor suppressor gene. *Am. J. Cancer Res.* **5**, 2562–2568 (2015).
22. Zhang, H. et al. PAQR4 has a tumorigenic effect in human breast cancers in association with reduced CDK4 degradation. *Carcinogenesis* **39**, 439–446 (2018).
23. Okada-Iwabu, M. et al. A small-molecule AdipoR agonist for type 2 diabetes and short life in obesity. *Nature* **503**, 493–499 (2013).
24. Beals, J. W. et al. Increased adipose tissue fibrogenesis, not impaired expandability, is associated with nonalcoholic fatty liver disease. *Hepatology* **74**, 1287–1299 (2021).
25. Kusminski, C. M. et al. MitoNEET-driven alterations in adipocyte mitochondrial activity reveal a crucial adaptive process that preserves insulin sensitivity in obesity. *Nat. Med.* **18**, 1539–1551 (2012).
26. An, Y. A. et al. The mitochondrial dicarboxylate carrier prevents hepatic lipotoxicity by inhibiting white adipocyte lipolysis. *J. Hepatol.* **75**, 387–399 (2021).
27. Ferrero, R., Rainer, P. & Deplancke, B. Toward a consensus view of mammalian adipocyte stem and progenitor cell heterogeneity. *Trends Cell Biol.* **30**, 937–950 (2020).
28. Burl, R. B. et al. Deconstructing adipogenesis induced by β3-adrenergic receptor activation with single-cell expression profiling. *Cell Metab.* **28**, 300–309.e4 (2018).
29. Merrick, D. et al. Identification of a mesenchymal progenitor cell hierarchy in adipose tissue. *Science* **364**, aav2501 (2019).
30. Schwalie, P. C. et al. A stromal cell population that inhibits adipogenesis in mammalian fat depots. *Nature* **559**, 103–108 (2018).
31. Shao, M. et al. Pathologic HIF1α signaling drives adipose progenitor dysfunction in obesity. *Cell Stem Cell* **28**, 685–701.e7 (2021).
32. Wang, Q. A., Tao, C., Gupta, R. K. & Scherer, P. E. Tracking adipogenesis during white adipose tissue development, expansion and regeneration. *Nat. Med.* **19**, 1338–1344 (2013).
33. Ussher, J. R. et al. Inhibition of de novo ceramide synthesis reverses diet-induced insulin resistance and enhances whole-body oxygen consumption. *Diabetes* **59**, 2453–2464 (2010).
34. Amrutkar, M. et al. Genetic disruption of protein kinase STK25 ameliorates metabolic defects in a diet-induced type 2 diabetes model. *Diabetes* **64**, 2791–2804 (2015).
35. Guerre-Millo, M. et al. PPAR-α-null mice are protected from high-fat diet-induced insulin resistance. *Diabetes* **50**, 2809–2814 (2001).
36. Xia, J. Y. et al. Targeted induction of ceramide degradation leads to improved systemic metabolism and reduced hepatic steatosis. *Cell Metab.* **22**, 266–278 (2015).
37. Ogretmen, B. Sphingolipid metabolism in cancer signalling and therapy. *Nat. Rev. Cancer* **18**, 33–50 (2017).
38. Spalding, K. L. et al. Dynamics of fat cell turnover in humans. *Nature* **453**, 783–787 (2008).
39. Ghaben, A. L. & Scherer, P. E. Adipogenesis and metabolic health. *Nat. Rev. Mol. Cell Biol.* **20**, 242–258 (2019).
40. Sprott, K. M., Chumley, M. J., Hanson, J. M. & Dobrowsky, R. T. Decreased activity and enhanced nuclear export of CCAAT-enhancer-binding protein β during inhibition of adipogenesis by ceramide. *Biochem. J.* **365**, 181–191 (2002).
41. Jones, J. E. C. et al. The adipocyte acquires a fibroblast-like transcriptional signature in response to a high fat diet. *Sci. Rep.* **10**, 1–15 (2020).
42. Roh, H. C. et al. Adipocytes fail to maintain cellular identity during obesity due to reduced PPARγ activity and elevated TGFβ-SMAD signaling. *Mol. Metab.* **42**, 101086 (2020).
43. Kruglikov, I. L. & Scherer, P. E. Dermal adipocytes: from irrelevance to metabolic targets? *Trends Endocrinol. Metab.* **27**, 1–10 (2016).
44. Shan, B. et al. Perivascular mesenchymal cells control adipose-tissue macrophage accrual in obesity. *Nat. Metab.* **2**, 1332–1349 (2020).
45. Laviad, E. L., Kellys, S., Merrill, A. H. & Futerman, A. H. Modulation of ceramide synthase activity via dimerization. *J. Biol. Chem.* **287**, 21025–21033 (2012).
46. Hammerschmidt, P. et al. CerS6-derived sphingolipids interact with Mff and promote mitochondrial fragmentation in obesity. *Cell* **177**, 1536–1552.e23 (2019).
47. Raichur, S. et al. CerS2 haploinsufficiency inhibits β-oxidation and confers susceptibility to diet-induced steatohepatitis and insulin resistance. *Cell Metab.* **20**, 687–695 (2014).
48. Rodriguez-Cuenca, S., Pellegrinelli, V., Campbell, M., Oresic, M. & Vidal-Puig, A. Sphingolipids and glycerophospholipids – The 'ying and yang' of lipotoxicity in metabolic diseases. *Prog. Lipid Res.* **66**, 14–29 (2017).
49. Volkmar, N. et al. Regulation of membrane fluidity by RNF145 - triggered degradation of the lipid hydrolase ADIPOR2. *EMBO J.* **41**, 1–22 (2022).
50. Wang, K. et al. Pan-cancer analysis of the prognostic and immunological role of PAQR4. *Sci. Rep.* **12**, 1–16 (2022).
51. Brachtendorf, S., El-Hindi, K. & Grösch, S. Ceramide synthases in cancer therapy and chemoresistance. *Prog. Lipid Res.* **74**, 160–185 (2019).
52. Morad, S. A. F. & Cabot, M. C. Ceramide-orchestrated signalling in cancer cells. *Nat. Rev. Cancer* **13**, 51–65 (2013).
53. Li, Y. et al. Ceramides increase fatty acid utilization in intestinal progenitors to enhance stemness and increase tumor risk. *Gastroenterology* **165**, 1136–1150 (2023).
54. Zhang, Y. et al. C24-ceramide drives gallbladder cancer progression through directly targeting phosphatidylinositol 5-phosphate 4-kinase type-2 γ to facilitate mammalian target of rapamycin signaling activation. *Hepatology* **73**, 692–712 (2021).

55. Dany, M. & Ogretmen, B. Ceramide induced mitophagy and tumor suppression. *Biochim. Biophys. Acta Mol. Cell Res.* **1853**, 2834–2845 (2015).
56. Inoue, T. et al. Mechanistic insights into the hydrolysis and synthesis of ceramide by neutral ceramidase. *J. Biol. Chem.* **284**, 9566–9577 (2009).
57. Okino, N. et al. The reverse activity of human acid ceramidase. *J. Biol. Chem.* **278**, 29948–29953 (2003).
58. El Bawab, S. et al. Biochemical characterization of the reverse activity of rat brain ceramidase. A CoA-independent and fumonisin B1-insensitive ceramide synthase. *J. Biol. Chem.* **276**, 16758–16766 (2001).
59. Zhu, Q. et al. Suppressing adipocyte inflammation promotes insulin resistance in mice. *Mol. Metab.* **39**, 1–11 (2020).
60. Deng, Y. et al. Adipocyte Xbp1s overexpression drives uridine production and reduces obesity. *Mol. Metab.* **11**, 1–17 (2018).
61. Zhang, Z. et al. Adipocyte iron levels impinge on a fat-gut crosstalk to regulate intestinal lipid absorption and mediate protection from obesity. *Cell Metab.* **33**, 1624–1639.e9 (2021).
62. Zhu, Q. et al. Adipocyte-specific deletion of Ip6k1 reduces diet-induced obesity by enhancing AMPK-mediated thermogenesis. *J. Clin. Invest.* **126**, 4273–4288 (2016).
63. Zhang, Z. et al. Insulin resistance and diabetes caused by genetic or diet-induced KBTBD2 deficiency in mice. *Proc. Natl Acad. Sci. USA* **113**, E6418–E6426 (2016).
64. Kusminski, C. M. et al. A novel model of diabetic complications: adipocyte mitochondrial dysfunction triggers massive β-cell hyperplasia. *Diabetes* **69**, 313–330 (2020).
65. Rampler, E. et al. Simultaneous non-polar and polar lipid analysis by on-line combination of HILIC, RP and high resolution MS. *Analyst* **143**, 1250–1258 (2018).
66. Kim, H. J., Qiao, Q., Toop, H. D., Morris, J. C. & Don, A. S. A fluorescent assay for ceramide synthase activity. *J. Lipid Res.* **53**, 1701–1707 (2012).
67. Tani, M., Okino, N., Mitsutake, S. & Ito, M. Specific and sensitive assay for alkaline and neutral ceramidases involving C12-NBD-ceramide. *J. Biochem.* **125**, 746–749 (1999).
68. Zhu, Q., Ghoshal, S., Tyagi, R. & Chakraborty, A. Global IP6K1 deletion enhances temperature modulated energy expenditure which reduces carbohydrate and fat induced weight gain. *Mol. Metab.* **6**, 73–85 (2017).
69. Ninagawa, S. et al. Forcible destruction of severely misfolded mammalian glycoproteins by the non-glycoprotein ERAD pathway. *J. Cell Biol.* **211**, 775–784 (2015).

Acknowledgements

We thank staff at the UTSW Animal Resource Center, Histology Core, Metabolic Phenotyping Core, the Live Cell Imaging Core, Transgenic Core, Proteomics Core and Flow Cytometry Facility for their excellent assistance with experiments performed here. We thank Helmholtz Zentrum München for their support and Matthias Tschöp for helpful discussions. We also thank Shimadzu Scientific Instruments for the collaborative efforts in mass spectrometry technology resources. This study was supported by US National Institutes of Health (NIH) grants RC2-DK118620, R01-DK55758, R01-DK099110, R01-DK127274, P01 AG051459 and R01-DK131537 to P.E.S., as well as NIDDK-NORC P30-DK127984; NIH grant R00-AG068239, R01-DK138035 and a Voelcker Fund Young Investigator Award to S.Z., DFG Walter Benjamin Fellowship 444933586 to L.G.S. and AHA Career Development Award 855170 to Q.Z.

Author contributions

Q.Z. and P.E.S. conceptualized the study and designed experiments. Q.Z., S.C., J.-B.F., L.G.S., Q.L., S.Z., C.J., Z.Z., D.K., N.L., C.M.G., C.L., R.G., A.C.-S. and C.M.K. conducted experiments. N.H., L.P. and C.M.K. were involved in study design and data flow in the paper. All authors analysed and interpreted data. Q.Z. wrote the manuscript and C.M.K. and P.E.S. revised it.

Competing interests

The authors declare no competing interests.

Additional information

Extended data is available for this paper at https://doi.org/10.1038/s42255-024-01078-9.

Supplementary information The online version contains supplementary material available at https://doi.org/10.1038/s42255-024-01078-9.

Correspondence and requests for materials should be addressed to Philipp E. Scherer.

Peer review information *Nature Metabolism* thanks the anonymous reviewer(s) for their contribution to the peer review of this work. Primary Handling Editor: Revati Dewal, in collaboration with the *Nature Metabolism* team.

https://doi.org/10.1038/s42255-024-01078-9

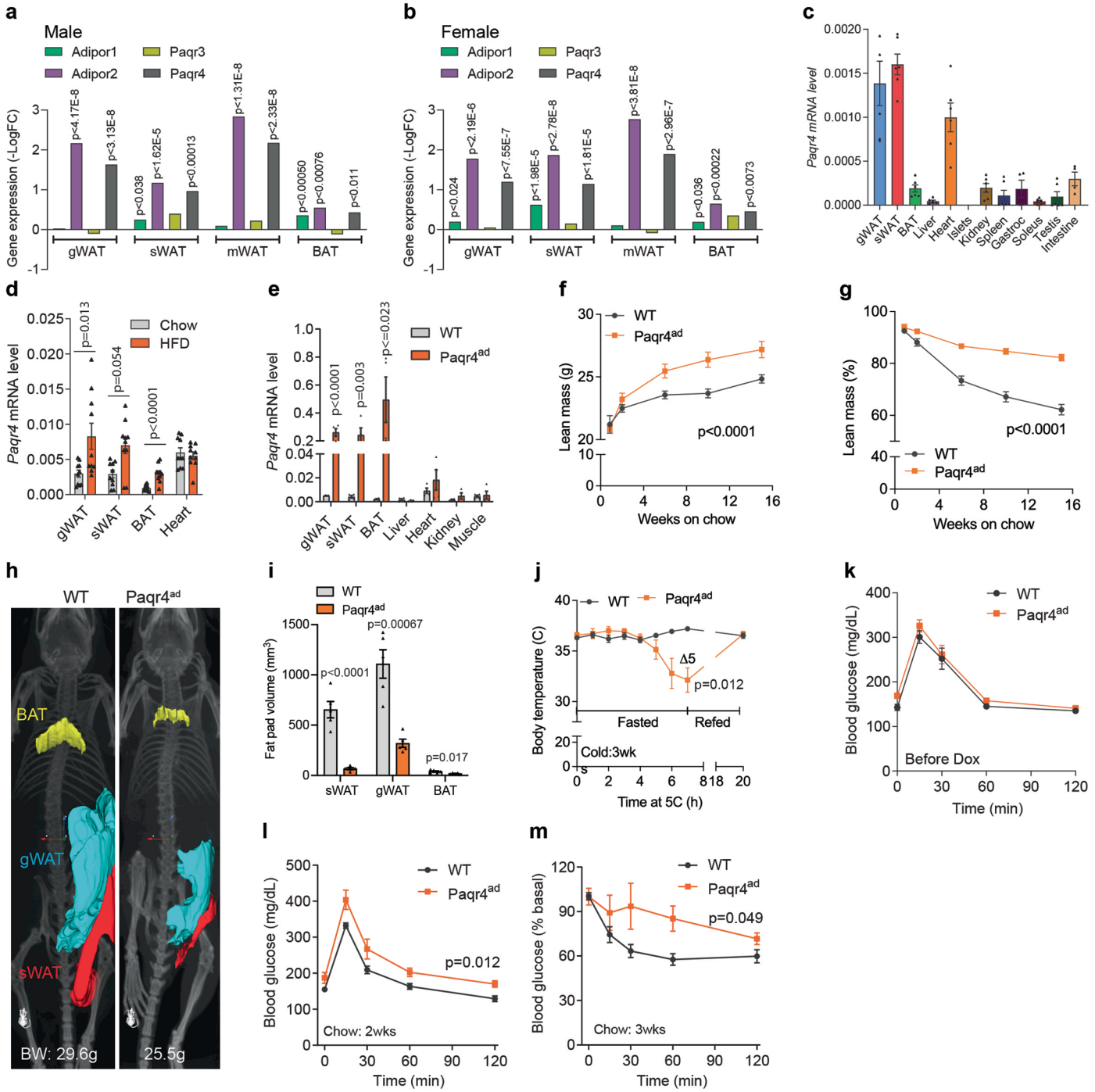

Extended Data Fig. 1 | PAQR4 is an important player in regulating adipose tissue function. Gene expression of Class I Paqr's in less expanded adipose tissues (AT), including gonadal (gWAT), subcutaneous (sWAT), mesenteric white adipose tissues (mWAT), and brown fat (BAT) from obese mice, compared to massively expanded AT from morbidly obese mice, in males (**a**) and females (**b**) (n = 3). -Log2 (FC) and *P*-values are shown. FC, fold change. (**c**) Tissue expression of *Paqr4* in chow-fed mice (n = 6). (**d**) HFD feeding increases *Paqr4* expression in adipose tissues but not heart (n = 10). (**e**) *Paqr4* is specifically induced in adipose tissues in Paqr4^{ad} mice fed dox chow for 1 week (n = 4). (**f**-**g**) Time course of lean mass and percentage of lean mass (WT, n = 8; Paqr4^{ad}, n = 10). (**h**-**i**) CT scan of WT and Paqr4^{ad} mice. ROI of gWAT, sWAT and BAT were highlighted, and the fat pad volume was measured (n = 5). (**j**) Cold-acclimated Paqr4^{ad} mice display hypothermia upon fasting (WT, n = 7; Paqr4^{ad}, n = 6). (**k**) Overlapping glucose tolerance test prior to dox induction (WT, n = 7; Paqr4^{ad}, n = 6). (**l**-**m**) Impaired glucose tolerance and insulin sensitivity in Paqr4^{ad} mice (WT, n = 7; Paqr4^{ad}, n = 6). Data shown as mean ± SEM and analysed by two-tailed unpaired *t*-test (**d**-**e**, **i**) and two-way ANOVA (**f**-**g**, **j**-**m**).

https://doi.org/10.1038/s42255-024-01078-9

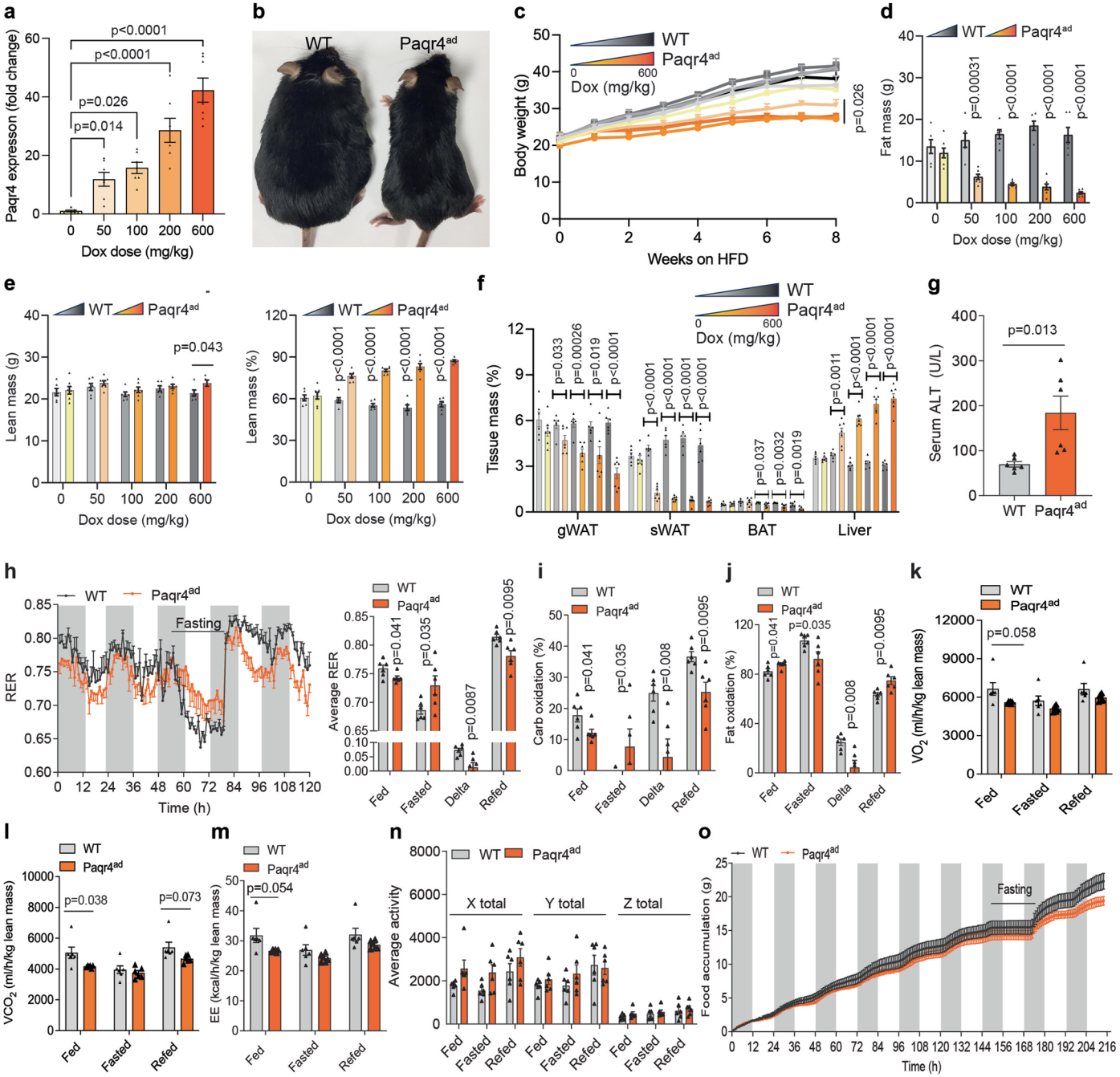

Extended Data Fig. 2 | Paqr4 overexpressing in adipocytes reduced weight gain upon HFD feeding. Mice were fed dox-HFD (600 mg/kg except in the dox-response assays). (**a**) Dox-dose dependent of *Paqr4* induction in gonadal fat pads in Paqr4^{ad} mice (WT, n = 6; Paqr4^{ad}, n = 7). (**b**) Paqr4^{ad} mice are smaller. (**c**-**f**) Body weight, fat mass, lean mass, percentage of lean mass and tissue mass of WT and Paqr4^{ad} mice in response to different dox doses (WT, n = 6; Paqr4^{ad}, n = 7). (**g**) Elevated serum ALT levels in Paqr4^{ad} mice at week 10 (n = 6). (**h**) Respiratory exchange ratio (RER) assessed in mice fed dox-HFD for 2 weeks (n = 6). (**i**-**j**) Substrate oxidation calculated from RER and VO_2 (n = 6). (**k**-**o**) VO_2, VCO_2, energy expenditure (EE), physical activity and food intake assessed in mice fed dox-HFD for 2 weeks (n = 6). Data shown as mean ± SEM and analysed by one-way ANOVA followed by Holm-Sidak multiple-comparison test (**a**), two-way ANOVA (**c**), and two-tailed unpaired *t*-test (**d**-**g**, **h**-**n**).

https://doi.org/10.1038/s42255-024-01078-9

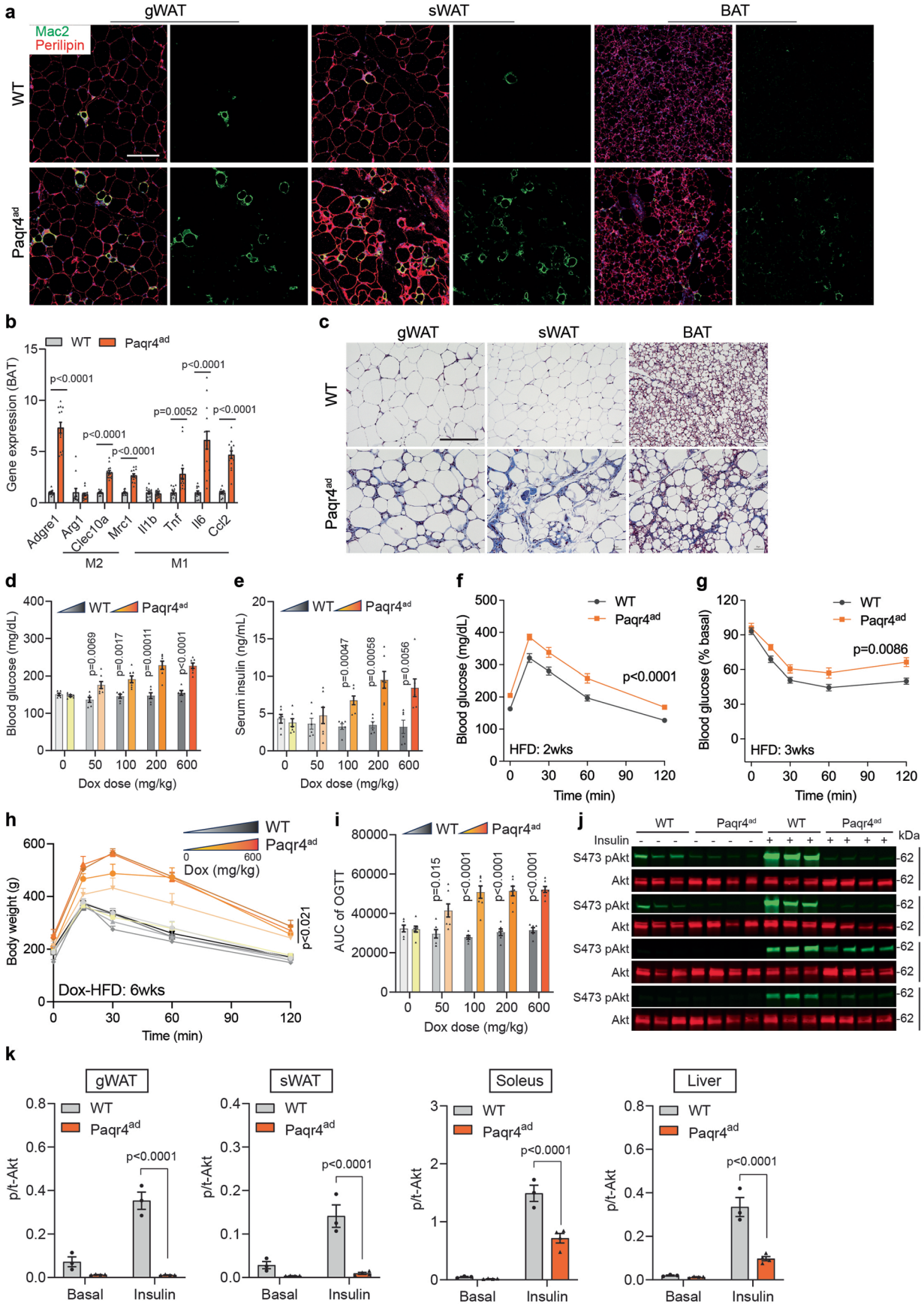

Extended Data Fig. 3 | See next page for caption.

https://doi.org/10.1038/s42255-024-01078-9

Extended Data Fig. 3 | Paqr4 overexpressing in adipocytes induces insulin resistance upon HFD feeding. (**a**) Immunofluorescence staining of Perilipin (red) and Mac2 (macrophage marker, green) in different fat pads (n = 3). Scale bar 200 μm. (**b**) Inflammatory gene expressions in BAT at week 3 (WT, n = 12; Paqr4^{ad}, n = 14). (**c**) Trichrome staining indicated enhanced adipose fibrosis in Paqr4^{ad} mice at week 10 (n = 3). Scale bar 200 μm. (**d**-**e**) Dox-dose dependent effects of hyperglycaemia and hyperinsulinaemia in Paqr4^{ad} mice (WT, n = 6; Paqr4^{ad}, n = 7). (**f**-**g**) Impaired glucose tolerance and insulin^{-}stimulated glucose disposal in Paqr4^{ad} mice at week 2-3 (WT, n = 14; Paqr4^{ad}, n = 12). (**h**-**i**) Dox-dose dependent effects of glucose tolerance in Paqr4^{ad} mice (WT, n = 6; Paqr4^{ad}, n = 7). (**j**-**k**) Impaired insulin signalling as accessed by phospho-Akt (Ser473) in various tissues from Paqr4^{ad} mice fed dox-HFD for 6 weeks (WT, n = 3; Paqr4^{ad}, n = 4). Data shown as mean ± SEM and analysed by two-tailed unpaired *t*-test (**b**, **d**-**e**, **i**) and two-way ANOVA followed by Holm-Sidak multiple-comparison test (**f**-**h**, **k**).

https://doi.org/10.1038/s42255-024-01078-9

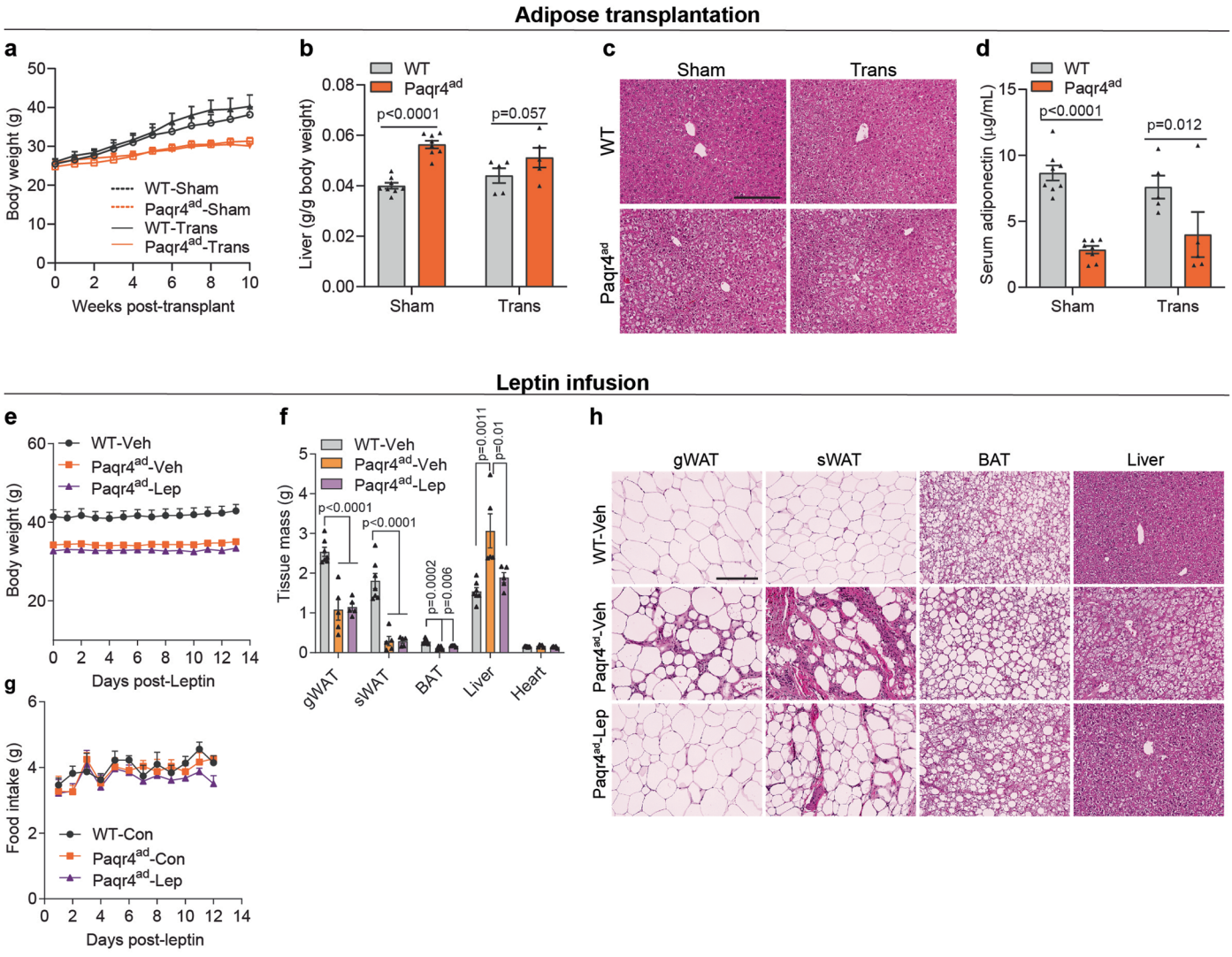

Extended Data Fig. 4 | Amelioration of PAQR4-induced metabolic defects by adipose transplants or leptin treatment. Mice receiving adipose transplants (sWAT) were fed dox chow for 10 weeks. (**a**-**b**) Transplants do not rescue body weight and liver/body weight ratio (Sham, n = 8 per group; Transplant, n = 5 per group). (**c**) H&E staining of liver (n = 3). Scale bar 200 μm. (**d**) Transplants do not rescue serum adiponectin levels (Sham, n = 8 per group; Transplant, n = 5 per group). (**e**-**f**) Two weeks of leptin perfusion does not rescue body weight and adipose tissue mass, but reduces liver weight in Paqr4^{ad} mice (WT, n = 7; Paqr4^{ad}, n = 5 per group). (**g**) Unaltered food intake (WT, n = 7; Paqr4^{ad}, n = 5 per group). (**h**) Leptin improves adipose health and fatty liver in *Paqr4^{ad}* mice (WT, n = 3; Paqr4^{ad}, n = 4 per group). Scale bar 200 μm. (**i**) Reduced body weight in *ob/ob*:Paqr4^{ad} mice (*ob/ob*, n = 8; *ob/ob*:Paqr4^{ad}, n = 4; *Ob/ob* and Paqr4^{ad}, n = 5). (**j**) Food intake is reduced transiently upon dox induction and recovered thereafter (*ob/ob*, n = 8; *ob/ob*:Paqr4^{ad}, n = 4; *Ob/ob* and Paqr4^{ad}, n = 5). (**k**) Further aggravated glucose intolerance in *ob/ob*:Paqr4^{ad} mice (*ob/ob*, n = 8; *ob/ob*:Paqr4^{ad}, n = 4; *Ob/ob* and Paqr4^{ad}, n = 5). (**l**) Insulin release during glucose tolerance test (*ob/ob*, n = 8; *ob/ob*:Paqr4^{ad}, n = 4; *Ob/ob* and Paqr4^{ad}, n = 5). Data shown as mean ± SEM and analysed by two-way ANOVA (**a-b, d-e, g, i-l**) and one-way ANOVA followed by Holm-Sidak multiple-comparison test (**f**).

https://doi.org/10.1038/s42255-024-01078-9

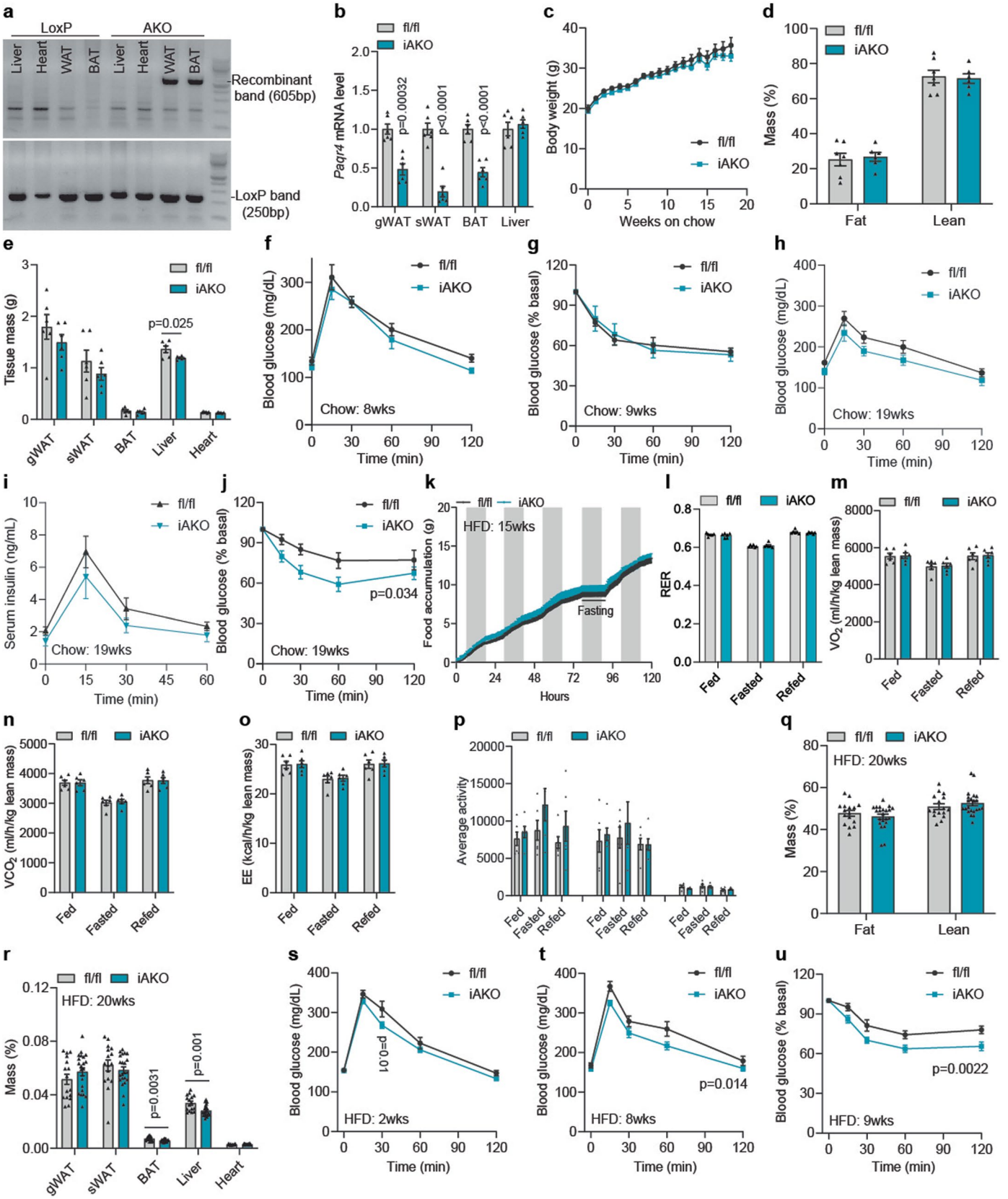

Extended Data Fig. 5 | See next page for caption.

https://doi.org/10.1038/s42255-024-01078-9

Extended Data Fig. 5 | Adipocyte-specific deletion of Paqr4 improves glucose homoeostasis in obesity. (**a**-**b**) Specific recombination of *Paqr4* (representative images from 3 independent assays with similar results) and downregulation in gene expression levels in Paqr4^{iAKO} mice fed dox chow for 2 weeks (n = 6). (**c**-**d**) Comparable body weight and body composition in Paqr4^{iAKO} mice fed dox chow for 20 weeks (Paqr4$^{fl/fl}$, n = 7; Paqr4^{iAKO}, n = 6). (**e**) Tissue weights in Paqr4^{iAKO} mice fed dox chow for 20 weeks (n = 6). (**f**-**g**) Comparable glucose tolerance and insulin sensitivity after 8-9 weeks of dox chow feeding (Paqr4$^{fl/fl}$, n = 7; Paqr4^{iAKO}, n = 6). (**h**-**j**) Moderately improved glucose tolerance and insulin-mediated glucose disposal after 19-20 weeks of dox chow feeding (Paqr4$^{fl/fl}$, n = 7; Paqr4^{iAKO}, n = 6). (**k**-**p**) Comparable food intake, RER, VO_2, VCO_2, energy expenditure (EE), and physical activity after 15 weeks of dox-HFD feeding (n = 6). (**q**-**r**) Body composition and tissue weights after 20 weeks of dox-HFD feeding (Paqr4$^{fl/fl}$, n = 16; Paqr4^{iAKO}, n = 22). (**s**-**u**) Slightly improved glucose tolerance in Paqr4^{iAKO} mice after 2 and 8 weeks and insulin-mediated glucose disposal after 9 weeks of dox-HFD feeding (Paqr4$^{fl/fl}$, n = 16; Paqr4^{iAKO}, n = 22). Data shown as mean ± SEM and analysed by two-tailed unpaired *t*-test (**b**, **d**-**e**, **l**-**r**) and two-way ANOVA (**c**, **f**-**k**, **s**-**u**).

https://doi.org/10.1038/s42255-024-01078-9

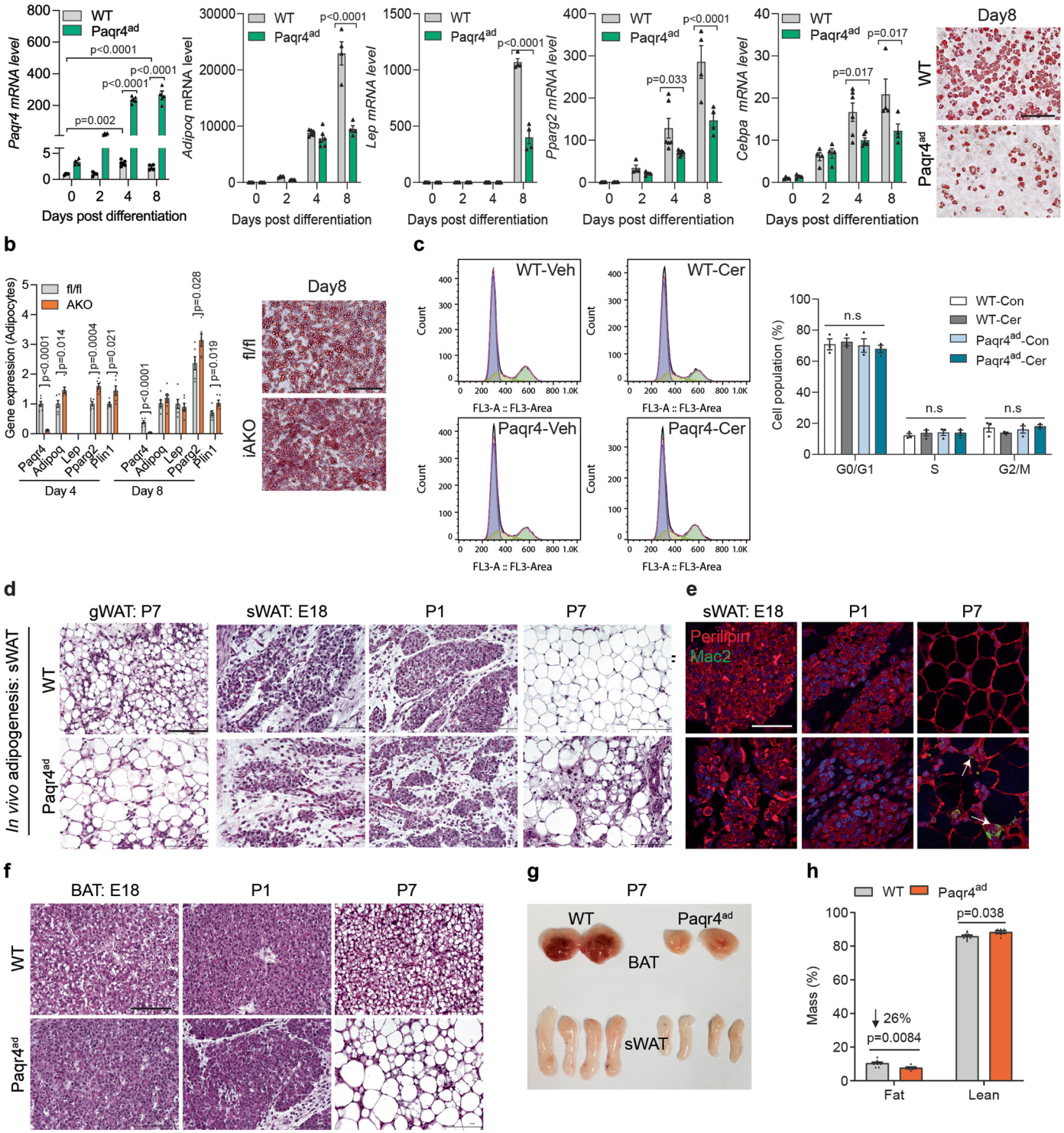

Extended Data Fig. 6 | PAQR4 suppresses adipogenesis. (**a**) PAQR4 decreases adipocyte marker expressions during adipogenesis (Group day 4, n = 6; other groups, n = 4) and reduces lipid accumulation as assessed by Oil Red O staining (n = 3) in stromal vascular fraction (SVF) cells. Scale bar 200 µm. (**b**) Expression of adipocyte markers (n = 6) and Oil Red O staining (n = 3) during adipogenesis upon *Paqr4* deletion. Scale bar 200 µm. (**c**) Minor changes of cell cycle by PAQR4 and C2-ceramide at day 2 of adipogenesis (n = 3 biological samples). (**d**) H&E staining in gWAT and sWAT during adipose development of mice fed dox chow from E13 onwards (n = 4 mice per group). E18, embryotic day 18; P1 and P7, postnatal day 1 and 7. Scale bar 100 µm. (**e**) Immunofluorescence staining of Perilipin (red) and Mac2 (green) in sWAT during adipose development of mice fed dox chow from E13 onwards (n = 4). Scale bar 50 µm. (**f**) H&E staining in BAT during adipose development of mice fed dox chow from E13 onwards (n = 4). Scale bar 100 µm. (**g**) Smaller size of BAT and sWAT on P7 in Paqr4^{ad} mice fed dox chow from E13 onwards. (**h**) Body composition at week 6 in mice fed dox chow from E13 onwards (WT, n = 9; Paqr4^{ad}, n = 6). Data shown as mean ± SEM and analysed by two-way ANOVA (**a**), one-way ANOVA followed by Holm-Sidak multiple-comparison test (**c**), and two-tailed unpaired *t*-test (**b**, **h**).

https://doi.org/10.1038/s42255-024-01078-9

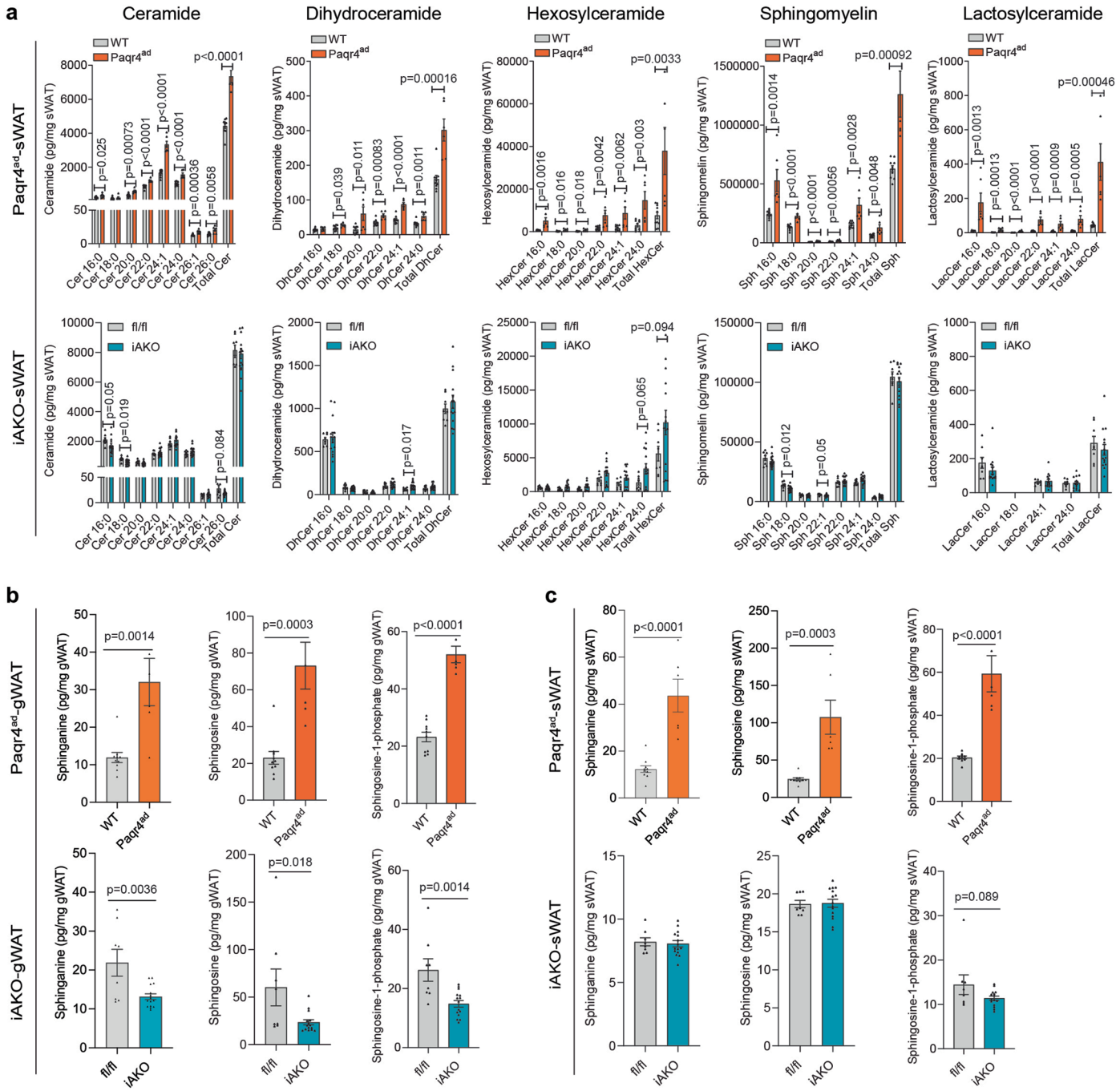

Extended Data Fig. 7 | Effects of PAQR4 on sphingolipid levels in adipose tissues. (**a**-**c**) Sphingolipid profiles in sWAT and gWAT of Paqr4^{ad} mice (WT, n = 10; Paqr4^{ad}, n = 6) or Paqr4^{iAKO} mice (Paqr4$^{fl/fl}$, n = 8; Paqr4^{iAKO}, n = 15) fed dox-HFD. Data shown as mean ± SEM and analysed by two-tailed unpaired *t*-test (**a**-**c**).

https://doi.org/10.1038/s42255-024-01078-9

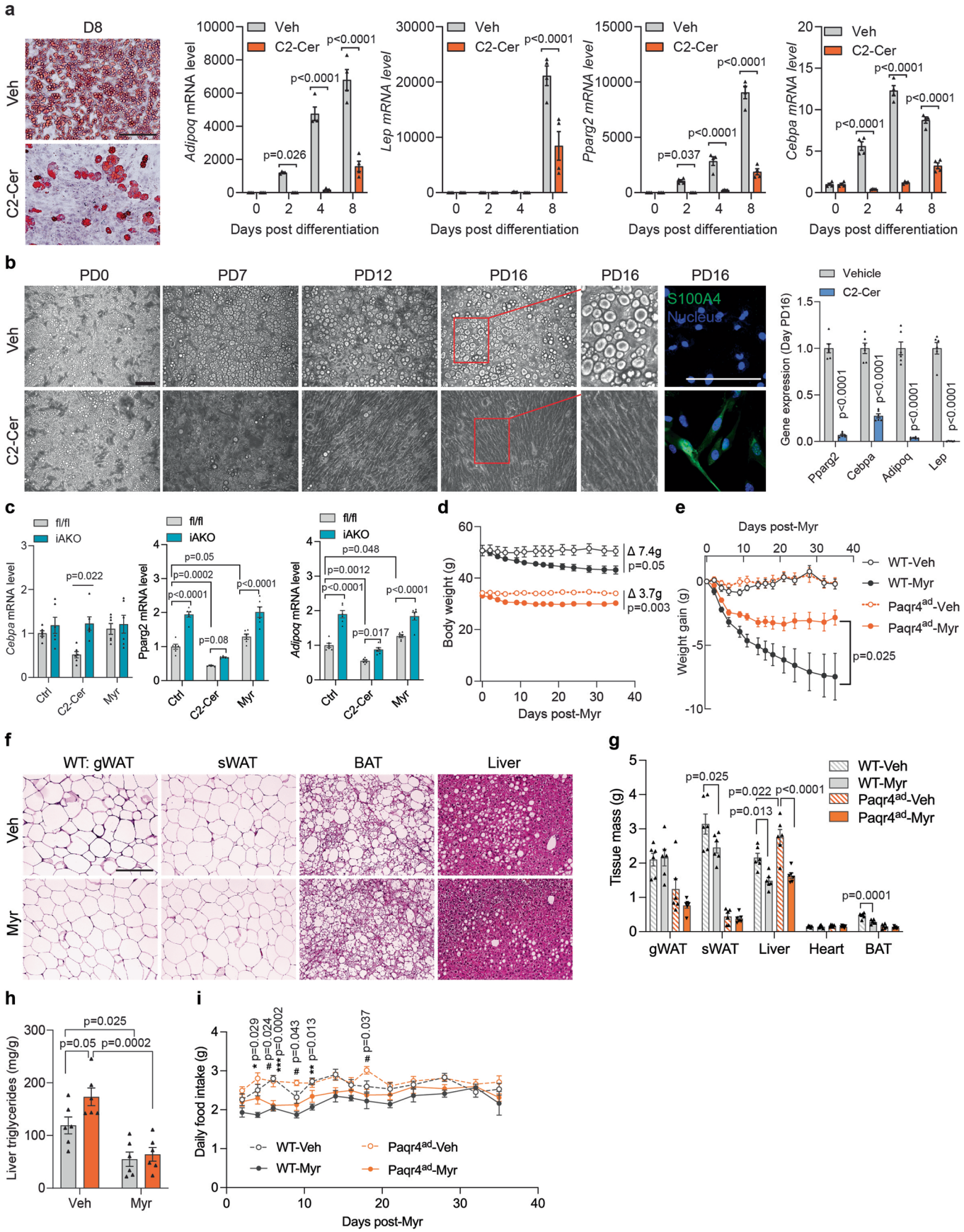

Extended Data Fig. 8 | See next page for caption.

https://doi.org/10.1038/s42255-024-01078-9

Extended Data Fig. 8 | Blocking ceramide synthesis improves PAQR4-induced metabolic defects. (**a**) Oil Red O staining (n = 3) and adipocyte markers (n = 4 biological samples) indicate that C2-Ceramide (C2-Cer) blocks adipogenesis in sWAT stromal vascular fraction (SVF) cells. Scale bar 200 µm. (**b**) C2-Cer causes de-differentiation of adipocytes with expression of fibroblast marker S100A4 and decreased expression of adipocyte markers (n = 6 biological samples). Adipocytes were treated with C2-Cer post-differentiation (PD) for the indicated days. Scale bar 100 µm. (**c**) Expression of adipogenic markers in SVF cells that were differentiated in the absence or presence of 5 µM C2-Cer or 10 µM myriocin (Myr) at day 4 of post-differentiation (n = 6 biological samples). (**d**-**e**) Body weight and weight gain upon Myr treatment in mice priorly fed dox-HFD for 12 weeks (n = 6). (**f**) H&E staining of adipose tissues and liver after 5 weeks of Myr treatment (WT, n = 3; Myr, n = 4). Scale bar 200 µm. (**g**) Tissue weights after 5 weeks of Myr treatment (n = 6). (**h**) Myr treatment reduced liver triglyceride content in Paqr4^{ad} mice (n = 6). (**i**) Food intake upon Myr treatment in mice priorly fed dox-HFD for 12 weeks (n = 6). * indicates comparisons between groups of WT-Veh and WT-Myr; $^{\#}$ indicates comparisons between groups of Paqr4^{ad}-Veh and Paqr4^{ad}-Myr. Data shown as mean ± SEM and analysed by two-way ANOVA followed by Holm-Sidak multiple-comparison test (**a**, **c**-**e**, **g**-**i**) and two-tailed unpaired *t*-test (**b**).

https://doi.org/10.1038/s42255-024-01078-9

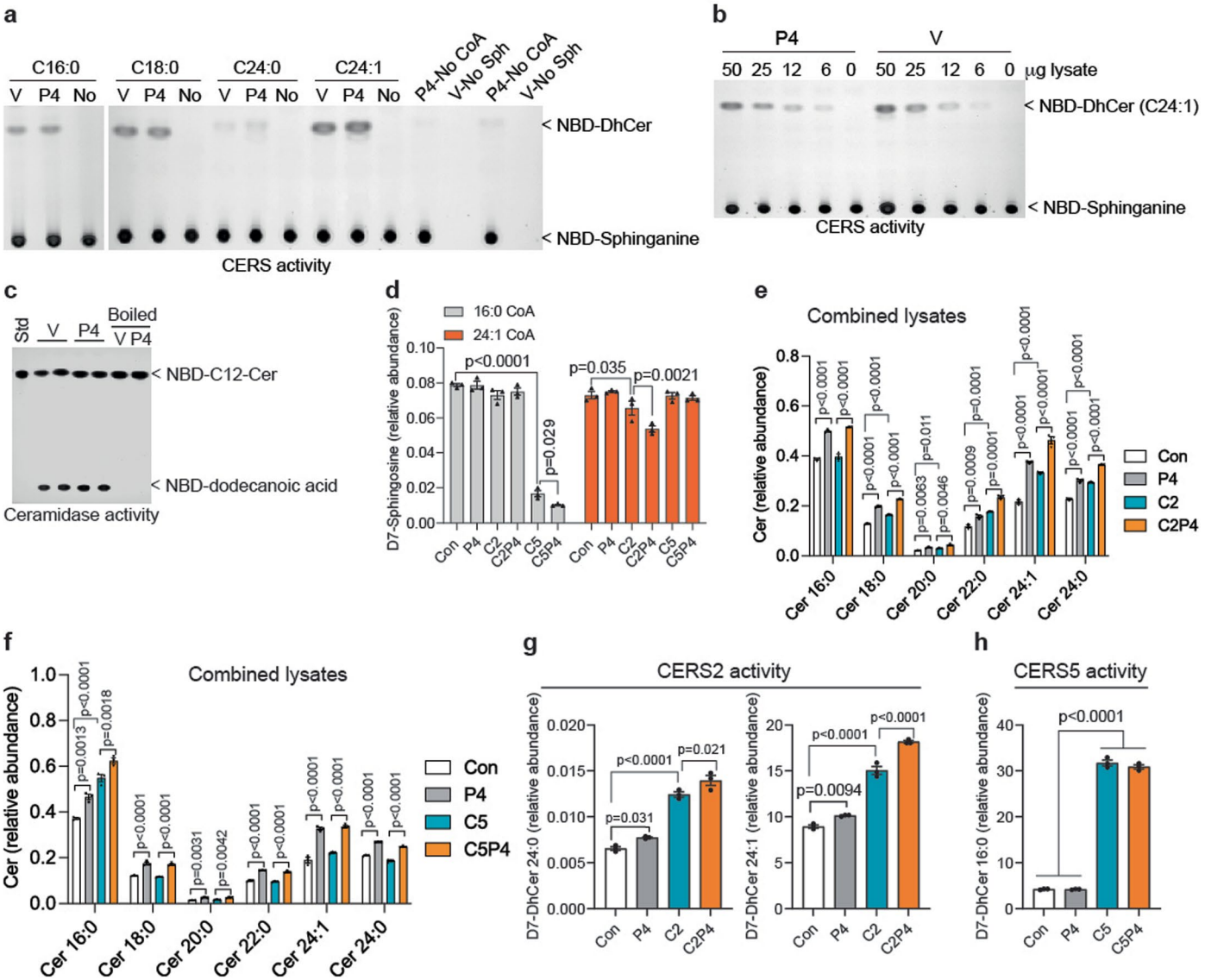

Extended Data Fig. 9 | PAQR4 regulates ceramide synthase activity. (**a**-**c**) Fluorescent activity assays indicate PAQR4 itself does not have ceramide synthase or ceramidase activity. Representative images from 2 independent assays with similar results. (**d**) Consumption of D7-spingosine that originally comes from D7-sphinganine during the CERS activity assay (n = 3). (**e**-**f**) PAQR4 further increases CERS2 or CERS5-induced ceramide levels in HEK293T cells (n = 3). Ceramide species are measured in lysates of cells overexpressing Myc-Cers2 (C2), Myc-Cers5 (C5), and FLAG-Paqr4 (P4) alone or in combination of the two individual lysates (C2P4 and C5P4) as indicated. (**g**-**h**) Enzymatic activities of CERS2 and CERS5 are determined in individual cell lysates or in combination of the two individual lysates as indicated. Products of stable isotope labelled C24:1 and C16:0 D7-dehydroceramide (D7-DhCer) that are generated from the substrates D7-sphinganine and C24:1 or C16:0 acyl-CoA, which are mainly utilized by CERS2 and CERS5, respectively, reflecting their enzymatic activities (n = 3). Data shown as mean ± SEM and analysed by one-way ANOVA followed by Holm-Sidak multiple-comparison test (**d**-**h**).

https://doi.org/10.1038/s42255-024-01078-9

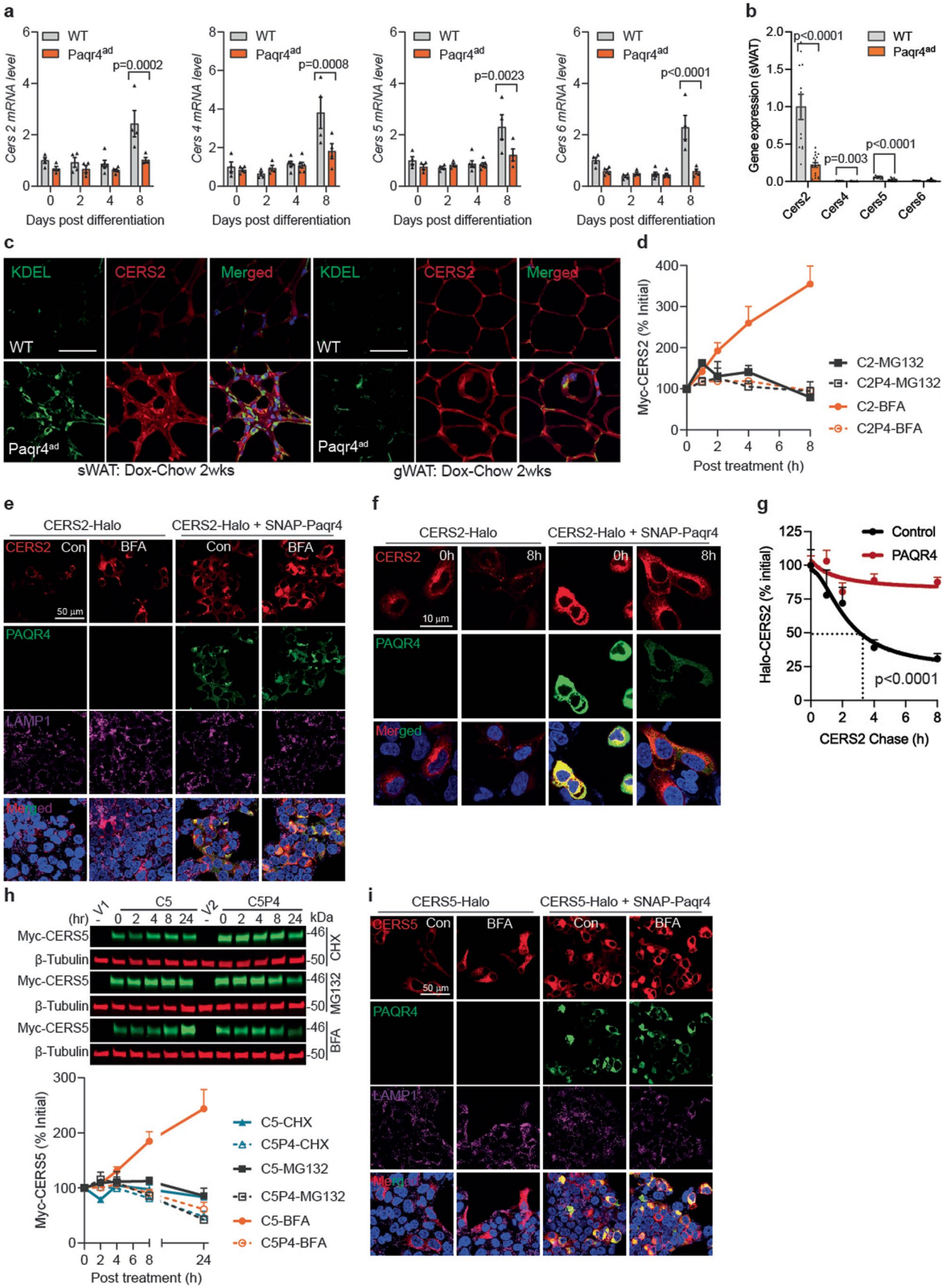

Extended Data Fig. 10 | See next page for caption.

https://doi.org/10.1038/s42255-024-01078-9

Extended Data Fig. 10 | PAQR4 promotes ceramide synthase stability. (**a**) Cers expressions during SVF-derived adipocyte differentiation (Day 4 group, n = 6; other groups, n = 4). (**b**) Cers expressions in sWAT of Paqr4ad and WT mice fed dox chow for 2 weeks (WT, n = 12; Paqr4ad, n = 18). (**c**) Representative staining of ER marker KDEL and CERS2 in sWAT and gWAT from 2 weeks of dox chow-fed Paqr4^{ad} and WT mice (n = 3). Scale bar 50 μm. (**d**) Quantification analysis of Myc-CERS2 (C2, normalized by β-Tubulin) during the treatment of MG132 or bafilomycin A1 (BFA) (n = 3). (**e**) PAQR4 prevents CERS2 lysosomal degradation. HEK293A cells were transfected with Halo-Cers2 and SNAP-Paqr4 vectors for 24 h, and then treated with BFA for 8 h. CERS2 was labelled with HaloTag TMR ligand (red) and PAQR4 was labelled with SNAP-Cell Oregon Green (green). Cells were then fixed and stained with lysosomal marker LAMP1. Scale bar, 50 μm. Representative images from 2 independent assays with similar results. (**f**-**g**) 'Pulse–chase' indicates PAQR4 stabilization of CERS2. CERS2 or PAQR4 were first labelled with HaloTag TMR ligand (red) or SNAP-Cell Oregon Green (green), respectively, cells were then imaged at the indicated time points. About 20 cells of each condition were analysed. (n = 3 biological samples for each group.) Scale bar 10 μm. (**h**) Effect of PAQR4 on CERS5 protein levels in the presence of cycloheximide (CHX), MG132, or BFA (n = 2). (**i**) PAQR4 prevents CERS5 lysosomal degradation in HEK293A cells. Cells were transfected with Halo-Cers5 and SNAP-Paqr4 vectors for 24 h, and then treated as in (**e**). Representative images from 2 independent assays with similar results. Scale bar 50 μm. Data shown as mean ± SEM and analysed by two-way ANOVA followed by Holm-Sidak multiple-comparison test (**a**, **g**) and two-tailed unpaired t-test (**b**).

nature portfolio

Corresponding author(s): Philipp Scherer

Last updated by author(s): 4/23/2024

Reporting Summary

Nature Portfolio wishes to improve the reproducibility of the work that we publish. This form provides structure for consistency and transparency in reporting. For further information on Nature Portfolio policies, see our Editorial Policies and the Editorial Policy Checklist.

Statistics

For all statistical analyses, confirm that the following items are present in the figure legend, table legend, main text, or Methods section.

n/a	Confirmed	
☐	☒	The exact sample size (*n*) for each experimental group/condition, given as a discrete number and unit of measurement
☐	☒	A statement on whether measurements were taken from distinct samples or whether the same sample was measured repeatedly
☐	☒	The statistical test(s) used AND whether they are one- or two-sided *Only common tests should be described solely by name; describe more complex techniques in the Methods section.*
☐	☒	A description of all covariates tested
☐	☒	A description of any assumptions or corrections, such as tests of normality and adjustment for multiple comparisons
☐	☒	A full description of the statistical parameters including central tendency (e.g. means) or other basic estimates (e.g. regression coefficient) AND variation (e.g. standard deviation) or associated estimates of uncertainty (e.g. confidence intervals)
☐	☒	For null hypothesis testing, the test statistic (e.g. *F*, *t*, *r*) with confidence intervals, effect sizes, degrees of freedom and *P* value noted *Give P values as exact values whenever suitable.*
☒	☐	For Bayesian analysis, information on the choice of priors and Markov chain Monte Carlo settings
☒	☐	For hierarchical and complex designs, identification of the appropriate level for tests and full reporting of outcomes
☐	☒	Estimates of effect sizes (e.g. Cohen's *d*, Pearson's *r*), indicating how they were calculated

Our web collection on statistics for biologists contains articles on many of the points above.

Software and code

Policy information about availability of computer code

Data collection	Spingolipids data acquisition: Nexera ultra-high-performance liquid chromatograph coupled to an LCMS-8050 Glycerolipids data: Nexera LC-40 UHPLC system coupled to a Shimadzu LCMS-9030 Q-TOF mass spectrometer Cell sorting: BD Biosciences FACSAria cytometer Flow cytometry analysis: BD Biosciences LSR II cytometer Image acquisition: Olympus FSX100 Microscope , LSM510 confocal microscope (Zeiss) Mice CT imaging: Mediso NanoScan Sc-transcriptomics: 10X Genomics Chromium software, Illumina NovaSeq 6000 system qPCR acquisition: QuantStudio 5 and 6 Flex Real-Time PCR System software
Data analysis	Glycerolipids data analysis: The LIPID MAPS® Lipidomics Gateway (https://www.lipidmaps.org/) FACS data analysis: FlowJo (V10.8.1) Image processing and quantification: Fiji (ImageJ 1.53c), VivoQuant workstation (Invicro). Sc-RNA-seq: Cell Ranger (v7.0.0), Seurat R package (v4.1.1; Satija Lab, Seurat; https://satijalab.org/seurat/), RStudio (v2023.06.2+561) GO enrichment analysis: DAVID 2021 (https:// david.ncifcrf.gov/) Proteomics: Perseus software platform (v2.0.11) (https://maxquant.net/perseus/) Statistics: GraphPad Prism 8.0

For manuscripts utilizing custom algorithms or software that are central to the research but not yet described in published literature, software must be made available to editors and reviewers. We strongly encourage code deposition in a community repository (e.g. GitHub). See the Nature Portfolio guidelines for submitting code & software for further information.

Data

Policy information about availability of data

All manuscripts must include a data availability statement. This statement should provide the following information, where applicable:

- Accession codes, unique identifiers, or web links for publicly available datasets
- A description of any restrictions on data availability
- For clinical datasets or third party data, please ensure that the statement adheres to our policy

scRNA-seq data files are deposited in Gene Expression Omnibus (GSE246712).

Research involving human participants, their data, or biological material

Policy information about studies with human participants or human data. See also policy information about sex, gender (identity/presentation), and sexual orientation and race, ethnicity and racism.

Reporting on sex and gender	N/A
Reporting on race, ethnicity, or other socially relevant groupings	N/A
Population characteristics	N/A
Recruitment	N/A
Ethics oversight	N/A

Note that full information on the approval of the study protocol must also be provided in the manuscript.

Field-specific reporting

Please select the one below that is the best fit for your research. If you are not sure, read the appropriate sections before making your selection.

☒ Life sciences ☐ Behavioural & social sciences ☐ Ecological, evolutionary & environmental sciences

For a reference copy of the document with all sections, see nature.com/documents/nr-reporting-summary-flat.pdf

Life sciences study design

All studies must disclose on these points even when the disclosure is negative.

Sample size	Sample sizes were determined based on previous published papers containing similar procedures and pilot data showing trends of effects. All the sample size information is indicated in the figure legends.
Data exclusions	Mice in the transgenic cohorts who occasionally have malocclusion were excluded from studies as this affects their nutritional status. Two sample in the lipidomics analysis of sWAT was not included due to sample loss.
Replication	Each experiment was independently reproduced >=2 times. Additional details were provided in corresponding figure legends.
Randomization	Mice were first grouped based on genotypes, and subsequently randomized into groups for different treatments.
Blinding	Studies were not performed blinded as mouse genotypes were predetermined. We keep an unbiased way to collect and analyze data with all randomized assays.

Reporting for specific materials, systems and methods

We require information from authors about some types of materials, experimental systems and methods used in many studies. Here, indicate whether each material, system or method listed is relevant to your study. If you are not sure if a list item applies to your research, read the appropriate section before selecting a response.

Materials & experimental systems

n/a	Involved in the study
☐	☒ Antibodies
☐	☒ Eukaryotic cell lines
☒	☐ Palaeontology and archaeology
☐	☒ Animals and other organisms
☒	☐ Clinical data
☒	☐ Dual use research of concern
☒	☐ Plants

Methods

n/a	Involved in the study
☒	☐ ChIP-seq
☐	☒ Flow cytometry
☒	☐ MRI-based neuroimaging

Antibodies

Antibodies used

Primary antibodies:
Antibody, Application, Supplier, Cat#, Clone, Lot#
anti-CD31-BV421, FACS, BioLegend, cat# 102423, 390, B347936
anti-CD45-BV421, FACS, BioLegend, cat# 103133, 30-F11
anti-PDGFRb/CD140b-APC, FACS, BioLegend, cat# 136007, APB5, B365704
anti-CD31-PE/Cy7, FACS, BioLegend, cat# 102418, 390, B398639
anti-CD45-PE/Cy7, FACS, BioLegend, cat# 103114, 30-F11, B382493
anti-TER119-PE/Cy7, FACS, BioLegend, cat# 116222, TER19, B374823
anti-CD26/DPP4-FITC, FACS, BioLegend, cat# 137806, H194-112, B383392
anti-CD54/ICAM1-PE, FACS, BioLegend, cat# 116108, YN1/1.7.4, B393840
anti-SCA1/LY6a-BV711, FACS, BioLegend, cat# 108131, D7, B389732
anti-CD142/F3, FACS, SinoBiological, cat# 50413-R034, 034, HA13AU2301
anti-Adiponectin, Western blotting, homemade
anti-phospho-Akt (Ser473) (D9E), Western blotting, Cell Signaling, cat# 4060
anti-Akt (pan) (40D4), Western blotting, Cell Signaling, cat# 2920
anti-Myc-tag, Western blotting, Cell Signaling, cat# 2278
anti-FLAG-tag, Western blotting, Cell Signaling, cat# 14793
anti-CERS2, Western blotting, Sigma, cat# HPA027262
anti-beta-tubulin, Western blotting, Cell Signaling, cat# 86298
anti-Ceramide IgM, Immunoprecipitation, Enzo Life Sciences, cat# ALX-804-196-T050, 15B4
anti-LAMP1, Immunostaining, Cell Signaling, cat# 9091
anti-Perilipin, Immunostaining, Fitzgerald, cat# 20R-PP004
anti-EGFP, Immunostaining, Abcam, cat# ab13970
anti-Mac2, Immunostaining, CEDARLANE, cat# CL8942AP
anti-S100A4, Immunostaining, Abcam, cat# ab41532
anti-KDEL, Immunostaining, Abcam, cat# ab176333
anti-LASS2/CERS2, Immunostaining, Santa Cruz, cat# sc-390745
anti-Insulin, Immunostaining, Dako, cat# A0564
anti-Glucagon, Immunostaining, Abcam, cat# ab92517
Goat anti-Guinea Pig IgG (H+L) Alexa Fluor™ 488, Immunostaining, Invitrogen, cat# A-11073, 2674373
Donkey anti-Rabbit IgG (H+L) Alexa Fluor™ 594, Immunostaining, Invitrogen, cat# A-21207, 2441375
Goat anti-Chicken IgY (H+L) Alexa Fluor™ 488, Immunostaining, Invitrogen, cat# A11039, 1691381
Goat anti-Guinea Pig IgG (H+L) Alexa Fluor™ 594, Immunostaining, Invitrogen, cat# A11076, 2304271
Donkey anti-Rat IgG (H+L) Alexa Fluor™ 488, Immunostaining, Invitrogen, cat# A21208, 1229697
Goat anti-Rabbit IgG (H+L) Alexa Fluor™ Plus 488, Immunostaining, Invitrogen, cat# A32731, XF346494
Chicken anti-Mouse IgG (H+L) Alexa Fluor™ 594, Immunostaining, Invitrogen, cat# A21201, 2136793
IRDye® 800CW Goat anti-Rabbit IgG Secondary Antibody, Western blotting, LI-COR, cat# 926-32211, B80807-01
IRDye® 680RD Donkey anti-Mouse IgG Secondary Antibody, Western blotting, LI-COR, cat# 926-68072, C90723-07
IRDye® 800CW Goat anti-Mouse IgG Secondary Antibody, Western blotting, LI-COR, cat# 926-32210, C90408-08
IRDye® 680RD Goat anti-Rabbit IgG Secondary Antibody, Western blotting, LI-COR, cat# 926-68071, C90827-25

Validation

All primary antibodies are commercially available and validated by the manufacturer, except anti-Adiponectin that is homemade.
CD31-BV421 was validated for flow cytometry. (https://www.biolegend.com/en-us/products/brilliant-violet-421-anti-mouse-cd31-antibody-8599)
CD45-BV421 was validated for flow cytometry. (https://www.biolegend.com/en-us/products/brilliant-violet-421-anti-mouse-cd45-antibody-7253)
PDGFRb/CD140b-APC was validated for flow cytometry. (https://www.biolegend.com/en-us/products/apc-anti-mouse-cd140b-antibody-6441)
CD31-PE/Cy7 was validated for flow cytometry. (https://www.biolegend.com/en-us/products/pe-cyanine7-anti-mouse-cd31-antibody-3942)
CD45-PE/Cy7 was validated for flow cytometry. (https://www.biolegend.com/en-us/products/pe-cyanine7-anti-mouse-cd45-antibody-1903)
TER119-PE/Cy7 was validated for flow cytometry. (https://www.biolegend.com/en-us/products/pe-cyanine7-anti-mouse-ter-119-erythroid-cells-antibody-3904)
CD26/DPP4-FITC was validated for flow cytometry. (https://www.biolegend.com/en-us/products/fitc-anti-mouse-cd26-dpp-4-antibody-6946)
CD54/ICAM1-PE was validated for flow cytometry. (https://www.biolegend.com/en-us/products/pe-anti-mouse-cd54-antibody-1680)
SCA1/LY6a-BV711 was validated for flow cytometry. (https://www.biolegend.com/en-us/products/brilliant-violet-711-anti-mouse-

ly-6a-e-sca-1-antibody-8632)
CD142/F3 was validated for flow cytometry. (https://pubmed.ncbi.nlm.nih.gov/31023895/)
Adiponectin was validated for Western blotting. (https://pubmed.ncbi.nlm.nih.gov/32408016/)
phospho-Akt (Ser473) was validated for Western blotting and immunostaining. (https://www.cellsignal.com/products/primary-antibodies/phospho-akt-ser473-d9e-xp-rabbit-mab/4060)
Akt (pan) was validated for Western blotting and immunostaining. (https://www.cellsignal.com/products/primary-antibodies/akt-pan-40d4-mouse-mab/2920)
Myc-tag was validated for Western blotting and immunostaining. (https://www.cellsignal.com/products/primary-antibodies/myc-tag-71d10-rabbit-mab/2278)
FLAG-tag was validated for Western blotting and immunostaining. (https://www.cellsignal.com/products/primary-antibodies/dykddddk-tag-d6w5b-rabbit-mab-binds-to-same-epitope-as-sigma-aldrich-anti-flag-m2-antibody/14793)
CERS2 was validated for Western blotting and immunostaining. (https://www.sigmaaldrich.com/US/en/product/sigma/hpa027262)
Beta-tubulin was validated for Western blotting and immunostaining. (https://www.cellsignal.com/products/primary-antibodies/b-tubulin-d3u1w-mouse-mab/86298)
Ceramide IgM was validated for immunostaining. Enzo Life Sciences, cat# ALX-804-196-T050 (https://www.enzolifesciences.com/ALX-804-196/ceramide-monoclonal-antibody-mid-15b4/)
LAMP1 was validated for Western blotting and immunostaining. (https://www.cellsignal.com/products/primary-antibodies/lamp1-d2d11-xp-rabbit-mab/9091)
Perilipin was validated for immunostaining. (https://pubmed.ncbi.nlm.nih.gov/36103820/)
EGFP was validated for immunostaining. (https://pubmed.ncbi.nlm.nih.gov/36103820/)
Mac2 was validated for immunostaining. (https://www.nature.com/articles/nm.3487)
S100A4 was validated for Western blotting and immunostaining. (https://pubmed.ncbi.nlm.nih.gov/29910813/; https://pubmed.ncbi.nlm.nih.gov/31775048/)
KDEL was validated for Western blotting and immunostaining. (https://www.abcam.com/products/primary-antibodies/kdel-antibody-epr12668-ab176333.html)
LASS2/CERS2 was validated for Western blotting and immunostaining. (https://www.scbt.com/p/lass2-antibody-c-11)
Insulin was validated for immunostaining. (https://pubmed.ncbi.nlm.nih.gov/37561596/)
Glucagon was validated for immunostaining. (https://www.abcam.com/products/primary-antibodies/glucagon-antibody-ep3070-ab92517.html)
Goat anti-Guinea Pig IgG (H+L) Alexa Fluor™ 488 was validated for immunostaining. (https://www.thermofisher.com/antibody/product/Goat-anti-Guinea-Pig-IgG-H-L-Highly-Cross-Adsorbed-Secondary-Antibody-Polyclonal/A-11073)
Donkey anti-Rabbit IgG (H+L) Alexa Fluor™ 594 was validated for immunostaining. (https://www.thermofisher.com/antibody/product/Donkey-anti-Rabbit-IgG-H-L-Highly-Cross-Adsorbed-Secondary-Antibody-Polyclonal/A-21207)
Goat anti-Chicken IgY (H+L) Alexa Fluor™ 488 was validated for immunostaining. (https://www.thermofisher.com/antibody/product/Goat-anti-Chicken-IgY-H-L-Secondary-Antibody-Polyclonal/A-11039)
Goat anti-Guinea Pig IgG (H+L) Alexa Fluor™ 594 was validated for immunostaining. (https://www.thermofisher.com/antibody/product/Goat-anti-Guinea-Pig-IgG-H-L-Highly-Cross-Adsorbed-Secondary-Antibody-Polyclonal/A-11076)
Donkey anti-Rat IgG (H+L) Alexa Fluor™ 488 was validated for immunostaining. (https://www.thermofisher.com/antibody/product/Donkey-anti-Rat-IgG-H-L-Highly-Cross-Adsorbed-Secondary-Antibody-Polyclonal/A-21208)
Goat anti-Rabbit IgG (H+L) Alexa Fluor™ Plus 488 was validated for immunostaining. (https://www.thermofisher.com/antibody/product/Goat-anti-Rabbit-IgG-H-L-Highly-Cross-Adsorbed-Secondary-Antibody-Polyclonal/A32731)
Chicken anti-Mouse IgG (H+L) Alexa Fluor™ 594 was validated for immunostaining. (https://www.thermofisher.com/antibody/product/Chicken-anti-Mouse-IgG-H-L-Cross-Adsorbed-Secondary-Antibody-Polyclonal/A-21201)
IRDye® 800CW Goat anti-Rabbit IgG Secondary Antibody was validated for Western blotting. (https://pubmed.ncbi.nlm.nih.gov/38280846/)
IRDye® 680RD Donkey anti-Mouse IgG Secondary Antibody was validated for Western blotting. (https://pubmed.ncbi.nlm.nih.gov/37558661/)
IRDye® 800CW Goat anti-Mouse IgG Secondary Antibody was validated for Western blotting. (https://pubmed.ncbi.nlm.nih.gov/37561577/)
IRDye® 680RD Goat anti-Rabbit IgG Secondary Antibody was validated for Western blotting. (https://pubmed.ncbi.nlm.nih.gov/36624187/)

Eukaryotic cell lines

Policy information about cell lines and Sex and Gender in Research

Cell line source(s)	293T cells; 293A cells; AML12.
Authentication	293T cells were obtained from ATCC (#CRL-3216), AML12 cells were obtained from ATCC (#CRL-2254), and the 293A cells were obtained from Invitrogen (#R70507).
Mycoplasma contamination	Mycoplasma was not tested.
Commonly misidentified lines (See ICLAC register)	None.

Animals and other research organisms

Policy information about studies involving animals; ARRIVE guidelines recommended for reporting animal research, and Sex and Gender in Research

Laboratory animals	All mice (TRE-Paqr4, Paqr4-flox, Adipoq-rtTA, TRE-Cre, ob/ob, Flp, and Rosa26-mT/mG) were on a C57BL/6J background. For the TRE-Paqr4 mouse line, founder was first generated on C57BL/6N background, following by back crossed to C57BL/6J background for at

	least four generations. For all studies unless otherwise indicated, mice at 8 weeks old were used; for adipose tissue development studies, transgene was induced on embryonic day 13.
Wild animals	No wild animals included.
Reporting on sex	Male mice were used.
Field-collected samples	This study did not involved samples collected from the field.
Ethics oversight	All mouse protocols were approved by the Institutional Animal Care and Use Committee of the University of Texas Southwestern Medical Center (APN: 2015-101207G).

Note that full information on the approval of the study protocol must also be provided in the manuscript.

Plants

Seed stocks	N/A
Novel plant genotypes	N/A
Authentication	N/A

Flow Cytometry

Plots

Confirm that:

☒ The axis labels state the marker and fluorochrome used (e.g. CD4-FITC).

☒ The axis scales are clearly visible. Include numbers along axes only for bottom left plot of group (a 'group' is an analysis of identical markers).

☒ All plots are contour plots with outliers or pseudocolor plots.

☒ A numerical value for number of cells or percentage (with statistics) is provided.

Methodology

Sample preparation	Subcutaneous adipose tissues were dissected, minced, and digested with 1X Hank's balanced slated solution contained 1mg/ml Collagenase D (Roche, cat# 11088882001) and 1.5% BSA at 37°C for 45 min within a shaking water bath. Subsequently, 10mM EDTA was added and incubated for another 5 min. The digested mixture was then filtered through 100 µm cell strainer and then 40 µm cell strainer. Red blood cells were lysed with 1X RBC lysis buffer. Cells were resuspended with FACS buffer (2% FBS/PBS) and incubated with anti-mouse CD16/CD32 Fc Block (1:200) for 15 min on ice, and then stained with antibodies for 30 min on ice. Cells were washed twice before flow analyses. Sorting was conducted by using a BD Biosciences FACSAria cytometer, and analysis of cell frequency was conducted by using a BD Bioscience LSR II cytometer at the Flow Cytometry Core Facility at UT Southwestern Medical Center.
Instrument	BD Biosciences FACSAria cytometer for soring; BD Biosciences LSR II for flow analysis.
Software	FlowJo (V10.8.1)
Cell population abundance	In wild type samples, EGFP+ PDGFRb+ = 0.04% (Fig.5f); CD142+ ASPCs = 19.7%, ICAM1+ ASPCs = 36.8%, DPP4+ ASPCs = 45.9% (Supplementary Fig.3a).
Gating strategy	For sorting CD45- stromal vascular fraction cells, live cells/single cells were selected with gating on FSC-A/SSC-A, FSC-A/FSC-H and SSC-A/SSC-H singlet gate. CD45- cells were separated from CD45+ hematopoietic cells. For quantifying adipocyte dedifferentiated cells, upon selection of live cells/single cells (pregated on SC-A/SSC-A, FSC-A/FSC-H and SSC-A/SSC-H), CD45-CD31- cells were selected, and further subdivided based on EGFP and PDGFRb expression. CD31-CD45-EGFP+PDGFRb+ cells represent dedifferentiated cells. For quantifying ASPCs, upon selection of live cells/single cells (pregated on SC-A/SSC-A, FSC-A/FSC-H and SSC-A/SSC-H), SVF cells were first gated for Lin- (CD31-CD45-TER119-) SCA1+ ASPCs, and then gated for CD142+ ASPCs. CD142- cells were further gated for ICAM1+ APSCs and DPP4+ ASPCs.

☒ Tick this box to confirm that a figure exemplifying the gating strategy is provided in the Supplementary Information.